Author:
Mukhanov, Dauren

Title:
Development of conjugated microporous polymers for energy storage applications

DEVELOPMENT OF CONJUGATED MICROPOROUS POLYMERS FOR ENERGY STORAGE APPLICATIONS

BY

Dauren Mukhanov

School of Chemistry

UNIVERSITY OF BRISTOL

A dissertation submitted to the University of Bristol in accordance with the requirements for award of the degree of MASTER BY RESEARCH in the Faculty of Science

June 2022

Word count: nineteen thousand six hundred eight

Abstract

In this study, four novel nitrogen-rich conjugated microporous polymers (CMPs) PPAAQ, PBAQ, PPAHQ and PBHQ were synthesised via Buchwald-Hartwig cross-coupling reaction. The polymerisation reaction and the structure of the synthesized polymers were characterised using X-Ray Diffractometry (XRD), Ultraviolet Visible Near Infrared (UV-Vis-NIR) spectroscopy, Fourier-transform infrared (FT-IR) spectroscopy, and scanning electron microscopy (SEM) methods. The total surface area of the materials were determined by the Brunauer–Emmett–Teller (BET) method, and the pore size distributions (PSD) determined by nonlocal density functional theory (NLDFT) method. Hansen solubility parameters and the Bristol-Xi'an-Jiaotong approach (developed in the Faul Research Group) were used to improve solubility and gain high surface area and tunable pore size distributions for these CMPs. Determination of HSPs depends on the interaction between the solvent and polymer by the influence of three major intermolecular interactions: dispersion interaction (δ_D), hydrogen-bonding component (δ_H)), and permanent dipole-dipole interaction (δ_P)). Design, assembly and testing of batteries were done by colleagues from the National Center for Nanoscience and Technology in China.

Key words: Conjugated microporous polymers, Hansen solubility parameters, Lithium-ion batteries, cathode materials

Acknowledgements

First and foremost, I would like to express my deepest gratitude to my supervisor, Prof Charl Faul, for his intellectual guidance and constant encouragement throughout my study. I am deeply grateful for his patience, advice and help in the completion of this project. I would like to thank Prof. Charl Faul for his support during difficult times and because he never stopped believing in me. I would like to express special gratitude to his wife Jacqueline Conradie-Faul for her hospitality and organise entertainments even during lockdown.

My cordial and sincere thanks go to all my colleagues in Faul groups for their professionalism and mutual assistance. I'm glad was a part of a big, friendly and magnificent scientist team. Especially thanks for Basiram Brahma Narzary, Safa Ali Al Siyabi and Xue Fang for their friendship and support. Dr Christian Romero, Maximilian Hagemann, Veronica del Angel Hernandez, Marcos Villeda Hernandez, Dr Ben Baker and Ulzhalgas Karatayeva for all assistance during my study. I am also very grateful to Dr Sébastien Rochat who provided some useful advice during the interview of my annual progress monitoring meeting.

I also thank to Dr Kamran Amin from the National Center for Nanoscience and Technology in China for helping me in electrochemical investigations.

I would like to especially thanks to all the staff and teams who helped with the instrumental and theoretical work. Many thanks to Dr Jean-Charles Eloi electron microscopy technician from School of Chemistry's and Dr Natalie E. Pridmore from Structural Chemistry Laboratory.

Author’s Declaration

I declare that the work in this dissertation was carried out in accordance with the requirements of the University's Regulations and Code of Practice for Research Degree Programmes and that it has not been submitted for any other academic award. Except where indicated by specific reference in the text, the work is the candidate's own work. Work done in collaboration with, or with the assistance of, others, is indicated as such. Any views expressed in the dissertation are those of the author.

SIGNED: ..... *D.Mukhanov*..... DATE:.....15/06/2022.....

Table of Contents

List of Figures

List of Tables

List of Schemes

List of Abbreviations

Abbreviation	Full name
°C	Degree Celsius
BET	Brunauer–Emmett–Teller
B-H Coupling	Buchwald-Hartwig coupling
CMPs	Conjugated microporous polymers
COF	Covalent-organic framework
DAAQ	2,6-diaminoantraquinone
DAHQ	2,5-diaminohydroquinone dihydrochloride
DMF	N,N-dimethylformamide
DMSO	Dimethyl sulfoxide
IUPAC	International Union of Pure and Applied Chemistry
FT-IR	Fourier transform infrared spectroscopy
HSPs	Hansen Solubility Parameters
MOF	Metal-organic framework
nm	Nanometre
NMP	N-Methyl-2-pyrrolidone
POPs	Porous Organic Polymers
PTPA	Poly(triphenylamine)
$Pd(dba)_2$	Bis (dibenzylideneacetone) palladium(0)
PSD	Pore size distribution
PXRD	Powder X-ray diffraction spectroscopy
RHE	Reversible hydrogen electrode
SEM	Scanning Electron Microscopy
TBPA	tris(4-bromophenyl)amine
TBB	tribromobenzene

THF	Tetrahydrofuran
NaOtBu	Sodium tert-butoxide
UV-Vis-NIR	Ultraviolet–visible-near infrared spectroscopy
XPhos	2-Dicyclohexylphosphino-2’,4’,6’-triisopropylbiphenyl
λ	Wavelength

1. Introduction

Growing the abundance of greenhouse gases in the atmosphere, man activities are increasing Earth's natural greenhouse effect. Practically all climate scientists agree that this rise in heat-trapping gases is the main cause of the 1.8 °F (1.0 °C) increase in global average temperature since the late nineteenth century.[1,2] Carbon dioxide, methane, nitrous oxide, ozone, and various chlorofluorocarbons are all human-emitted heat-trapping gases, as shown in Figure 1-1. In the midst of this, carbon dioxide is of highest concern to scientists because it exerts a larger overall warming effect than the other gases combined.[3]

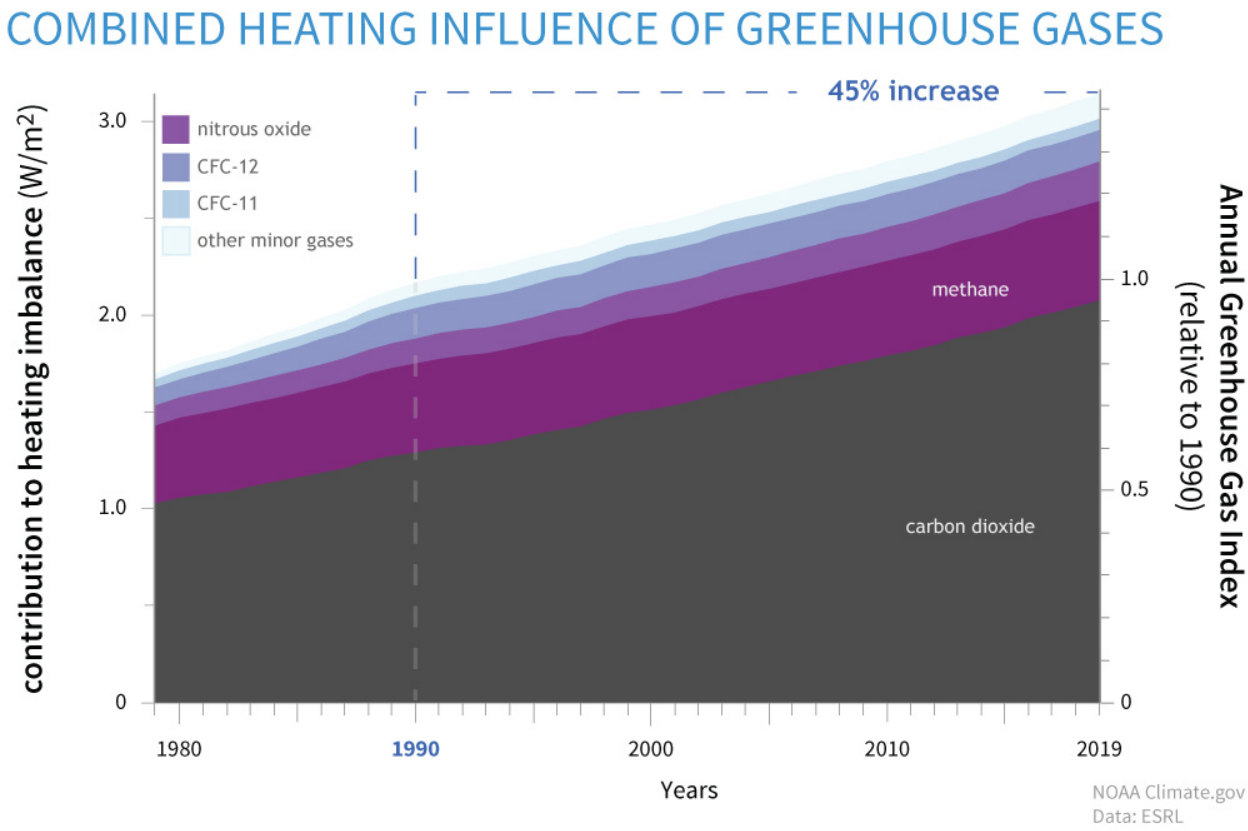

Figure 1-1 Combined heating influence of greenhouse gases[3]

Humans are putting an estimated 9.5 billion metric tons of carbon into the atmosphere each year by burning fossil fuels, and another 1.5 billion through deforestation and other land cover changes. Of this human-produced carbon, forests and other vegetation absorb around 3.2 billion

metric tons per year, while the ocean absorbs about 2.5 billion metric tons per year. A net 5 billion metric tons of human-produced carbon remain in the atmosphere each year, raising the global average carbon dioxide concentrations by about 2.3 parts per million per year.[4] Since 1750, humans have increased the abundance of carbon dioxide in the atmosphere by nearly 50 percent.[4]

There is an acute question in the world about reducing the existing emissions in the fuel supply and use sector that mostly relates to fossil fuel supply. In the near future the demand for fossil fuels in the energy system is expected to decrease, which will affect the output of refineries.

During replacing fossil fuels and reducing greenhouse gas emissions in the fuel supply sector, the main focus areas will be clean generation of electricity, production and use of hydrogen and bioenergy, which will be used to meet the needs of heat, traffic and electricity. [5]

The government of the UK developed a strategy “Net Zero Strategy: Build Back Greener” which is to lead the world in ending humans contribution to climate change, while turning this mission into the greatest opportunity for jobs.[6]

1.1. Porous organic materials

Porous organic materials (POMs) are valuable in different aspects of technology and science because of their applications in energy storage, CO_2 reduction and storage, catalysis and optoelectronics.[7–9] The popularity of porous materials comes from their high surface area, microporosity, and ability to incorporate functional groups. A general classification of porous materials is shown in Figure 1-2. Besides organic porous materials, inorganic porous materials such as zeolites and activated carbon exist as well.

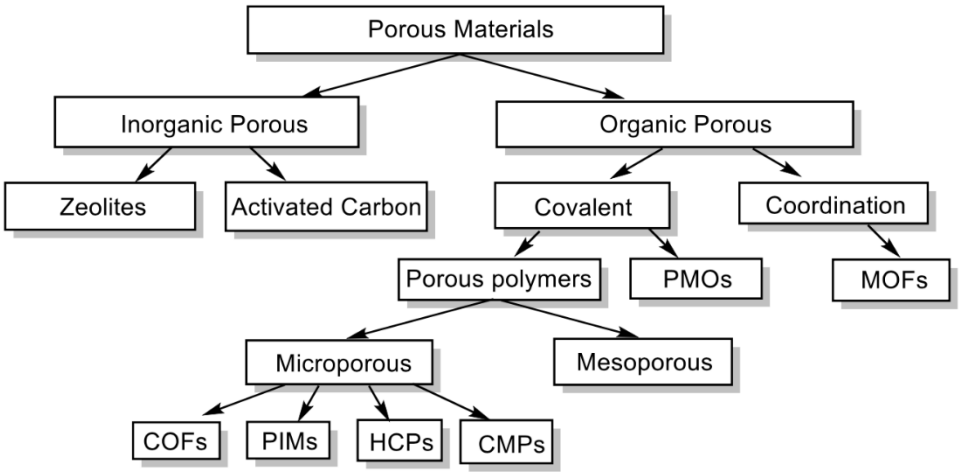

Figure 1-2 Classification of porous materials

According to the International Union of Pure and Applied Chemistry (IUPAC) all porous materials can be divided into groups by diameter (d) of their pores:[10] microporous (d < 2 nm), mesoporous (2 nm < d < 50 nm) and macroporous (d > 50 nm).

Initially, from a research perspective, the skeleton structure of porous polymers progressed from inorganic open frameworks of zeolites to metal organic frameworks (MOFs) and, more recently, to organic porous materials. Organic porous polymers can be fabricated by noncovalent and covalent methods.[11] The non-covalent organic frameworks class includes porous organic cage forms such as hydrogen-bonded organic frameworks,[12] whereas periodic mesoporous organosilica, covalent organic frameworks (COF)[13], polymers of intrinsic polymers (PIMs)[14], hyper-cross-linked polymers (HCPs)[15] and conjugated microporous polymers (CMPs)[16]. They are all units with similar properties: high porosity, lightweight elements, and strong covalent linkages.

Porous materials are discussed in more detail below.

1.1.1. Metal-organic frameworks (MOFs)

One of the considerable discoveries of the end of the last century in inorganic and materials chemistry has been MOFs.[17] MOFs are a class of porous materials that can be easily constructed from metal ion or metal cluster compounds and organic linkers, hybrid inorganic-organic material.[18] **Figure 1-3** shows several representative examples of MOFs structures. These versatile material show great promise because of their synthetic tunability, affording both fine chemical and structural control **Figure 1-4**.[19] With creative synthetic design, properties such as porosity, stability, particle morphology, and conductivity can be tailored for specific applications.[19] As the needs of each energy storage device are different, this synthetic versatility of MOFs provides a method to optimize materials properties to combat inherent electrochemical limitations.[19] In addition, MOFs are popular because of the regular porosity and high surface area (from 1000 m^2/g to 10000 m^2/g).[20] Furthermore, MOFs demonstrate redox-active properties during electrochemical investigations owing to the inorganic units that consist of metal ions and metal oxides. Therefore, MOFs are the most likely to be applied as electrodes for lithium-ion batteries (LIBs) and fuel cells. Over the past 20 years, MOFs were used as anodes, cathodes and electrolytes for LIBs.[21-22] However, the low hydrolytic stability of most of the MOFs makes them unsuitable for applications in humid or other extreme conditions. Despite potential, there is still much to be studied about effective applications of MOFs in devices for energy storage. Design strategies employed in polymers, carbons, ionic liquids, and solid inorganic compounds can serve as inspiration for identifying and discovering new MOF architectures for superior storage capabilities. Furthermore, MOF composite materials are vastly underexplored, and their research will likely reveal new parameter space at the intersection of conventional soft/hard materials and MOFs.[19] Fundamental and applied knowledge gained from MOF-based devices will thus be invaluable for designing next-generation materials for emerging technologies in flexible and transparent electronics, solid-state electrolytes, and advanced energy storage devices in moderate and extreme environments.[19,23–25]

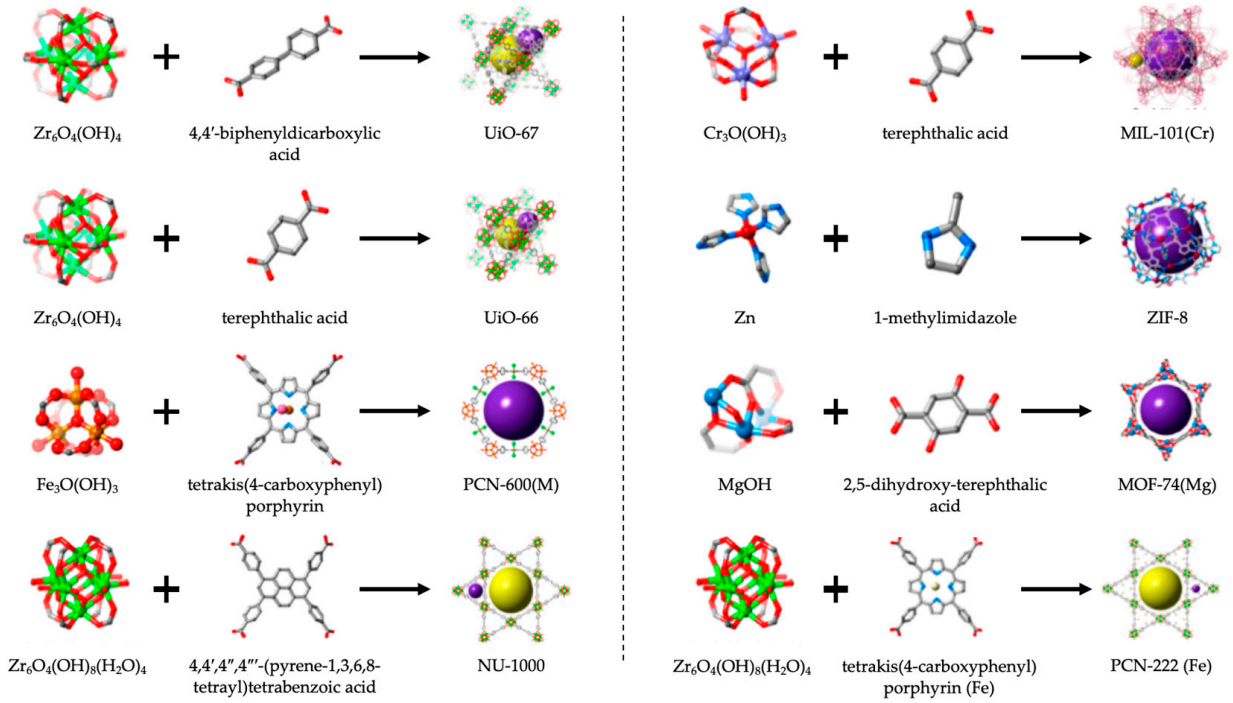

Figure 1-3. Examples of different metal–organic frameworks structures with their corresponding metallic clusters and organic linkers.[26]

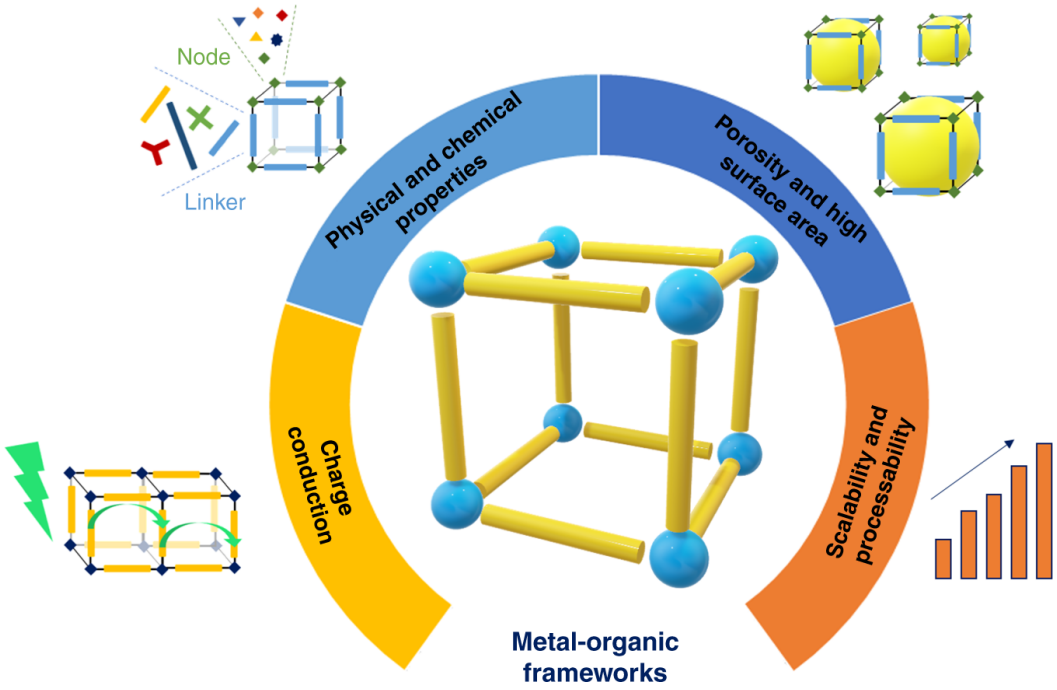

Figure 1-4. Tunable MOF attributes for electrochemical applications.[19]

1.1.2. Covalent organic framework (COFs)

COFs were introduced in 2005 for the first time by Yaghi and Cote.[7] These developments reflect an interesting new class of porous materials that has crystalline structures and linking building templates via hard covalent connections.[7,27] One of the crucial properties of the COFs is the regular distribution of porous structures, and that their size and shapes could be adapted via precise design of building units.[28] There are two types of COFs that rely on constructed blocks dimensions: two (2D) and three (3D) dimensional COFs.[13] Several approaches have been developed to construct COFs with diverse topologies from various building units, as shown in Figure 1-5. Theoretically, the topology of a COF is pre-determined by the dimensions and geometry of its building unit. The ability to predict the skeleton structures of COFs is unique, when compared with other porous materials; it enables the construction of complex geometries with highly ordered structures, rather than primary ordered structures.[29–31] The topology diagram in Figure 1-5 provides a systematic method for generating polygons through integration of building units to form extended lattices in two-dimensional (2D) or three-dimensional (3D) COFs, yielding crystalline networks with alternately placed linkers and knots [31,32].[32,33] In 2D COFs, the covalently linking construction is limited by 2D orientations, that assemble further to create a layered structure to show sequentially aligned columns.[13] This type of COFs is perfect for application in optoelectronic devices because they present π-electron networks into ordered structures.[34,35] Unfortunately, given materials cannot be easily connected with electrodes or include into devices to control.[34] Regarding 3D COFs, the frameworks are expanded into three dimensions via building blocks that including sp^3 carbon or silane atoms, which have high specific surface area, low skeletal density and numerous open sites .[13] A crucial characteristic of 3D COFs is its capacity to infiltrate the pores and span the entire molecular blocks, which enables the fabrication of a framework.[36] According to all the above outlined features COFs can be used in different applications and properties including catalysis, energy storage, gas adsorption and storage, sensing and optoelectronic.[20,27,37]

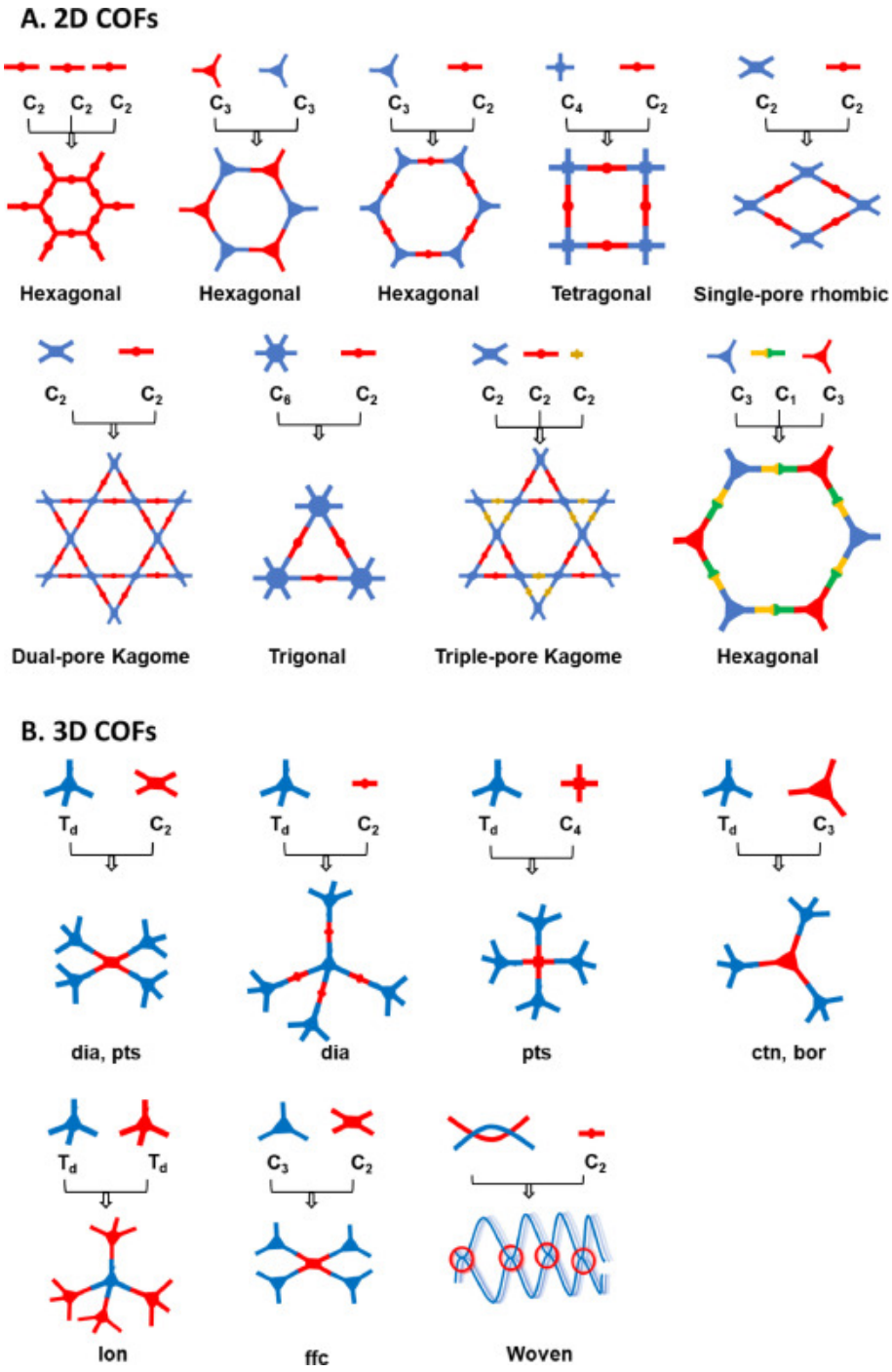

Figure 1-5 Topology diagrams representing a general basis for COF design and construction of (A) 2D COFs and (B) 3D COFs.[38]

1.1.3. Polymers of intrinsic microporosity (PIMs)

The concept of intrinsic microporosity for polymers emerged from work by Budd, McKeown, and co-workers in the early 2000s[14,39] and has been used in the design of materials for gas adsorption and gas separation. PIMs are organic microporous materials that have both a built-in high surface area as well as processability of polymers.[40] Moreover, being in the same class as other types of porous polymers, PIMs possess many prevailing properties such as high thermal and chemical stability,[14] high synthetic reproducibility and low intrinsic density. The rigid and deformed non-crosslinked molecular structure of PIMs guarantee that the primary network cannot move properly.[41] Thus, each part of the macromolecule is not able to pack internally in a space efficient fashion, which leads to creation of micropores in the concave part of the chain.[41,42] Another feature of PIMs that they can be prepared both as a soluble network as an insoluble polymer depending on applications.[42] Nowadays, the valuable properties of PIMs are finding a wider range of applications including in sensors and as membranes for liquid phase separations and in electrochemistry.[40] In particular, there is high interest in the use of PIM membranes in connection with electrochemical energy storage[43,44] and redox flow cells. [45,46] The properties of PIMs depend on molecular weight, functional groups (e.g., to provide acidity/basicity), guest species but also on the deposition method [47] and effects of aging [48] or exposure to air and light.[49] Molecular structures for prototypical types of PIMs are shown in Figure 1-6.

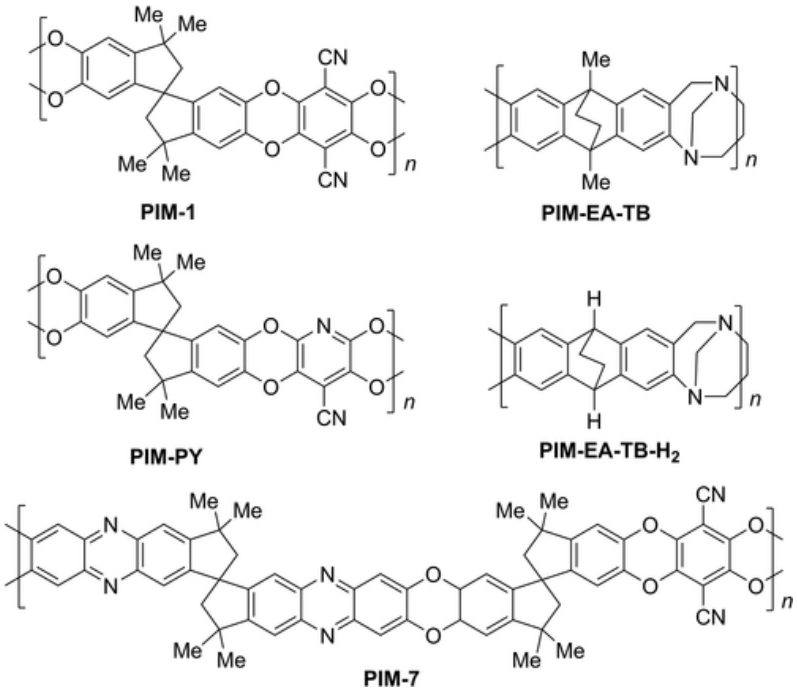

Figure 1-6 Molecular structures of some polymers of intrinsic microporosity

1.2. Conjugated microporous polymers

1.2.1. General properties of CMPs

Conjugated microporous polymers (CMPs) are class of amorphous porous organic materials that link building units in a π-conjugated system to yield 3-dimensional (3D) networks.[50] Their structural characteristics are unparalleled and they do not have analogues among other porous materials.[50] Starting from 2007 when Cooper et al published details of a poly(aryleneethynylene) network,[16] CMPs became a crucial subclass of porous materials. The great variety of synthesis routes to CMPs made them interesting for development of new organic materials with different properties and structures. Constructive design led to new opportunities in gas storage and separation,[51] optoelectronics properties,[52] light emittance,[53] catalysis,[54] and energy storage applications.[55]

In this study CMPs are used as electrode materials for lithium ion batteries owing to a variety of abilities.[56] Firstly, microporosity provides fast electrolyte ion transportation.[50,56] Secondly, the π-conjugated porous structure can be modified to tune the properties of the materials. Finally,

another unique property of CMPs is the large surface area, which creates more active sites[57] and gives a high capacitance.[58] The Faul group has also recently shown that by tuning the Hansen Solubility Parameters (HSPs) in CMP synthesis, fine control over surface area, porosity and function is possible.[59]

1.2.2. Design and synthesis of CMPs

Nowadays, many methods to synthesize CMPs exist. In the main they consist of C-N and C-C coupling reactions such as Suzuki, Sonogashira-Hagihara and Buchwald-Hartwig reactions. During this process strong covalent bonds are formed, and, in addition, π-conjugated structures are created, which contribute to provide high thermal and chemical stability **Figure 1-7.** First CMP-1 synthesized organic conjugated poly(arylene ethynylene) polymers using Sonogashira–Hagihara coupling. These polymers are microporous and exhibit specific surface areas of up to 834 m^2g^{-1}.[60] In 2014 the Faul group reported the synthesis of conjugated microporous polytriphenylamine (PTPA) networks with a surface area up to 530 m^2g^{-1} using BH coupling Figure 1-7.[61] The design and synthesis of these intrinsically microporous materials was based on conjugated polymer networks from a triphenylamine bromide core and selected aryl amine linkers.

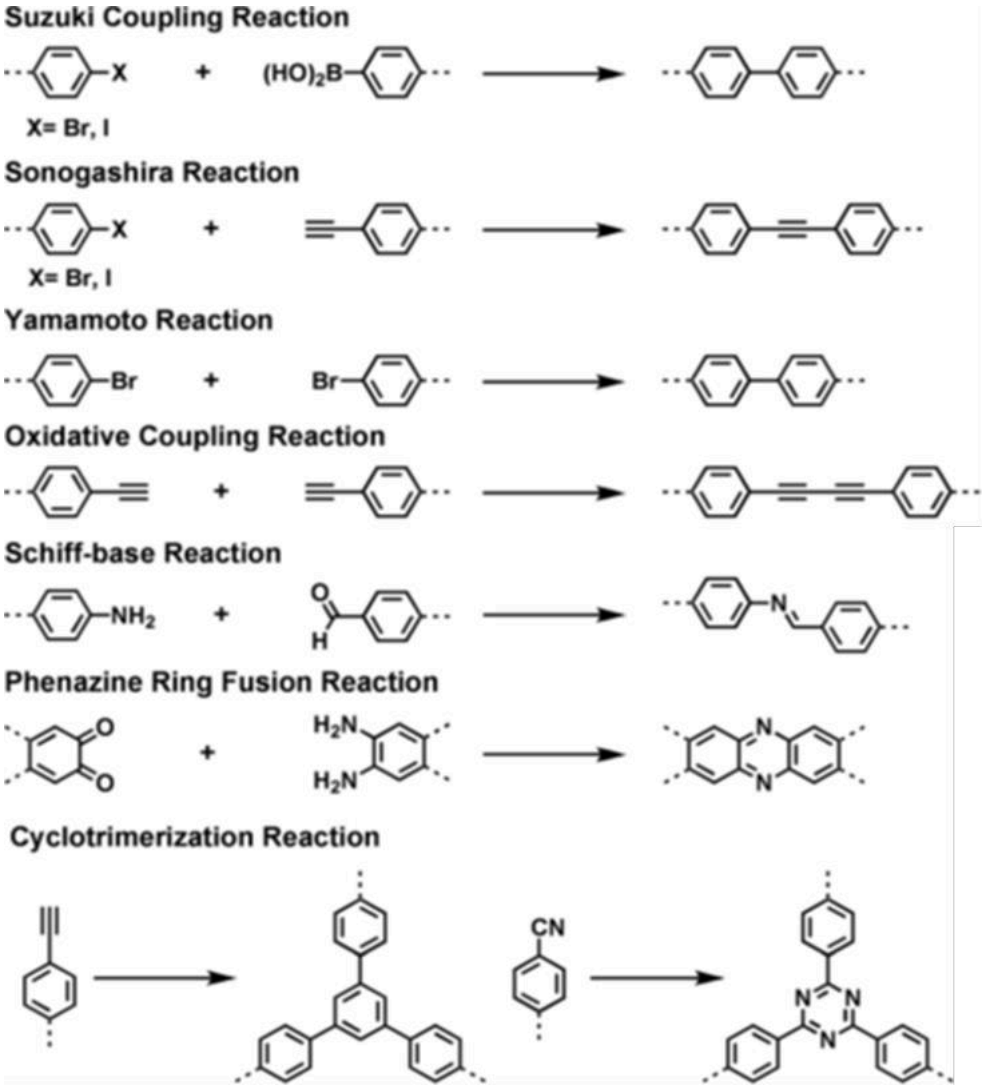

Figure 1-7 Synthetic methods to produce CMPs[62]

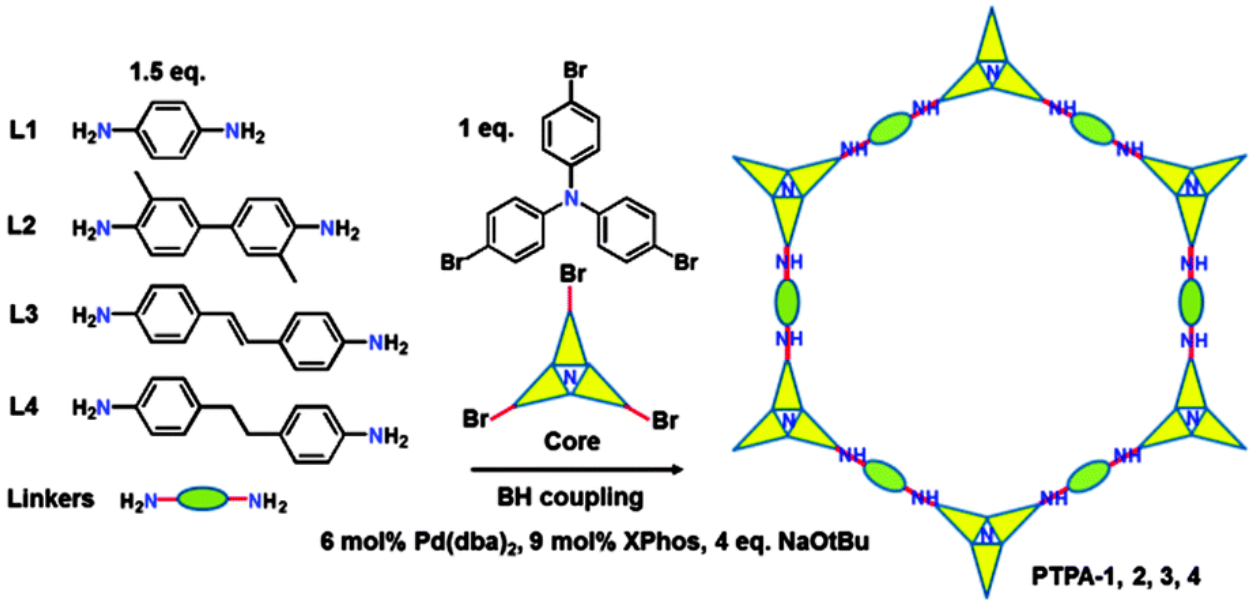

Figure 1-8 Synthetic route to conjugated microporous PTPAs.[61]

In this study Buchwald-Hartwig cross-coupling polymerisation was used, which is an easy method to synthesize CMPs. The general aim of this method is to produce C-N bond by the reaction of aryl halides and amines. Palladium dibenzylideneacetone $Pd(dba)_2$ was used as catalyst because it is stable during exposure in air. In this compiled dba ligands stabilize Pd(0) and provide a chance for ligand exchange to produce a more effective catalyst. XPhos is a three valent phosphorous compound system and act as σ-donating ligand with an unshared electron pair. These properties give solubilization and stabilization to organometallic complexes by forming complexes with various transition metal species including latter period transition metals. Besides, it is used for controlling the reactivity and selectivity of the transition metal promoted reactions. Frequently, the phosphine ligands with a high electron density increase the reactivity of oxidative addition from a metal center and their bulkiness improves their reductive elimination capability.

The mechanism and catalytic cycle of the BH cross-coupling reaction can be seen in **Figure 1-9**. Before starting the catalytic cycle, the catalyst needs to be activated. The dba ligands of $Pd^0(dba)_2$ are replaced by Xphos. That manipulation enhances the electron density of the palladium to increase the rate-determining step in oxidative addition. After the creation of the catalyst

complex, oxidative addition of aryl bromide with PD-L catalyst proceeds to the formation of Pd(II) compounds. Then, the aryl amine group will coordinate to palladium and obtain a positively charged nitrogen, which leads to deprotonation by the base and NaBr precipitates. Finally, the reductive elimination stage takes place to afford the target aryl amine and regenerates the catalyst to go back to its initial state.

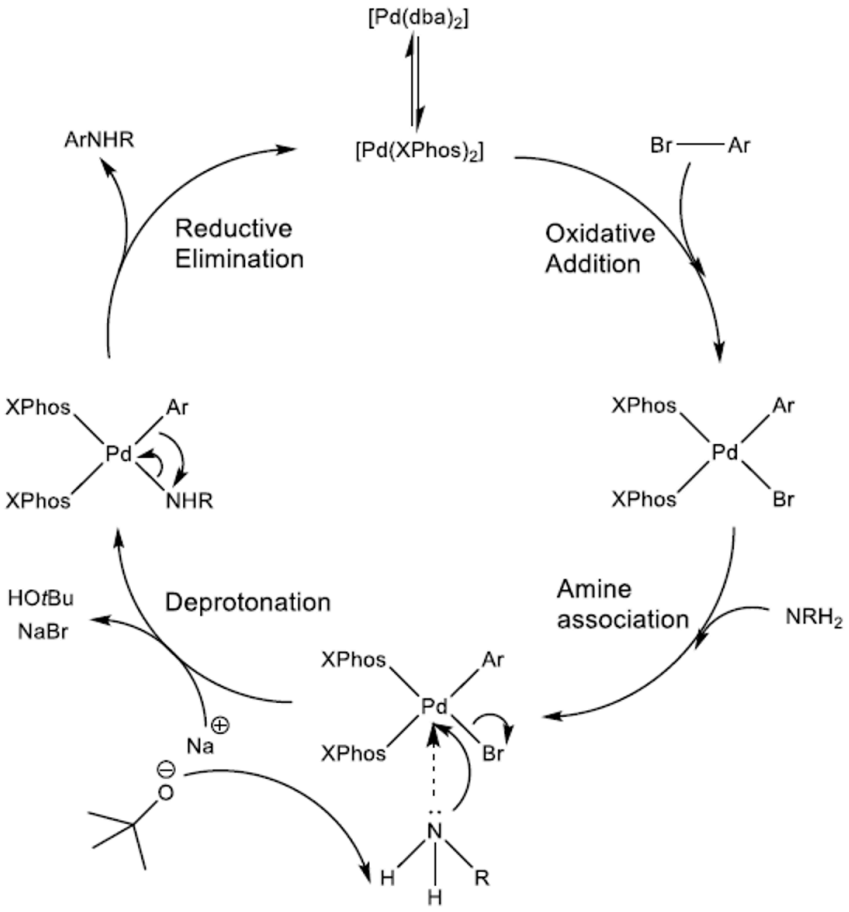

Figure 1-9 Catalytic cycle and mechanism of the Buchwald-Hartwig cross-coupling reaction

1.2.3. Applications of CMPs

CMPs have advantageous properties compared with other POMs: they can be used in different ways for applications, owing to extended conjugation, high surface area and porosity, tunable chemistry and thermal and chemical stabilities.[11,50]

1.2.3.1. Gas Storage and Separation

The main field of study for CMPs is the adsorption and storage of gases.[15,63,64] The synthetic control over structure and composition in CMPs offers strategies to heighten adsorption capacity and selectivity. However, the use of expensive transition metals in many CMP syntheses might prohibit their use in large-scale adsorption applications. The most crucial studied areas are the storage of H_2, CH_4 and CO_2.[50] Interest in H_2 and CH_4 storage is owing to their use as a fuels. Regarding CO_2, it is primary greenhouse which affects global warming and acidification of oceans, and its capture and storage is of high priority.[63]

High chemical abundance, high energy density and environmentally friendly characteristics of hydrogen attracts public interest because the gas represents a future energy resource.[11] The capacity of hydrogen to store vast amounts of energy for extended periods of time is a critical component of its strategic significance in achieving a fully decarbonized energy system. It is why hydrogen storage is considered an essential part of the future infrastructure of the energy network.[65] Storage can support security of supply as production and use growth and become more spread over time and distance. Similarly, for a future energy system with a lot of intermittent renewable power generation, hydrogen could be an important storage medium, converting excess renewable energy into a fuel for use across the economy, and supporting faster and integration of renewable capacity and the transition to a fully decarbonised power system. National Grid's 'Future Energy Scenarios 2021' suggest that between 12 TWh and 51 TWh of hydrogen storage will be required in 2050 across varying net zero compliant scenarios.[66] Similarly, Aurora Energy Research's 'Hydrogen for a Net Zero GB' report concludes that 19 TWh of centralised salt cavern storage might be required by 2050.[67] The UK currently has seven salt caverns and depleted gas fields being used as active natural gas storage facilities, providing

approximately 1.5 billion cubic meters, or 145 TWh, of storage capacity.[68] Although some of this could be repurposed for hydrogen storage, providing the same level of energy storage as hydrogen would require greater capacity given that hydrogen has only a third the energy density of natural gas.[69]

Materials that rely only on relatively weak physisorption where cryogenic temperatures (e.g. <100 K) will be required, only porous materials with high surface areas (>3000 m^2g^{-1}) and optimized pore sizes between 0.7 and 1.2 nm have the potential to meet the hydrogen storage target (9 wt% and 81 kg m 3 in the range of 253–323 K and at a pressure of 100 atm).[11] These porosity requirements can very likely be achieved with CMPs.

Li-CMP made by prof. Wei-Qiao Deng and coworkers showed a strategy to enhance the hydrogen storage capacity of CMP by doping with Li^+ ions. It was found that the capacity of these Li-CMP structures for hydrogen at 1 bar and 77 K, was 6.1 wt %, one of the highest capacities reported to date for physisorption materials.

Carbon dioxide is one of the main greenhouse gases that cause global issues, such as climate warming and increases in sea level and ocean acidity.[11] Among various techniques for capturing CO_2, adsorption using porous materials is energetically efficient and technically feasible. CMPs are quite promising due to their high porosity as well as high tunability of their pore surface functionality, which is important in enhancing interactions with CO_2.[11]

Cooper and co-workers prepared a variety of polyphenylethynylene-based CMPs for the absorption of CO_2 that combine a range of functional groups, including carboxylic acids, amines, hydroxyl and methyl units, into the pore surface Figure 1-10.[63] CO_2 uptake at low pressure (1 bar) depends on the binding energy caused by functional groups rather than on absolute surface area and pore volume. CMP-1 exhibits the highest volumetric CO_2 uptake, with a capacity of 1.18 mmol g^{-1} at 298 K and 1 bar, whereas the CMP with a dimethyl group (CMP-1–$(CH_3)_2$) exhibits the lowest uptake (0.94 mmol g^{-1}). The experimental isosteric heats are dependent on the functional groups and follow an order of –COOH > $(OH)_2$ > NH_2 > H > $(CH_3)_2$.

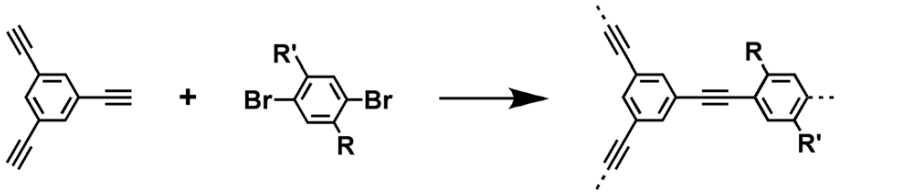

CMP-1 R = R' = H
CMP-1-$(CH_3)_2$ R = R' = CH_3
CMP-1-$(OH)_2$ R = R' = OH
CMP-1-NH_2 R = NH_2, R' = H
CMP-1-COOH R = COOH, R' = H

Figure 1-10 Schematic representation of the synthesis of polyphenylethynylenebased CMPs having different functional groups on the pore wall.[63]

In 2014 Faul and colleagues reported molecular design and synthesis of conjugated microporous polycarbazole networks as new precursors for nitrogen-enriched porous carbons. Obtained porous carbons show a high nitrogen content (6.1 wt %), ultramicropore size (0.7–1 nm), and large surface area (1280 $m^2\ g^{-1}$). In addition, nitrogen-enriched carbons showed highly efficient and reversible CO_2 capture (can store 20.4 wt % at 1 bar and 11.1 wt % at 0.15 bar and at 273 K, while maintaining 100% CO_2 uptake capacity after five cycles).[70]

Methane gas, the primary component of natural gas, is an abundant energy resource. The target value for methane storage is 180 cm^3 (STP) at 35 bar and 298 K or 7.3 wt% at 1 bar.[71] Compared with other gases, less attention has been given to the exploration of CMPs for CH_4 adsorption. The isosteric sorption heats for methane in carbonaceous materials fall within the appropriate range for storage near ambient temperature; hence, organic porous materials are highly promising.

1.2.3.2. Heterogeneous catalysis (structures, type of reaction)

CMPs can be used as a heterogeneous catalyst because they can cooperate with catalytic sites in the system.[54,72] The open porous framework easily gives access of reactants to the catalytic sites. Moreover, it can be interesting to use CMP as a photo-redox catalyst because of the extended conjugated chromophores that form part of the framework.[73]

Cooper et al prepared a metal–organic conjugated microporous polymer (CMP-1) based on cyclometalated Ir complexes with direct metal incorporation by copolymerization and post-synthetic metalation.[74]These two strategies offer the possibility to design conjugated microporous materials with a range of functions. By comparison, the metal node in CMP-1 does not break the conjugation in the network, although it does in MOFs.[75] CMP-1 as a heterogeneous catalyst showed high catalytic activity for reductive amination for a wide range of substrates (Figure 1-11). In addition, the activity for reductive amination of the heterogeneous catalyst CMP-1 is comparable to the homogeneous Ir catalyst.

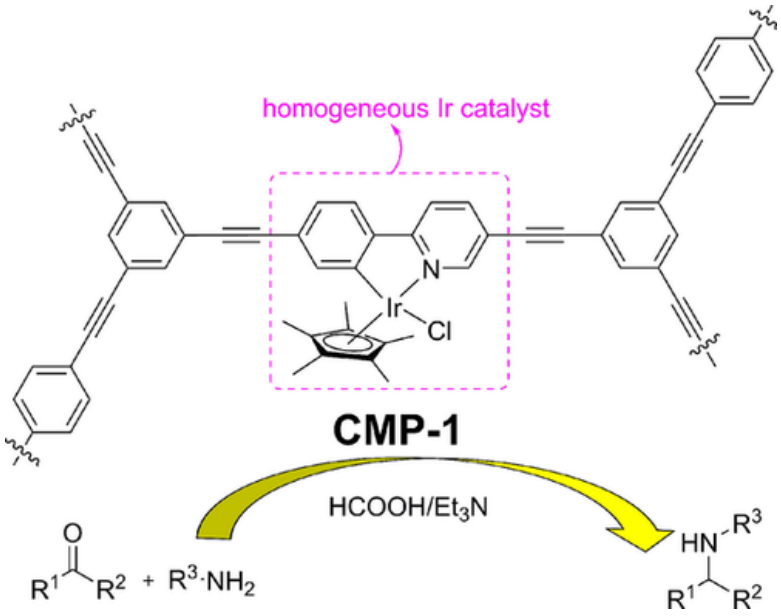

Figure 1-11 Reductive amination catalyzed by CMP-1.[76]

1.2.3.3. Sensors and electrodes

Owing to the extended π-conjugation of CMPs, their luminescent properties are increased and can be used for finding different chemical substance by quenching of the fluorescence.[77] The large open sites in CMPs permit significant interaction with chemicals, and then provide responses and signals with high sensitivity.[78]

A group of researcher from Central South University, China used a luminescent hypercrosslinked conjugated microporous polymer for efficient removal and detection of mercury ions.[79] They

prepared HCMP-1, which has a moderate BET specific surface (432 m^2 g^{-1}), but showed a high adsorption affinity (604 mg g^{-1}) and excellent trace efficiency for Hg^{2+}. The π–π* electronic transition of the aromatic heterocyclic rings endows HCMP-1 with strong fluorescence, with the fluorescence obviously weakened after Hg^{2+} uptake, which makes the hypercrosslinked conjugated microporous polymer a promising fluorescent probe for Hg^{2+} detection with exceptional sensitivity (detection limit 5×10^{-8} mol L^{-1}).

CMPs' crucial properties like microporosity and extended π-conjugation make them suitable candidates for electrodes in energy storage. High surface area and significant amount porosity of CMPs lead to access to many active sites for fast redox kinetics upon the surface. The simple tunability of CMPs allows redox-active groups to be introduced into the framework that might have fascinating properties during the electrochemistry. The biggest problem of using CMPs in this area is poor electronic conductivity, but there have been a number of proposed actions to solve this problem.[80] For example some proposed solutions to improve the electronic conductivity in CMPs may include doping the polymer materials with conductive compounds such as carbon nanotubes or metal nanoparticles, synthesizing CMPs with lower bandgap energies, or incorporating more conjugated chemical structures into the CMPs to enhance charge transfer. CMP energy storage will discussed in detail in Section 1.3.

1.3. Energy storage devices

In contemporary life a variety of energy storage devices (ESDs) exist that have a big impact on our daily routines. It is easy to imagine how reliant we are on technology and the distress caused when, for example, a phone's battery dies. There is a growing dependence on the fast progress of energy storage systems (ESS). Recently, ESS have been used in different applications and divided into four groups: mechanical, chemical, electrical, and electrochemical ESSs.[81–83] Currently, the most extended energy storage is mechanical energy via pumped hydropower.[84] In other areas, electrochemical capacitors and batteries, as part of electrochemical energy storage dominate among mobile systems and the transportation segment owing to their life time, light weight, high charge-discharge efficiency and opportunity to realize a variety of chemistries with low cost, durable and recyclable materials.[84,85]

Even though electrochemical energy storage presents an enormous opportunity for application, shortcomings still exist in exploiting its potential. One of the crucial obstacles are finding ideal electrodes, which would satisfy the requirements of high energy and power densities, and long lifetime.[86]

1.3.1. Properties

The most relevant parameters that characterize energy storage devices are energy density and power density.[87] Energy density is the amount of energy that can be stored in a given system, substance, or region of space.[88] Energy density can be measured in energy per volume or per mass. The higher the energy density of a system or material, the greater the amount of energy it has stored.[89] Power density is a measure of power output per unit volume. While it is not as commonly used a measurement as energy density, it is still useful for conversations about energy systems. It's helpful to understand power density vs. energy density.[87]

Plotting these two characteristics against each other give the well-known Ragone plot (Figure 1-12).[90] The Ragone plot is a known guideline for ESS devices. The Ragone plot is named after David V. Ragone who used this type of plot to compare battery performance.[91] Any kind of energy

storage devices can be compared on a Ragone plot with regard to energy density and power density.

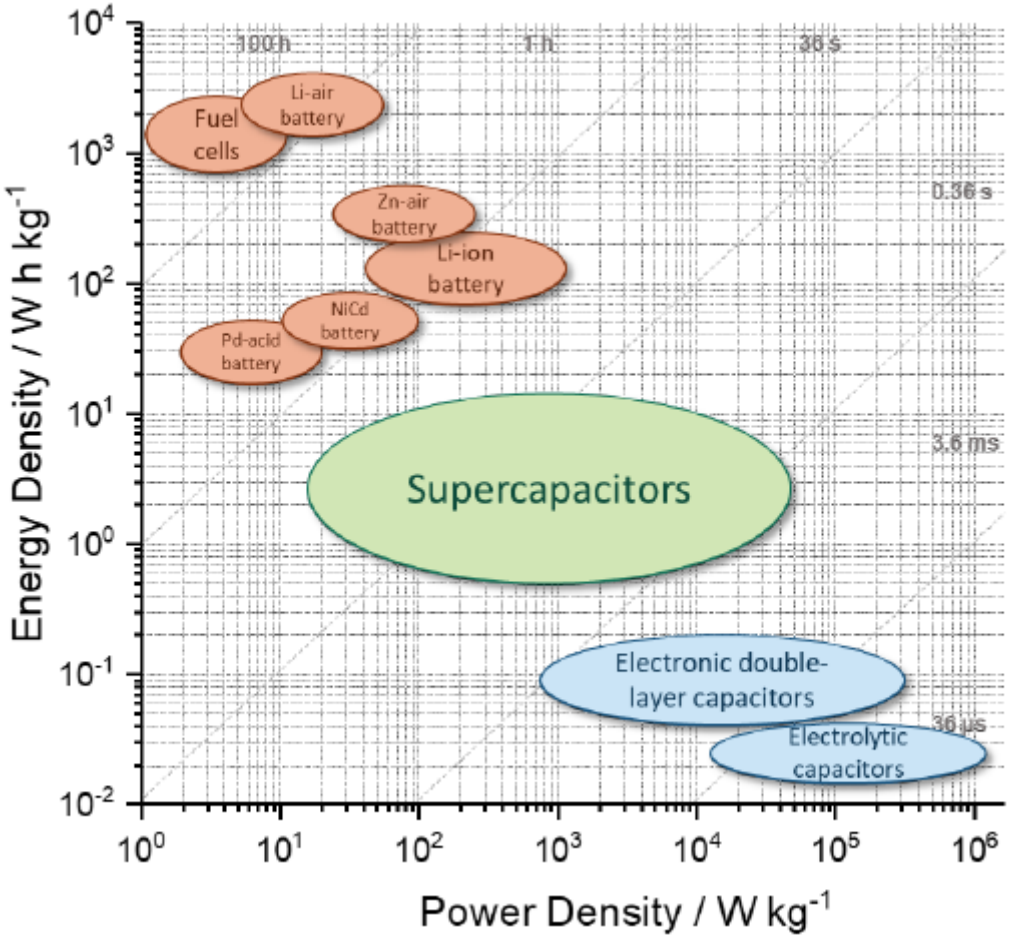

Figure 1-12 Ragone plot comparing various ESS devices[90]

It is clearly seen that the Ragone plot easily shows the limitations and direction of energy devices development.[91] The new developed batteries are placed on the Ragone plot in the upper left position, which shows high energy density. The point that represents capacitors is placed on right side of the Ragone plot, which refers to high power density. Even though the Ragone plot clearly and systematically expresses the energy devices improvement, there are still some drawbacks. Initially, the Ragone plot cannot express devices such as solar cell and wind turbine because they have unlimited and unformed energy.[91] Secondly, the plot cannot correspond to the developments of modern technologies. For example, the Ragone plot only considers gravimetric

energy density, but volumetric energy density has to be considered as well, because new material can be lighter but with the same volume. Due to these factors, the Ragone plot cannot fully show development of supercapacitors.[92]

To summarize, although the Ragone plot has some shortcomings, it is still provides the most helpful guidelines to compare and combine energy storage devices. The Ragone plot manages to provide an intuitive, understandable and organized visualization of relevant data for devices.

1.3.2. Batteries

Advanced technological systems for the storage of energy is required for major industrial applications such as smart grids and electric vehicles.[93] Lithium ion batteries (LiBs) the stage to replace lead acid batteries and will most probably become a crucial power supplier for electric vehicle owing to their significant capacity and long cycle life.[94]

LiBs consist of an anode, a cathode, an electrolyte, and a separator Figure 1-13.[95]. The positive electrode materials are usually Li-containing metal oxides that can have a layered structure such as lithium cobalt oxides or tunnel-like structure such as lithium manganese oxide.[96] The negative electrode materials are typically composed of insertion-type materials such as carbon, $Li_4Ti_5O_{12}$ and TiO_2;[97] conversion type materials such as iron oxides, nickel oxides or cobalt oxides;[98] alloying-type material such as Si or Sn. The main requirements for the electrolyte are that it should be a good ionic conductor and electronic insulator. Mostly, the electrolyte consists of two or more organic solvents containing dissolved lithium salts.[99] The separator needs to prevent short circuiting between the negative and positive electrodes while providing an abundant corridor for delivering lithium ions during charge-discharge processes.[100] When a battery is discharging and providing electric current, Li ions flow from the anode to the cathode. The generated electrons (from the flow of these ions) go through the external circuit and produce the electricity.[101–103] Reversibly, in the charging cycle, the lithium ions in the cathode move from this electrode and pass through the electrolyte and separator to reach the anode, where the anode material structure lead to energy storage. In both the charging and discharging process, electrons are produced and forced to travel through an external circuit against the direction the Li ions

move. It is crucial that the electrolyte does not pass electrons and they are forced to move via external circuit to charge electrical gadgets.[104]

One of the main parts of LiBs is the cathode. The cathode material must have a stable crystalline structure. For the period of charging, the oxidation reactions leads to modification in composition and as a result to negative phase changes.[104] Lithium ions are moved back into the cathode material and ions of transition metal travel from anode to cathode by electrons. Cathode productivity depends on the electrode surface morphology, microstructure, and electrochemical properties of the cathode materials.[105] The current challenge is to find an appropriate material that satisfies all requirements.

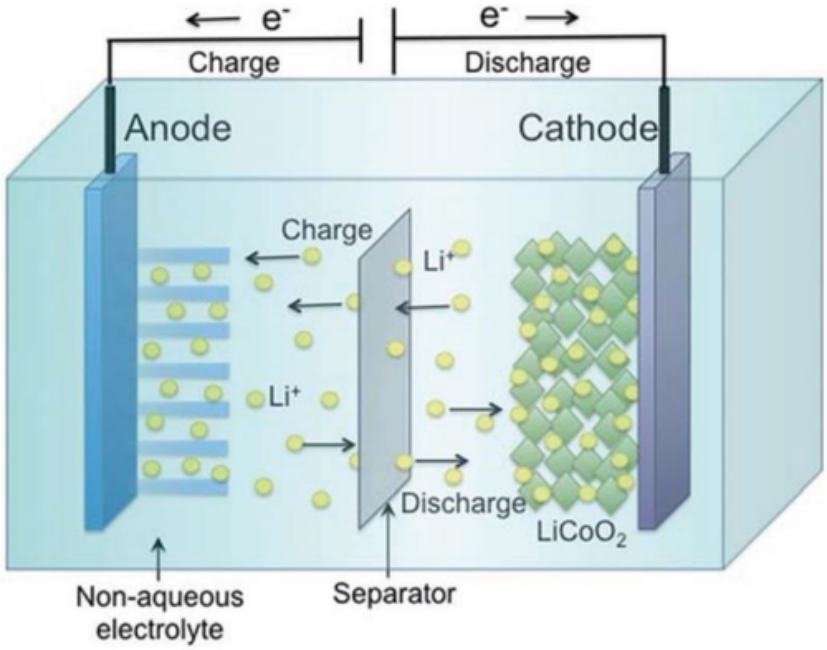

Figure 1-13 Schematic diagram of lithium-ion battery.[106]

1.3.3. Capacitors and supercapacitors

A supercapacitor is an electrochemical energy storage device with a superior capacity compared with conventional capacitors. It also possesses better charging/discharging rates than primary or

secondary batteries.[107,108] A supercapacitor contains two electrodes, an electrolyte and a separator which separates the two electrodes electrically Figure 1-14.[108] The most crucial part of supercapacitor is the electrode.[109] Supercapacitors are eco-friendly,[110,111] very safe and can operate in a varied temperature range with long cycling life (see the Ragone plot Figure 1-5). Therefore, supercapacitors can be used in mobile devices, vehicles, and electronics. For instance, they were used as uninterruptible power supplies and load-levelers in wireless towers.[110,112] Moreover, in association with fuel cells or batteries hybrid electric vehicles can be powered using supercapacitors. Mostly, that happens when increasing the energy density of supercapacitors, but keeping their high-power density stable.[95]

Based on their energy storage mechanisms supercapacitor divided into 2 groups: electrochemical double-layer capacitors (EDLCs) and pseudo-capacitors.

EDLC consist of two electrodes that are based on carbon materials, electrolyte, and a separator. EDLCs can collect charge electrostatically or through non faradaic processes.[113] The electrochemical double layer is the principle that is used in EDLCs. When potential is applied, electrode surfaces store the charge. It happens because of potential differences and there is an attraction of opposite charges, which lead to ions in the electrolyte travel through the separator to pores of the oppositely charged electrode.[108] Producing the double layer of charge helps to keep combination of ions at electrodes stable. The double layer, high specific surface area and low distance between electrodes gives EDLCs higher energy density.[114,115]

Pseudocapacitors store energy using Faradaic processes where charge moving between electrode and electrolyte take place.[116] When voltage is applied, reduction and oxidation processes take place on the electrode materials, and then charge diffuse over the double layer and formed faradic cell passing via the supercapacitor cell. This Faradaic process helps pseudocapacitors reach larger specific capacitance and energy densities than EDLCs. There is significant interest in metal oxides and conducting polymers as main materials for use in pseudocapacitors. However, faradaic process involves redox reaction such as found in batteries. Thus, current materials face the drawback of stability during cycling and have low power density.[117,118]

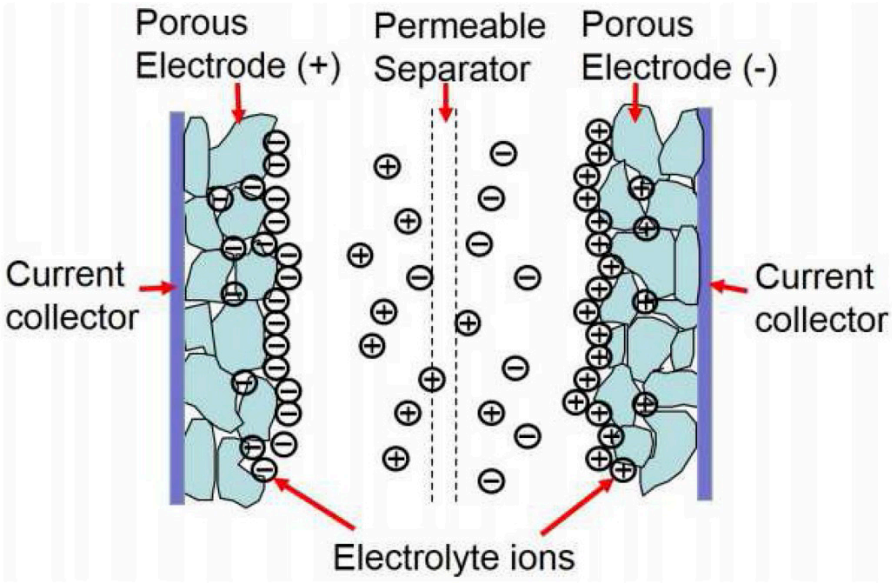

Figure 1-14 A schematic diagram of a supercapacitor at the charged state.[119]

1.4. Hansen Solubility Parameters

Hansen Solubility Parameters (HSP) are a set of three parameters that can be used to predict how well a solvent will dissolve a specific polymer or other compound. The three parameters are dispersion forces, polar forces, and hydrogen bonding forces, which describe the different types of intermolecular forces between molecules.

The HSP values can be used to characterize different solvents as either good or bad solvents for a particular polymer or compound. A good solvent is one that has similar HSP values to the solute, while a bad solvent has different HSP values. By using the HSP values, it is possible to predict the solubility of a material in a range of solvents, which can be very useful in fields such as material science, chemistry, and pharmacy.

In this work we use Hansen solubility parameters to obtain influence of difference solvents to surface area and pore diameters of CMPs. The Faul research group determined that the use of salts, and thus tuning of HSPs, is an important factor to acquire CMPs with high surface areas and well-defined micropores.[59] Owing to discovery Bristol–Xi'an Jiaotong (BXJ) method where salts

are used to carefully tune N-containing conjugated microporous materials and optimizing the Hansen solubility parameters, they can improve the BET surface area from 58 $m^2 g^{-1}$ to a maximum of 1152 $m^2 g^{-1}$.[59] It is important that adjusting the ionic radii of the salts lead to control is exerted over surface areas. Then it method was expanded using simple salts to fine-tune the porosity of conjugated microporous materials synthesized by various reaction approaches, including Buchwald–Hartwig (BH), Sonogashira–Hagihara, oxidative coupling and Suzuki cross-coupling.[120] This works confirm that HSPs of solvents and addition of the salts can be a crucial instruments for the preparation of fully tunable porous materials.

Hildebrand and Scoot were first who use solubility parameter as a term for select solvents for coatings materials.[121,122] The square root of cohesive energy determine the solubility parameter according to Hildebrand:

$$\delta=\sqrt{\frac{E}{V}}$$

Where E – energy of vaporisation, V – molar volume of pure solvent. The conventional units for solubility parameter is $MPa^{1/2}$ or $(Cal/cm^3)^{1/2}$. The shortcomings of this work was that the method was restricted to regular solvents as determined by Hildebrand and Scoot.[121] Moreover, early work does not account for the interaction between molecules, which is required for polar and hydrogen-bonding interactions.

Considering shortcomings of the early work, Charles Hansen developed Hansen solubility parameters (HSPs) in 1967.[121] The unique feature of this parameter compared with previous work was that Hansen found an experimentally valid and compatible way to divide the Hildebrand parameter into three components: Dispersive (van der Waals), Polar, and Hydrogen-bonding, and generate large tables of values for practical use. HSPs gives practical understanding of solubility, diffusion, chromatography and more.

Nonpolar interactions are the most common type, also called dispersion interactions in the literature.[121] Because of molecules constructed from atoms, all molecules contain these kind of forces. For instance, there are the only cohesive interactions for the saturated aliphatic hydrocarbons, and the energy of vaporization is assumed to be the same as the dispersion

cohesive energy. Calculating the three Hansen solubility parameter are started by defining the dispersion cohesive energy.

The polar cohesive energy, E_P, is based on the permanent dipole-permanent dipole interactions. Intrinsically, these are molecular interactions that can be detected in vast majority of molecules. The dipole moment is commonly used for calculating these interactions. The polar solubility parameters are precise, experimentally proved, and can be found from molecular parameters. The most polar of the solvents include those with relatively high total solubility parameters that are not particularly water soluble, such as nitroparaffins, propylene carbonate, and tri-*n*-butyl phosphate.[121] In solvents where dipole moments are zero, the crucial consideration is the existence of induced dipoles, which are not addressed in this method.

The third type of interactions are hydrogen bonding interactions, E_H, which are called an electron exchange parameter. Hydrogen bonding is a particular type of dipole-dipole attraction between molecules, not a covalent bond to a hydrogen atom. It results from the attractive force between a hydrogen atom covalently bonded to a very electronegative atom such as a N, O, or F atom and another very electronegative atom. Owing to hydrogen bonds, there are attractions between molecules, and accordingly, it forms the basis of this type of cohesive interactions. In this method, the hydrogen-bonding parameter was used to collect energies from interactions, which is not included in the other two parameters. The highest hydrogen-bonding parameters are found in alcohols, glycols, carboxyl acids and other hydrophilic materials.

Total cohesion energy defines the main Hansen parameter equation:

$$E=E_D+E_P+E_H$$

If the energy is divided by the molar volume it gives the square of the total solubility parameter (δ) as the sum of the squares of Hansen dispersion cohesion (solubility) parameter (δ_D), polar cohesion (solubility) parameter (δ_p), and hydrogen bonding cohesion (solubility) parameter (δ_H).

$$E/V_m=E_D/V_m+E_P/V_m+E_H/V_m$$

$$\delta^2=\delta^2_D+\delta^2_P+\delta^2_H$$

1.5. Aim and objectives

The aim of this project was the synthesis of conjugated microporous polymers as electrodes for lithium-ion batteries.

Three objectives were identified to reach the stated aim:

1. Careful choice of carbonyl-containing CMPs, and optimisation of Buchwald-Hartwig cross-coupling reaction conditions.

2. Synthesis, characterisation and optimising HSPs to explore the influence of different solvents on surface area and pore diameters of CMPs.

3. Energy storage studies to investigate the influence of tuning the structures on the functionality.

The discussions in the following chapter will show how the aim and the objectives set out here were reached for this investigation

2. Methodology/ Experimental

2.1. Synthesis and starting materials

Buchwald-Hartwig (BH) cross-coupling reactions were used for the synthesis of the conjugated microporous polymers. The following additional materials and reagents were used for this type of reaction.

In this study, two core materials were used: tris(4-bromophenyl) amine (TBPA) and 1,3,5-tribromobenzene (TBB). (Figure 2-1)

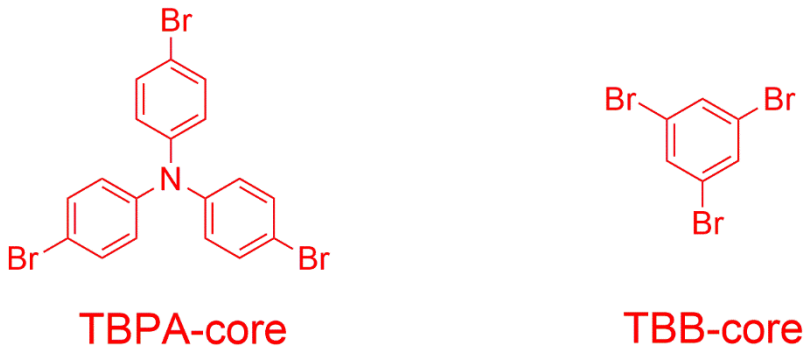

Figure 2-1: Core materials

As linkers 2,6-diaminoantraquinone (DAAQ) and 2,5-diaminohydroquinone dihydrochloride (DAHQ) were used. (Figure 2-2)

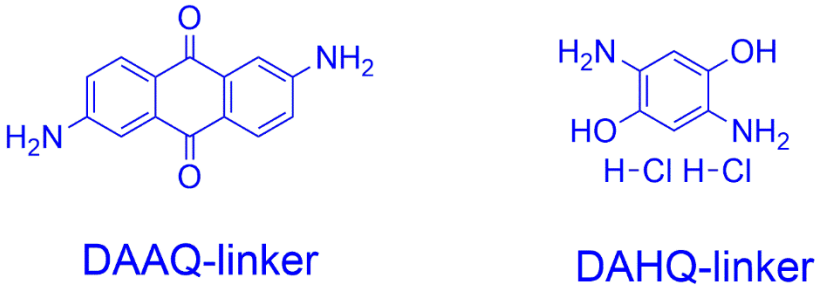

Figure 2-2: Linker materials

Bis(dibenzylideneacetone)palladium(0) (Pd(dba)) was used as catalyst, 2-dicyclohexylphosphino-2',4',6'-triisopropylbiphenyl (XPhos) as ligand, and sodium tert-butoxide as a base. All starting

materials and chemicals for the BH cross-coupling reaction was ordered from Merck and used as received. Dry solvents were collected from Synthetic lab in the School of Chemistry.

2.2. Optimizing reaction conditions

Reaction parameters such as reagent ratios and solvent were optimised to achieve a high yield and a high surface area. Also, the impact of salt on the porosity of polymers was explored. The large core TBPA and long linker DAAQ were chosen as a starting material for optimization, Scheme 2-1. Syntheses were performed in three different core:linker ratios of 1:1.5, 1:2 and 1.5:1 and with two solvents, toluene and tetrahydrofuran (THF). More detailed information regarding these parameters is presented in Table 2-1.

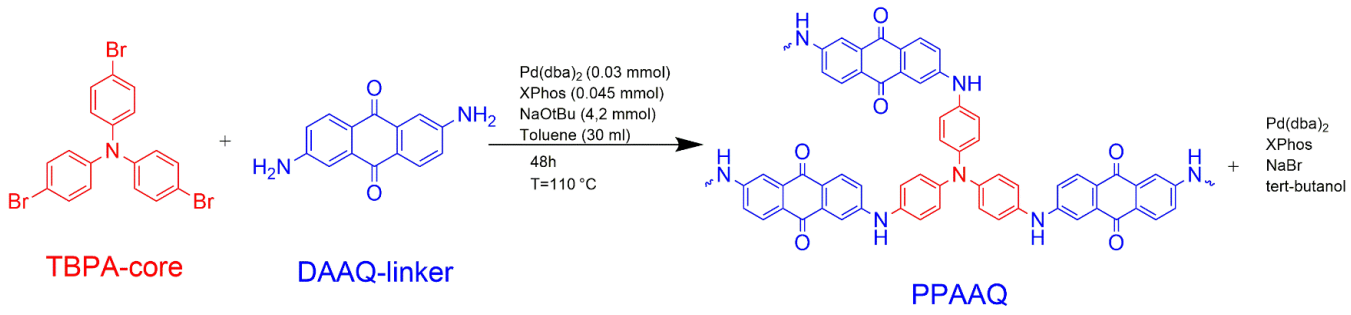

Scheme 2-1 Synthesis of poly (phenyl amino anthraquinone), PPAAQ

Table 2-1 Optimising Buchwald-Hartwig (BH) cross-coupling reaction conditions

Reaction schemes	Conditions	Ratio and name
TBPA+DAAQ	Solvent: Toluene Without NaF, 48h, 110 °C	PPAAQ 1:1.5
		PPAAQ 1:2
		PPAAQ 1.5:1
TBPA+DAAQ	Solvent: Toluene Add NaF, 48h, 110 °C	PPAAQ 1:1.5
		PPAAQ 1:2
		PPAAQ 1.5:1
TBPA+DAAQ	Solvent: THF, Add NaF, 48h, 65 °C	PPAAQ 1:1.5
		PPAAQ 1:2
		PPAAQ 1.5:1
TBPA+DAAQ	Solvent: THF, without NaF, 48h, 65 °C	PPAAQ 1:1.5
		PPAAQ 1:2
		PPAAQ 1.5:1

2.3. Calculation of Hansen Solubility Parameters

After the initial exploratory part of the research project, Hansen solubility parameters and the Bristol-Xi'an-Jiaotong approach (developed in the Faul Research Group) were used to improve solubility and gain high surface area and tuneable pore size distributions for these CMPs. The four polymers chosen to calculate HSPs for were: PPAAQ, PBAQ, PPAHQ and PBHQ.

Firstly, the polymer of interest should be ground to a fine powder. Secondly, 2 mg samples of the polymer are placed into vials for further investigation. Each vial is then filled with 5 ml of a chosen solvent. In this work we use 14 different solvents (all with known and published HSP data), as listed in Table 2-2: dimethyl sulfoxide (DMSO), dimethylformamide (DMF), acetonitrile, N-methyl-2-pyrrolidone (NMP), 1-methylimidazole, dimethylacetamide, propylene carbonate, quinoline, glycerol, xylene, toluene, ethanol and dioxane. It is important to note that amount of polymer and solvents must be the same in all vials. The numbered vials were sonicated for 24 hours, and sonicated suspensions were left to settle for 1-2 hours before the last stage. Aliquots of solution from vials were pipetted out to measure the UV-Vis absorption spectra. Note - it is important to correct the baseline for each solvent during the UV-Vis spectroscopic investigations. Finally, all results were transferred and data plotted (for an example of plotted data see Figure 2-3).

Table 2-2: List of polymers with HSP data

Sl No.	Solvents	δ_D[a]	δ_P[b]	δ_H[c]	δ_T[d]
1	Quinoline	20	5.6	5.7	21.53
2	NMP	18	12.3	7.2	22.95
3	DMSO	18.4	16.4	10.2	26.67
4	Propylene carbonate	20	18	4.1	27.22
5	Dioxane	17.5	1.8	9	19.76
6	DMF	17.4	13.7	11.3	24.86
7	1-methylimidazole	20.6	14.9	11	27.7
8	Acetonitrile	15.3	18	6.1	24.39
9	Xylene	17.8	1	3.1	18.09
10	Ethanol	15.8	8.8	19.4	26.52
11	Toluene	18	1.4	2	18.16
12	Dimethylacetamide	16.8	11.5	9.4	22.42
13	Acetone	15.5	10.4	7	19.93
14	m-cresol	17.96	15.73	10.46	26.06

[a] δ_D suggests the parameter. [b] δ_P suggests the permanent dipole interaction parameter. [c] δ_H suggests the hydrogen-bonding interaction parameter, [d] δ_T suggests the total Hansen solubility parameter.

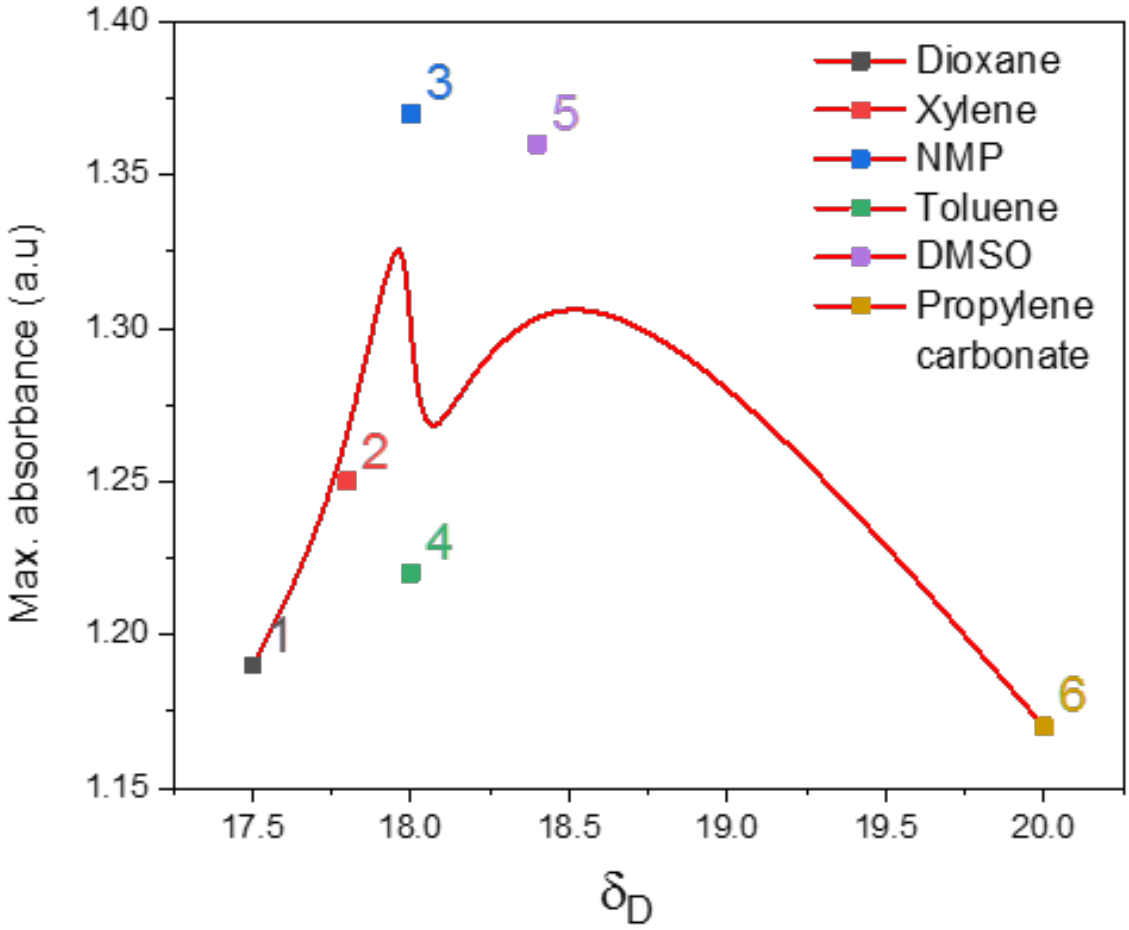

Figure 2-3: Calculation of HSPs for PPAAQ (as example).

The highest peak in Figure 2-3 showed the most efficient dispersion of the polymer, thus indicating that the solvent in question would be worth further investigation. In this case the peak belongs to NMP, which means the δD parameter of the polymer is compatible with the same parameter of NMP. The same procedure is then used to identify the polar and hydrogen-bonding components of the prepared polymer. After determining the best match for all three parameters, the total HSP is calculated according to the formula.

$\delta^2 = \delta^2_D + \delta^2_P + \delta^2_H$

Once the HSP parameters are calculated for the polymers, the difference between total HSP of polymers and total HSP parameter of solvents was determined. This difference will show how polymers and solvents are compatible with each other. For example, if the difference is less than

1, the solvent is a good solvent for the polymer; if between 1 and 3 the solvent is of medium quality; when difference is more than 3 it means the solvent is a poor solvent.

2.4. Synthesis of control CMPs for HSPs study.

2.4.1. Synthesis of CMPs (PPAAQ)

The synthesis of PPAAQ was achieved using a Buchwald-Hartwig cross-coupling reaction. A Schlenk tube was placed in a drysyn setup and charged with TBPA (0.3 mmol, 144mg) and DAAQ (0.45 mmol, 107 mg), Pd(dba)2 dba=dibenzylideneacetone, 17.3 mg, 0.03 mmol), 2-dicyclohexylphosphino-2',4',6'-triisopropylbiphenyl (XPhos, 21.5 mg, 0.045 mmol), and sodium tert-butoxide (NaOtBu, 403.62 mg, 4.2 mmol), and placed under a nitrogen atmosphere. Toluene (30 ml) was added to reaction the reaction mixture and sonicated for 10 minutes to obtain a homogeneous mixture. The reaction mixture was kept under constant stirring at room temperature for 2 hours before heating under constant stirring to 110 °C for 48h. The reaction was cooled to room temperature and solvents were removed by vacuum filtration. The remaining solids were washed with chloroform, methanol, ethanol and acetone (200 mL each), then Soxhlet extracted with methanol for 24 h, THF for 24 h and chloroform for 24 h, and finally, dried at 100 ^{o}C for 72 h in a vacuum oven.

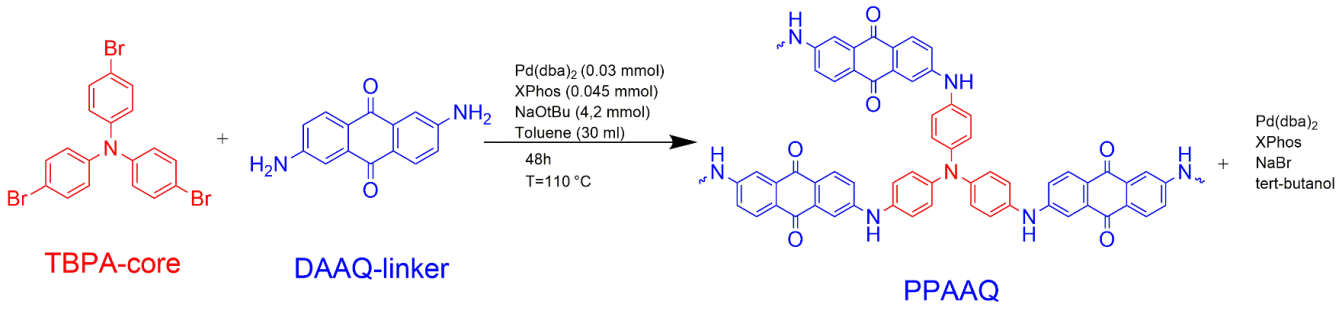

Scheme 2-2 Synthesis of poly(phenyl amino anthraquinone) (PPAAQ)

2.4.2. Synthesis of CMPs (PBAQ)

A Buchwald-Hartwig cross-coupling reaction was used to synthesize PBAQ. Before the start of the synthesis, a Schlenk tube was completely dried by heat gun and placed in a drysyn setup and charged with 1,3,5-tribromobenzene (0.3 mmol, 94.44 mg) and 2,6-diaminoanthraquinone (0.45 mmol, 107 mg), Pd(dba)2 dba=dibenzylideneacetone, 17.3 mg, 0.03 mmol), 2-dicyclohexylphosphino-2',4',6'-triisopropylbiphenyl (XPhos, 21.5 mg, 0.045 mmol), and sodium tert-butoxide (NaOtBu, 403 mg, 4.2 mmol), and placed under a nitrogen atmosphere. Toluene (30 ml) was added to reaction mixture and sonicated for 10 minutes to obtain a homogeneous mixture. The reaction mixture was kept under constant stirring at room temperature for 2 hours before heating under constant stirring to 110 °C for 48h. It is important that the Schlenk flask must be open to the line to avoid any pressure increase. Once completed, the system was left to cool down to avoid handling the very hot glassware. The reaction was cooled to room temperature and solvents were removed by vacuum filtration. The remaining solids were washed with chloroform, methanol, ethanol and acetone (200 mL each), then Soxhlet extracted with methanol for 24 h, THF for 24 h and chloroform for 24 h, and finally, dried at 100 °C for 72 h in a vacuum oven.

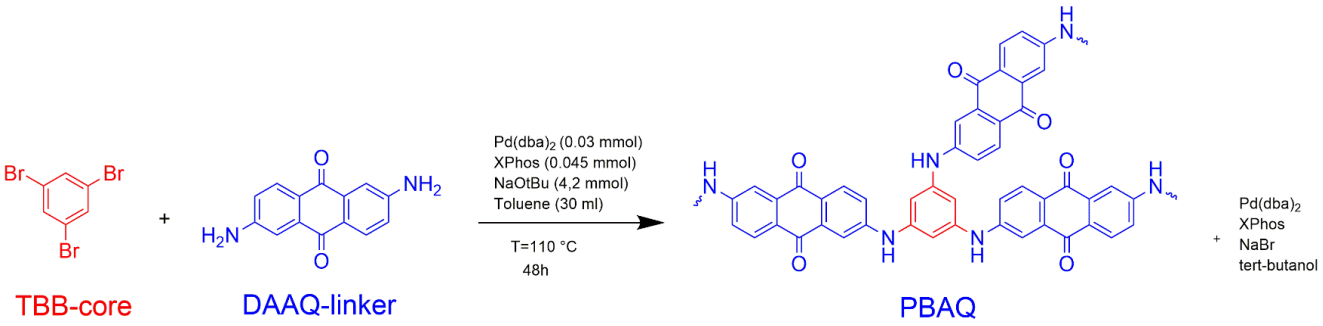

Scheme 2-3 Synthesis of poly(benzene amino anthraquinone) (PBAQ)

2.4.3. Synthesis of CMPs (PPAHQ)

A Schlenk tube was placed in an oil bath and charged with tris(4-bromophenyl)amine (0.3 mmol, 145 mg) and 2,5-diaminohydroquinone dihydrochloride (0.45 mmol, 96 mg), Pd(dba)2 dba=dibenzylideneacetone, 17.3 mg, 0.03 mmol), 2-dicyclohexylphosphino-2',4',6'-triisopropylbiphenyl (XPhos, 21.5 mg, 0.045 mmol), and sodium tert-butoxide (NaOtBu, 1414 mg, 12.6 mmol), and placed under a nitrogen atmosphere. Toluene (30 ml) was added to the reaction mixture and sonicated for 10 minutes to obtain a homogeneous mixture. The reaction mixture was kept under constant stirring at room temperature for 2 hours before heating under constant stirring to 75 °C for 96h. It is important that the Schlenk flask must be open to the line to avoid any pressure increase. Once completed, the system was left to cool down to avoid handling the very hot glassware. The reaction was cooled to room temperature and solvents were removed by vacuum filtration. The remaining solids were washed with chloroform, methanol, ethanol and acetone (200 mL each), then Soxhlet extracted with methanol for 24 h, THF for 24 h and chloroform for 24 h, and finally, dried at 100 oC for 72 h in a vacuum oven.

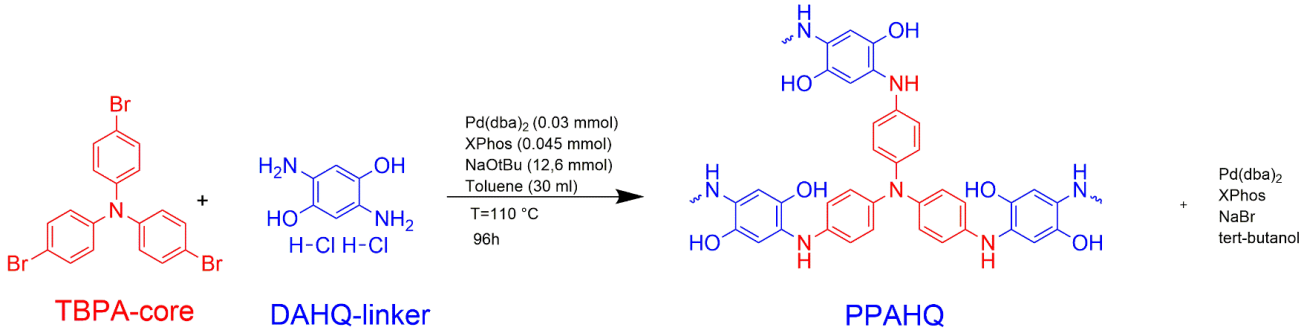

Scheme 2-4 Synthesis of poly(phenyl amino hydroquinone) (PPAHQ)

2.4.4. Synthesis of CMPs (PBHQ)

A Schlenk tube was placed into oil bath and charged with 1,3,5-tribromobenzene (0.3 mmol, 94.44 mg) and 2,5-diaminohydroquinone dihydrochloride (0.45 mmol, 95.88 mg), Pd(dba)2 dba=dibenzylideneacetone, 17.3 mg, 0.03 mmol), 2-dicyclohexylphosphino-2',4',6'-triisopropylbiphenyl (XPhos, 21.5 mg, 0.045 mmol), and sodium tert-butoxide (NaOtBu, 1414 mg, 12.6 mmol), and placed under a nitrogen atmosphere. Ethanol (30 ml) was added to reaction mixture and sonicated for 10 minutes to obtain a homogeneous mixture. The reaction mixture was kept under constant stirring at room temperature for 2 hours before heating under constant stirring to 75 °C for 96h. It is important that the Schlenk flask must be open to the line to avoid any pressure increase. Once completed, the system was left to cool down to avoid handling the very hot glassware. The reaction was cooled to room temperature and solvents were removed by vacuum filtration. The remaining solids were washed with chloroform, methanol, ethanol and acetone (200 mL each), then Soxhlet extracted with methanol for 24 h, THF for 24 h and chloroform for 24 h, and finally, dried at 100 oC for 72 h in a vacuum oven.

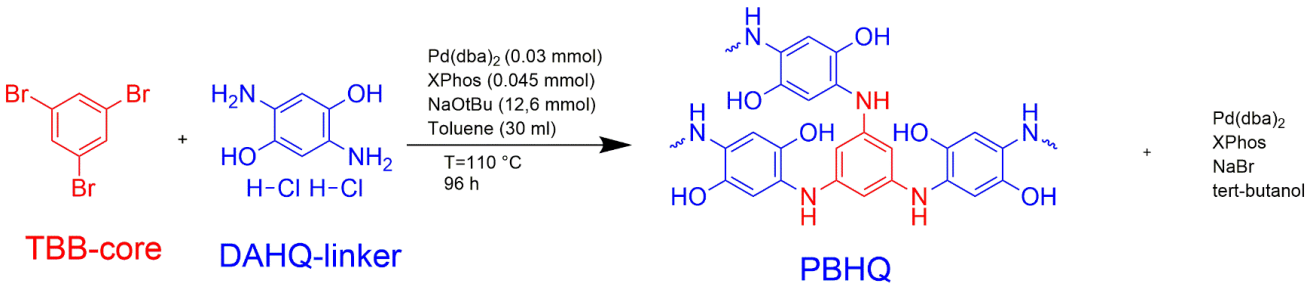

Scheme 2-5 Synthesis of poly(benzene hydroquinone) (PBHQ)

2.5. Characterization techniques and instrumentation

In this study, the determination of physisorption isotherms is achieved by an Autosorb iQ gas adsorption analyser from Quantachrome. Generally, the whole process of the analysis can be summarized in three steps: sample degassing, manometric analysis and data processing. After

the initial drying and degassing step on a Schlenk line at high temperature (140^{o} C) and reduced pressure, the samples were loaded into the cells and then exposed to a high vacuum at an elevated temperature for gas and residual solvent removal. To ensure that the isotherms were reproducible, all the samples were degassed at 70^{o} C for 20 hours, while the heating rate was controlled at 1 deg/min.

The characteristic vibration peaks belonging to the core and linker were detected using Fourier transform infrared (FTIR) spectroscopy. The analysis was performed on a PerkinElmer Spectrum 100 spectrometer.

Crystallinity in the prepared CMPs was determined by powder X-ray diffractometry (PXRD), recorded using a Bruker D8 Advance.

Solid-state ultraviolet-visible near-infrared (UV−vis/NIR) spectra were obtained using a Shimadzu UV-2600 spectrometer.

Cyclic voltammetry (CV) is a powerful and popular electrochemical technique commonly employed to investigate the reduction and oxidation processes of molecular species. A three-electrode H-cell set-up was used for the preliminary characterisation of PBHQ. There was used Pt wire as a counter electrode, saturated Ag/AgCl as reference electrode and glassy carbon as a working electrode. Ar and CO_2 was bubbled through the electrolyte ($KHCO_3$ 0.1 M, 5.0 mL on each side) for 30 min prior to measurements. The pH was measured after this time to account for any pH deviations. The potentiostat-galvanostat was Model 273A, (EG&G Princeton Applied Research, USA). The electrolyte on the cathode side was collected and cryogenic 500 MHz NMR performed for liquid products characterisation (sample 1000 µL, D2O 180 µL, maleic acid 10 µL of a 10 µM solution). Current vs voltage characteristics were recorded by scanning the potential from -1.75 V to 0.25 V with a scan rate of 20 mV S^{-1}. The measured potentials vs. Ag/AgCl were converted to the reversible hydrogen electrode (RHE) scale according to the Nernst equation:

$$E_{RHE} = E_{Ag/AgCl} + 0.059\ pH + E^{o}_{Ag/AgCl}$$

where E_{RHE} is the converted potential vs. RHE, $E^{o}_{Ag/AgCl}$ = 0.1976 at 25 °C, and $E_{Ag/AgCl}$ is the experimentally measured potential against Ag/AgCl reference.

SEM images were recorded using a JEOL 6330 FEG SEM. Samples were either prepared on glass slides that were fixed to the aluminum sample holders using adhesive carbon pads or were directly prepared on the sample holders themselves. All samples were sputter-coated with a 15 nm layer of silver.

2.6. Design, assembly and testing of batteries (performed in Beijing by collaborators at the National Centre for Nanoscience and Technology)

All electrochemical investigations were done in the National Center for Nanoscience and Technology in China. Coin cells are a standard way to test prototype materials for batteries. The coin cell is safely sealed and can be tested on standard test apparatuses.

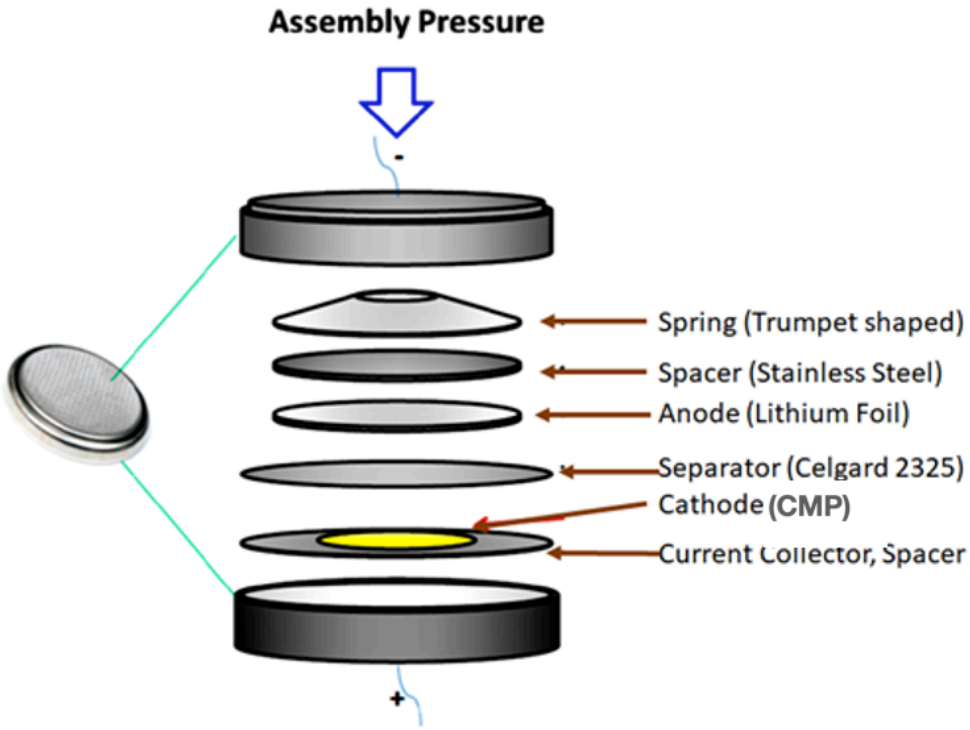

Figure 2.4 Illustration of a coin cell assembly with CMP material on the cathode

First, we need to completely dry the conductive additive (Super P) and active materials (CMP) because moisture is a critical factor in battery production. Then, the amount of active material used in the coin cell needs to be weighed out very carefully. The amount of super P depends on the electrical conductivity of our active materials. In our case, a slurry was prepared with a 6:3:1 ratio of active material to conductive additive to binder. The slurry was prepared in a mortar and pestle with the appropriate amount of NMP. It was cast on a carbon-coated Al film and then spread with a blade. The slurry coated film was then dried under vacuum overnight at 80 °C. 11mm discs were cut after drying and transferred to the glove box for battery assembling.

To assemble coin cells, the cathode disk needs to be pressed to have close contact to the stainless-steel current collectors as shown in Figure 2-4. Then, the Celgard 2325 membrane, which is used as a separator to avoid short circuits, needs to be added. After that, the lithium foil is placed and the assembly completed with a stainless steel spacer and spring on top. Finally, a larger cap is placed on top and then the coin cell is ready for electrochemical investigation.
Rate performance, Galvano-static charge discharge performance and cyclic performance was recorded using the Arbin instruments testing system (Arbin-SCTS) in a potential range of 1.5-3.5V. Cyclic voltammetry (CV) and electrochemical impedance spectroscopy (EIS) measurements were both conducted on an electrochemical workstation, VMP3 Potentiostat/Galvanostat (EG&G, Princeton Applied Research) under the potential range of 1.5-3.5V.

3. Results and discussion

3.1. Results of the synthesis of base CMP PPAAQ

In this study we aim to show how we utilize CMP PPAAQ for the energy storage applications. CMP PPAAQ was synthesized via Buchwald Hartwig (BH) cross-coupling reaction between TBPA and DAAQ as core and linker (see Figure 2-1 and 2-2 for the structures), respectively. The quinone groups from this material demonstrated high theoretical capacity for energy storage, tunable redox potentials and fast kinetics for energy storage applications, making it an attractive starting material.[123,124] Anthraquinone-based polymers have demonstrated excellent electrochemical characteristics, increased chemical stability and facilitated redox kinetics in similar applications.[125,126] From a chemistry perspective, the BH reaction opens up a simple pathway to form carbon–nitrogen bonds between aryl halides and amines. Here we have utilized the anthraquinone-based diamine linker (DAAQ, DAHQ) and various trihalide cores (TBB and TBPA) to form four types of CMPs. Good porosity and well-defined redox activity of CMPs can be reasonably designed, making them exceptionally suitable for electrochemical applications.[11,50] The details of the synthesis of PPAAQ materials is provided in Section 2.

The cross-coupling reaction between DAAQ and TBPA in toluene afforded the hybrid compound PPAAQ-Toluene as dark brown, insoluble powder and yield around 40%. FTIR, XRD and UV-VIS/NIR analyses were used to confirm successful coupling reaction, and are discussed below.

3.1.1. FT-IR Spectroscopy

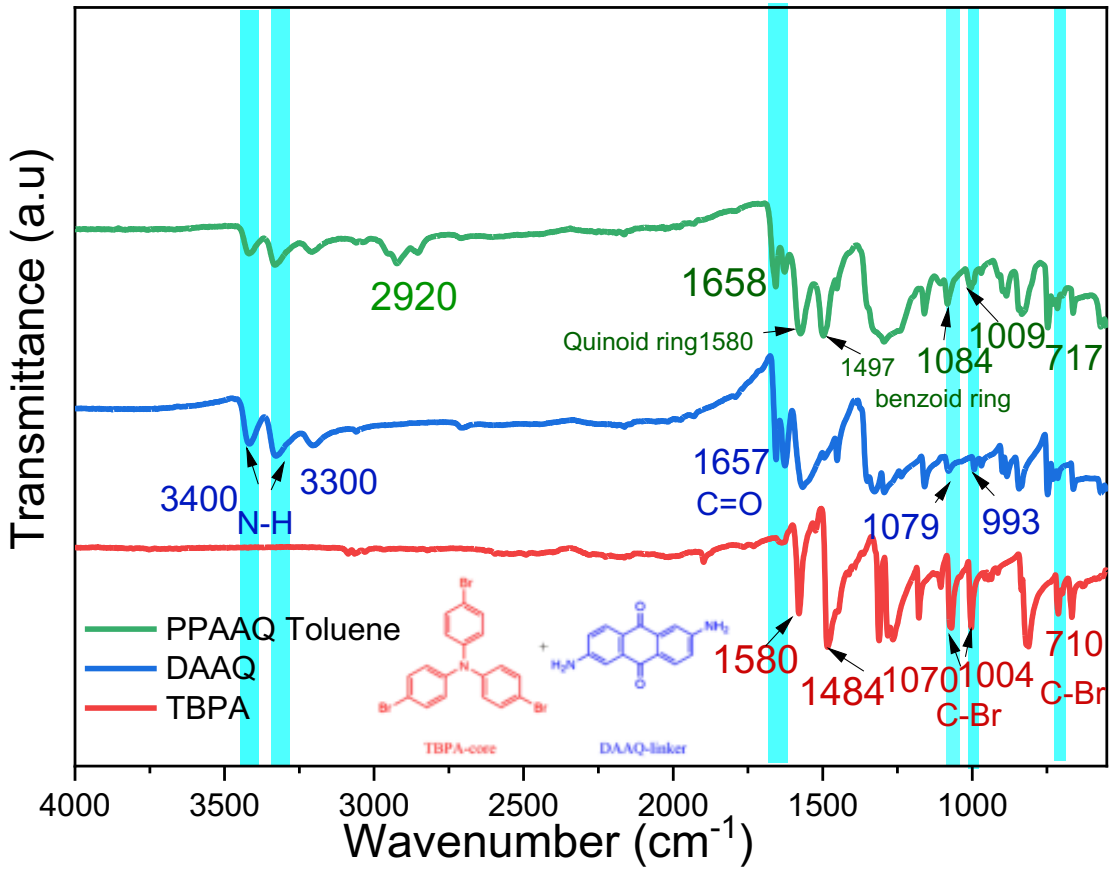

Figure 3-1 FT-IR spectrum of PPAAQ

Table 3-1 Peak affiliation of IR spectra

Peak	**Assignment**
3400-3300	-NH_2 stretching frequency
1658	C=O stretching bond
1580	C-C stretching of the quinoid ring
1497	C-C stretching of the benzenoid ring
1070, 1004, 710	C-Br bond vibration frequencies

The formation of the CMP PPAAQ-Toluene was confirmed by Fourier transform infrared (FT-IR) spectroscopy. It can be clearly seen from the Figure 3-1 that peaks at 710, 1004 and 1070 cm^{-1} are attributed to vibration frequencies of the C-Br stretching motion, which are absent from or strongly attenuated in the products. Weak peaks at 1085, 1009 and 717 cm^{-1} are attributed to C-H in plane and out-of-plane bending vibrations of the benzenoid rings, respectively.[127] The absorption peak at 1658 cm^{-1} corresponds to the C=O stretching vibration of the quinone group. The two peaks at 1580 and 1497 cm^{-1} are related to the C-C stretching of quinoid and benzenoid rings, respectively.

3.1.2. XRD investigations

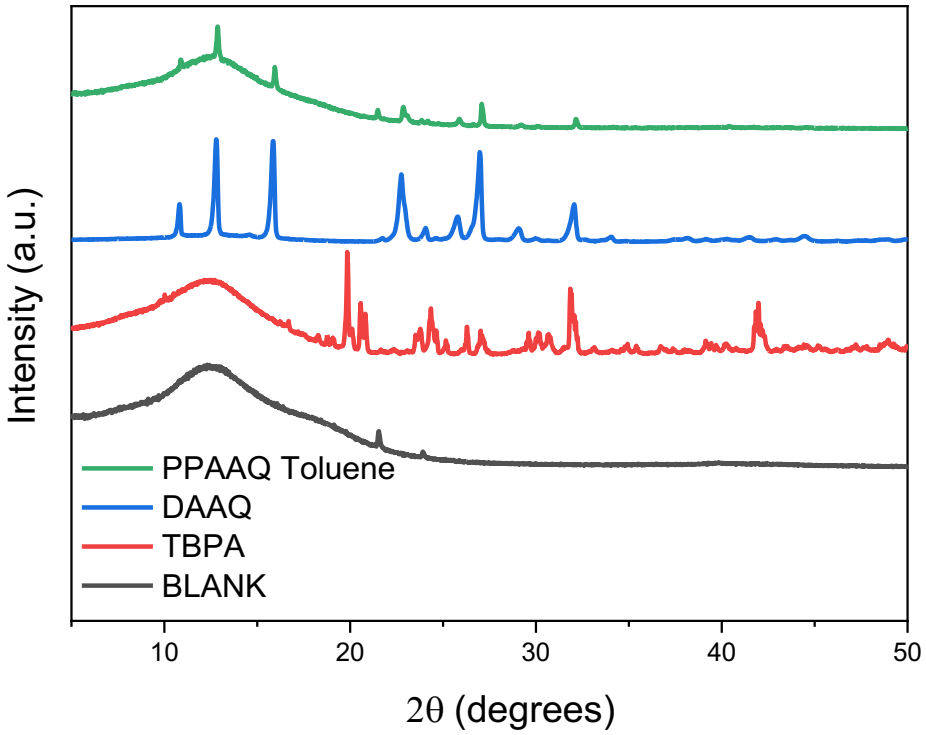

Figure 3-2 X-Ray diffraction pattern of PPAAQ, starting materials and blank sample holder.

The blank measurement was used for quality control that confirmed there was not any substances that may interfere with the analysis. The powder X-ray diffraction of PPAAQ-Toluene demonstrates that an amorphous structure was obtained for polymers, which is typical for porous organic polymers made under nonreversible conditions. However, some peaks from starting material (DAAQ) that show crystalline structure was still present in the final product, even after extensive Soxhlet extraction. The broad peak at 2θ=15 indicates repeat units within polymer chains.

3.1.3. UV-VIS/NIR Spectroscopy

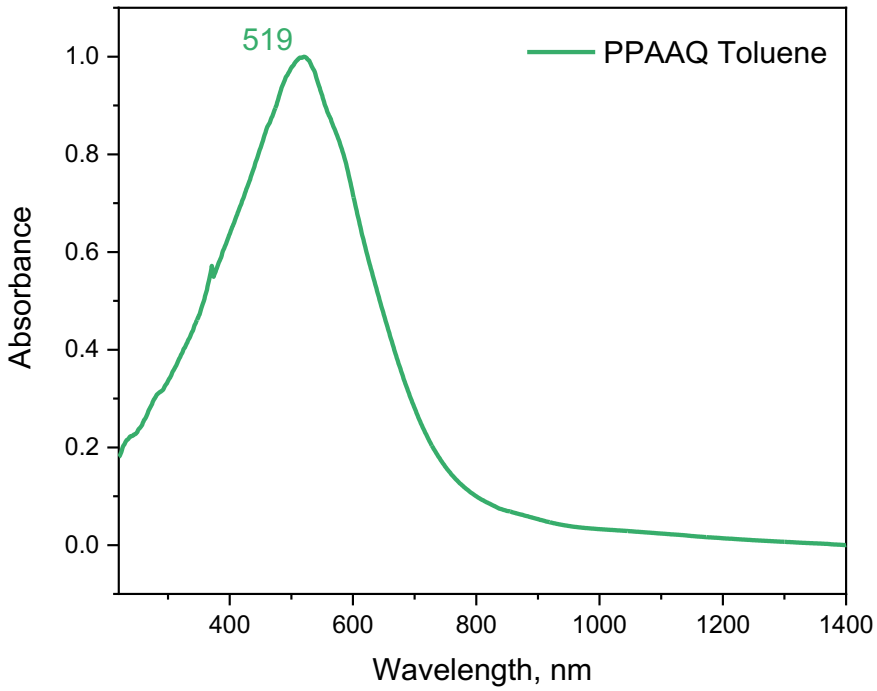

Figure 3-3 Solid-state UV-Vis/NIR spectra of PPAAQ-Toluene.

UV-Vis/NIR spectroscopy was used to prove conjugation and polymerization of our material. The PPAAQ polymer exhibits an absorption maximum at 519 nm, which is typical for amorphous CMPs. Furthermore, the shape of the absorption feature is also characteristic of such polymers.

The lower absorption maximum possibly indicates shorter conjugated structures, which could be expected when the structures of the starting materials are kept in mind.

3.1.4. Surface area characterization

A

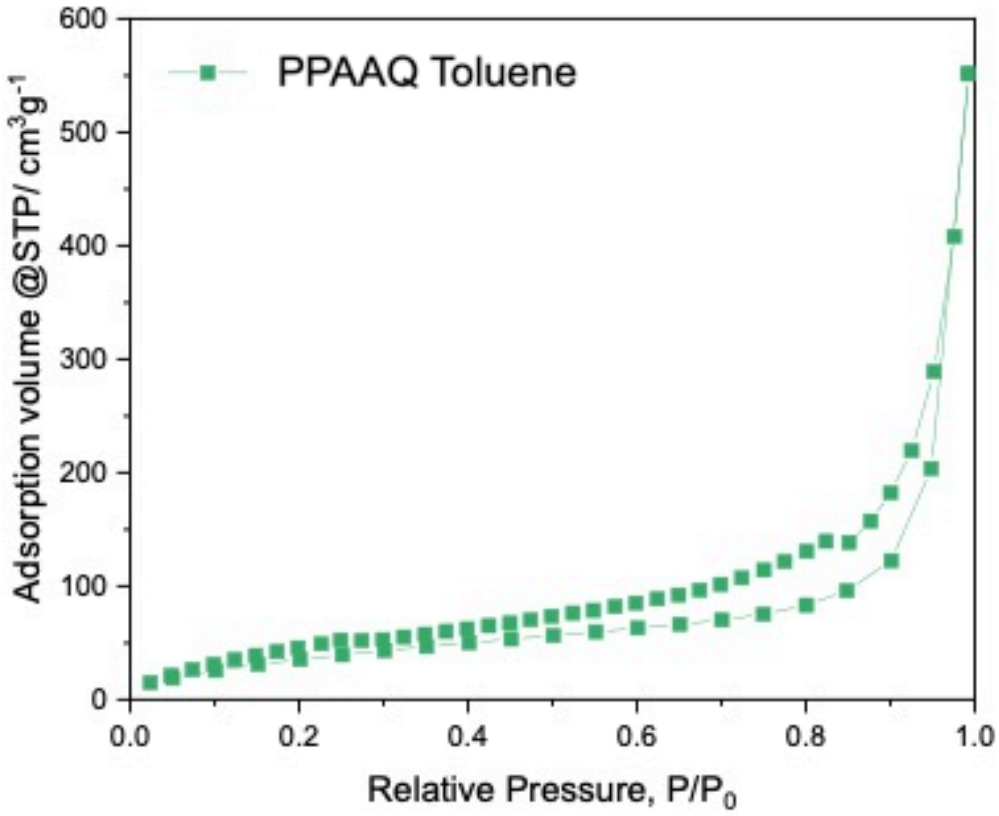

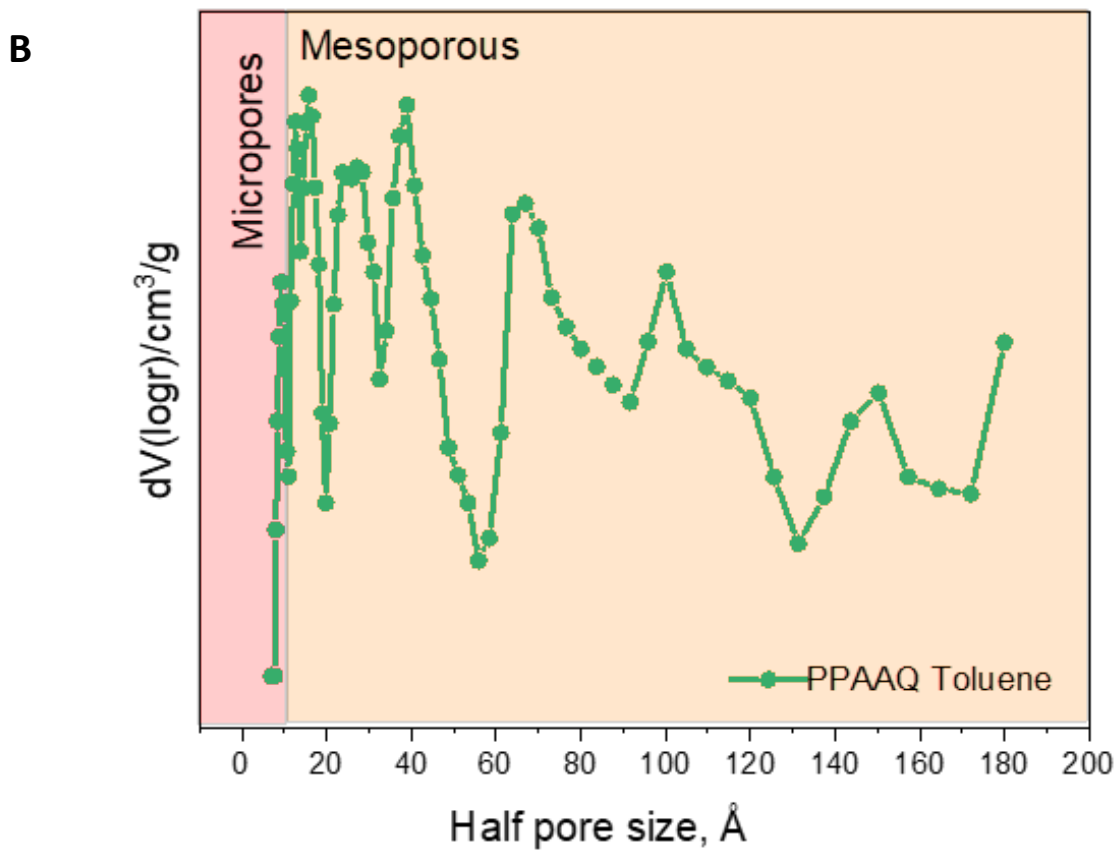

Figure 3-4 (A) N_2 adsorption/desorption isotherms and (B) pore size distribution of PPAAQ-Toluene

The N_2 adsorption/desorption isotherms of PPAAQ-Toluene are shown in Figure 3-4(a). All the isotherms were measured at 77 K by an Autosorb iQ gas adsorption analayser. According to IUPAC classification, PPAAQ-Toluene exhibits a Type III N_2 sorption isotherm. This type of isotherms is obtained when the amount of gas adsorbed increases without limit as its relative saturation approaches unity. The isotherms represented a slight increase at 0 to 0.9 relative pressure. However, after 0.9 it showed a sharp increase because of gas adsorption related to filling of macrostructure and interstitial voids. From the pore size distribution in Figure 3-4(b), it is shown that PPAAQ-Toluene have mix of micropores and mesopores. The surface area of the porous material was determined using the Brunauer-Emmett-Teller (BET) analysis technique. This is a widely-used method for measuring the surface area of porous materials, including polymers. Gas molecules are adsorbed onto the surface of the polymer at various pressures, and the amount of gas adsorbed is measured. By applying the BET equation to the resulting data, the

surface area of the material can be calculated. The surface area of the base material was found to be 142 m2/g. This value can be utilized to optimize reaction conditions and enhance other relevant physical properties.

3.2. Optimising reactions and conditions

With this initial study, the following approach was implemented. 12 PPAAQ CMPs were successfully synthesized via BH coupling reaction. These materials (at 3 different stoichiometries) were then divided into four groups according to reaction conditions. The chemical structure of the CMPs was confirmed by FT-IR spectroscopy, and amorphous nature of the polymers were determined by X-ray diffraction (see Table 3.2).

The reaction conditions were optimized to obtain high yields, achieve higher surface areas and optimize other physical properties. The theoretical yield of this reaction is calculated by the sum of core and linker and subtracting the mass of hydrogen bromide. The surface area was determined by applying the BET model to nitrogen adsorption isotherms measured at 77 K.

The comparison of yield and surface area of material under different conditions are showed in Table 3-2 The table is divided into four groups, related to the condition of the reactions. Firstly, toluene was used as a solvent without adding salt. In the second group toluene was used as well as sodium fluoride as salt additive. The purpose of adding salt was to investigate how salts may impact the reaction system. Salts were considered for their potential role as a template, or for their ability to alter the solubility parameters of the reaction solvent. To evaluate the compatibility of the polymers under investigation with different solvents, the solvent in the third group was replaced with THF from toluene. In the last group THF was used with added NaF salt. For each of these groups, the ratio between core and linker was also systematically changed – see Section 3.2.1 below for further details.

Table 3-2: Yield and surface area of PPAAQ under different conditions.

Reaction schemes	Conditions	Ratio and name	Unique Index	Yield, %	Surface area, m^2g^{-1}
1. TBPA+DAAQ PPAAQ-1	Solvent: Toluene Without NaF, 48h 110 ◦C	PPAAQ 1:1.5	DM-2	39	142
		PPAAQ 1:2	DM-3	36	20
		PPAAQ 1.5:1	DM-4	83	30
2. TBPA+DAAQ PPAAQ-2	Solvent: Toluene Add NaF, 48h, 110 ◦C	PPAAQ 1:1.5	DM-5	68	16
		PPAAQ 1:2	DM-6	74	10
		PPAAQ 1.5:1	DM-7	70	8
3. TBPA+DAAQ PPAAQ-3	Solvent: THF, without NaF, 48h,65 ◦C	PPAAQ 1:1.5	DM-19	78	35
		PPAAQ 1:2	DM-20	83	27
		PPAAQ 1.5:1	DM-21	75	71
4. TBPA+DAAQ PPAAQ-4	Solvent: THF, Add NaF, 48h,65 ◦C	PPAAQ 1:1.5	DM-8	57	17
		PPAAQ 1:2	DM-9	69	5
		PPAAQ 1.5:1	DM-10	51	10

3.2.1. Effect of different stoichiometric ratios

One of the factors explored for optimising were core and linker ratios of 1:1.5, 1:2 and 1.5:1, to find the optimal conditions for synthesis of CMPs. It can be clearly seen from Table 3-1 that the main parameters for initial assessment were yield and surface area.

The yields showed insignificant variation among stoichiometric ratios in the four groups. However, in the first group the surface area reported was the highest at 142 m^2g^{-1} for the ratio 1:1.5, while surface areas for the ratios 1:2 and 1.5:1 was 20 and 30 m^2g^{-1}, respectively.

Moreover, in the other groups the ratio 1:1.5 showed greater surface area than the 1:2 and 1.5:1 ratios.

In summary, according to Table 3-2, for all four groups the ratio 1:1.5 resulted in optimal values for yields and surface areas.

3.2.2. Effect of different solvents

In this work, initially toluene and tetrahydrofuran were used to synthesize CMPs to obtain the first materials for further investigation. Table 3-2 clearly shows results of experiments by using two different solvents.

From Table 3-2 the average yield was 61% when toluene was used, but the average percentage yield was increased by 7% when toluene was exchanged for THF. Although the yields were sufficient, the surface area was slightly higher when toluene was used. It was therefore decided to use toluene as a solvent for next stage of the investigations.

3.2.3. Effect of salt (Sodium fluoride)

The final parameter of optimisation for the Buchwald Hartwig reaction was using a salt to explore the influence on the synthesis. Based on earlier investigation,[59,120] we use NaF to determine the result of the influence of salts on the solubility parameters of the solvent. These effects could lead to simple salts controlling the porosity in CMP, to achieve high surface area and yield. Table 3-2 presents results of these investigations.

It was found that using a salt in the synthesis showed worse results than when reactions were performed without salt. For example, in the first group of polymers the surface area was 142, 20 and 30 m^2/g^{-1}, respectively, while in the second group when salt was used the surface area decreased to 16, 10 and 8 m^2/g^{-1}, respectively. Identical results were found for the third and fourth groups, where THF was used as a solvent. In this case, experiments without salt yielded greater surface areas than those where sodium fluoride was used.

3.3. Hansen solubility parameters and optimizing materials design

3.3.1. PPAAQ

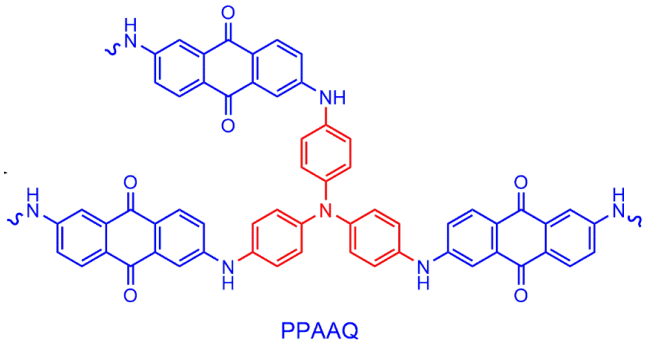

Scheme 3-1 PPAAQ base material

It was at this stage that HSPs become available as a tool in the Faul research group. After optimizing reactions and conditions we decided to calculate HSPs to find theoretically the most compatible solvents. Identifying compatible solvents will help to achieve high yield and surface area, as well as provide opportunities to tune the functionality of the CMPs. There are three parameters that are needed to calculate total HSP values**,** δ_T: The energy from dipolar intermolecular force between molecules, δ_P, the energy from dispersion forces between molecules, δ_D and the energy from hydrogen bonds between molecules, δ_H**.** Table 3-3 represent a list of solvents that was used in this work with their characteristics HSPs, taken from published data.[128] Moreover, this table showed differences, $|\Delta\delta_T|$ between HSPs of polymers and solvents. Figure 3-5 shows a B-spline fitting of HSPs against maximum UV/Vis absorbance of the insoluble polymers dispersed in various solvents. The maximum from the B-spline fitting corresponds to the solubility parameter of the polymer.

PPAAQ-Toluene was chosen as a base material for designing new polymers Scheme 3-1, with the main reaction presented in Part 2.4.1 (Scheme 2-4). It was determined that two solvents would have a close match in their Hansen solubility parameters (HSPs) to the synthesized CMP

materials, and these solvents were found to be a close match. DMSO show the lowest difference in value of $\mathbf{|\Delta\delta_T|=0.16}$, indicating it is the most appropriate solvent for PPAAQ.

However, if we consider another peak value Figure 3-5 where the polymers PPAAQ $\mathbf{\Delta\delta_T}$ value is 22.94, the difference for NMP would be only $|\Delta\delta T|=0.01$. As a result, we used DMSO and NMP solvents to synthesize PPAAQ and investigate the influence of matching HSPs on CMP synthesis. Section 2 provides more detailed information on the calculation of HSPs.

Table 3-3 List of used solvents

Sl No.	Solvents	δ_D[a]	δ_P[b]	δ_H[c]	δ_T[d]	$\lvert\Delta\delta_T\rvert$
1	***Dimethyl Sulfoxide (DMSO)***	***18.4***	***16.4***	***10.2***	***26.67***	***0.16***
2	Dimethylformamide (DMF)	17.4	13.7	11.3	24.86	1.97
3	Acetonitrile	15.3	18	6.1	24.39	2.44
4	***N-Methyl-2-pyrrolidone (NMP)***	***18***	***12.3***	***7.2***	***22.95***	***3.88***
5	1-methylimidazole	20.6	14.9	11	27.7	0.87
6	Dimethylacetamide	16.8	11.5	9.4	22.42	4.41
7	Propylene carbonate	20	18	4.1	27.22	0.39
8	Quinoline	20	5.6	5.7	21.53	5.3
9	Acetone	15.5	10.4	7	19.93	6.9
10	Xylene	17.8	1	3.1	18.09	8.74
11	Toluene	18	1.4	2	18.16	8.67
12	Ethanol	15.8	8.8	19.4	26.52	0.31
13	Dioxane	17.5	1.8	9	19.76	7.07
14	***PPAAQ***	***17.96***	***15.73***	***10.46***	***26.83***	

[a] δ_D = dipolar interaction parameter. [b] δ_P = the permanent dipole interaction parameter. [c] δ_H = the hydrogen-bonding interaction parameter, [d] δ_T = the total Hansen solubility parameter.

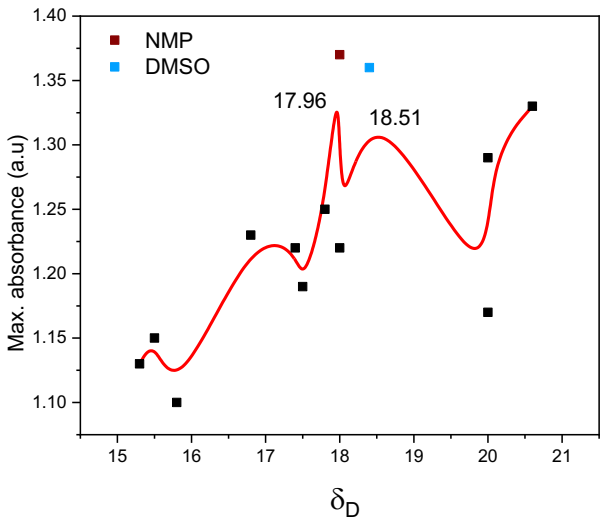

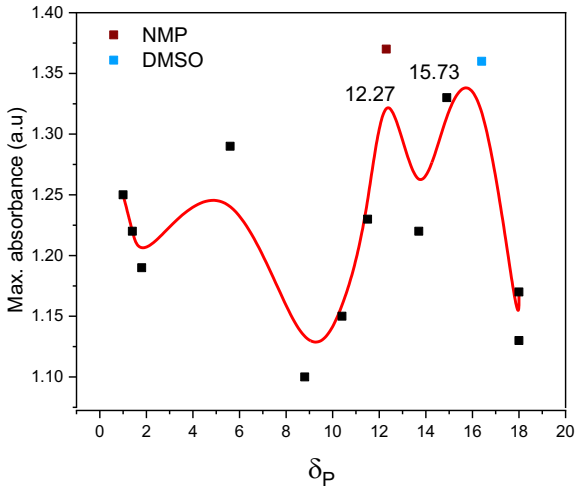

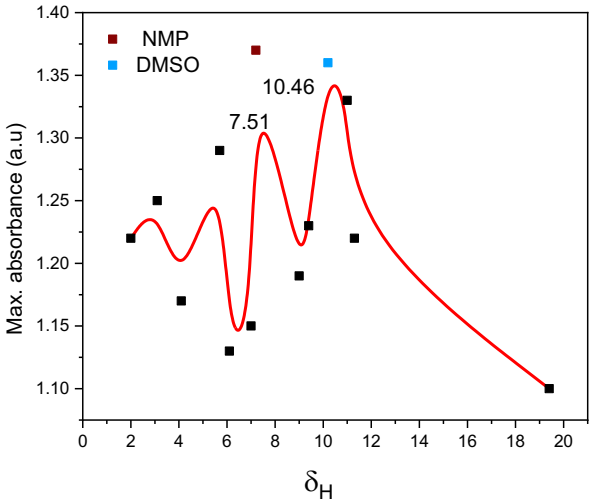

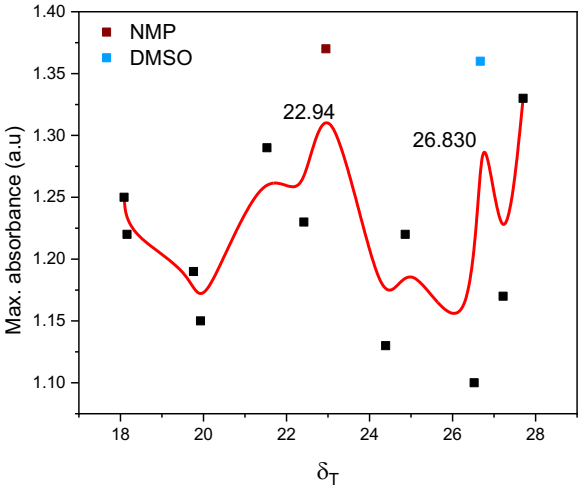

Figure 3-5 B-spline curve of δ_D (a), δ_P (b), δ_H (c) and δ_T(d) of PPAAQ-Toluene

3.3.1.1. FT-IR spectroscopy of PPAAQ-based materials

With this information available, these newly selected solvents DMSO and NMP were now employed for the synthesis of PPAAQ-based materials.

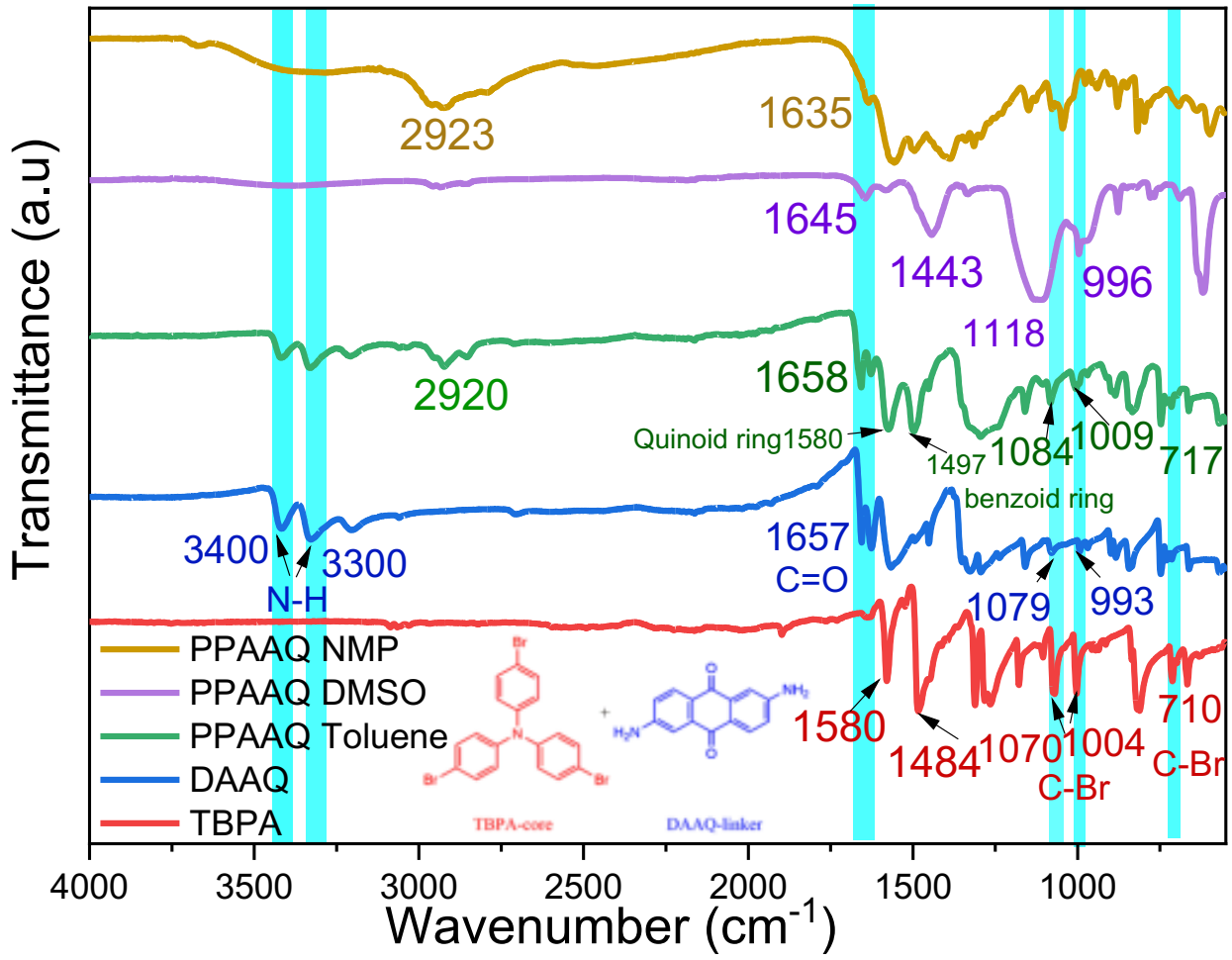

Figure 3-6 FTIR spectra of PPAAQ synthesized in different solvents

The formation of CMPs was confirmed by FT-IR spectroscopy. It is clearly seen from Figure 3-6 that all three polymers have carbonyl groups. Also, FTIR investigations confirmed the presence of benzenoid rings in products from these reactions. However, PPAAQ-Toluene has peaks that belong to primary amine groups whereas in PPAAQ DMSO and PPAAQ NMP no vibrations from

this group are presented in their spectra. PPAAQ-Toluene and PPAAQ NMP have similar peaks at around 2923 cm^{-1} that show C-H bonds. Weak peaks at around 700, 1000 and 1100 cm^{-1} can be assigned to C-H in-plane and out-of-plane bending vibrations of benzenoid rings.

3.3.1.2. XRD studies of PPAAQ-based materials

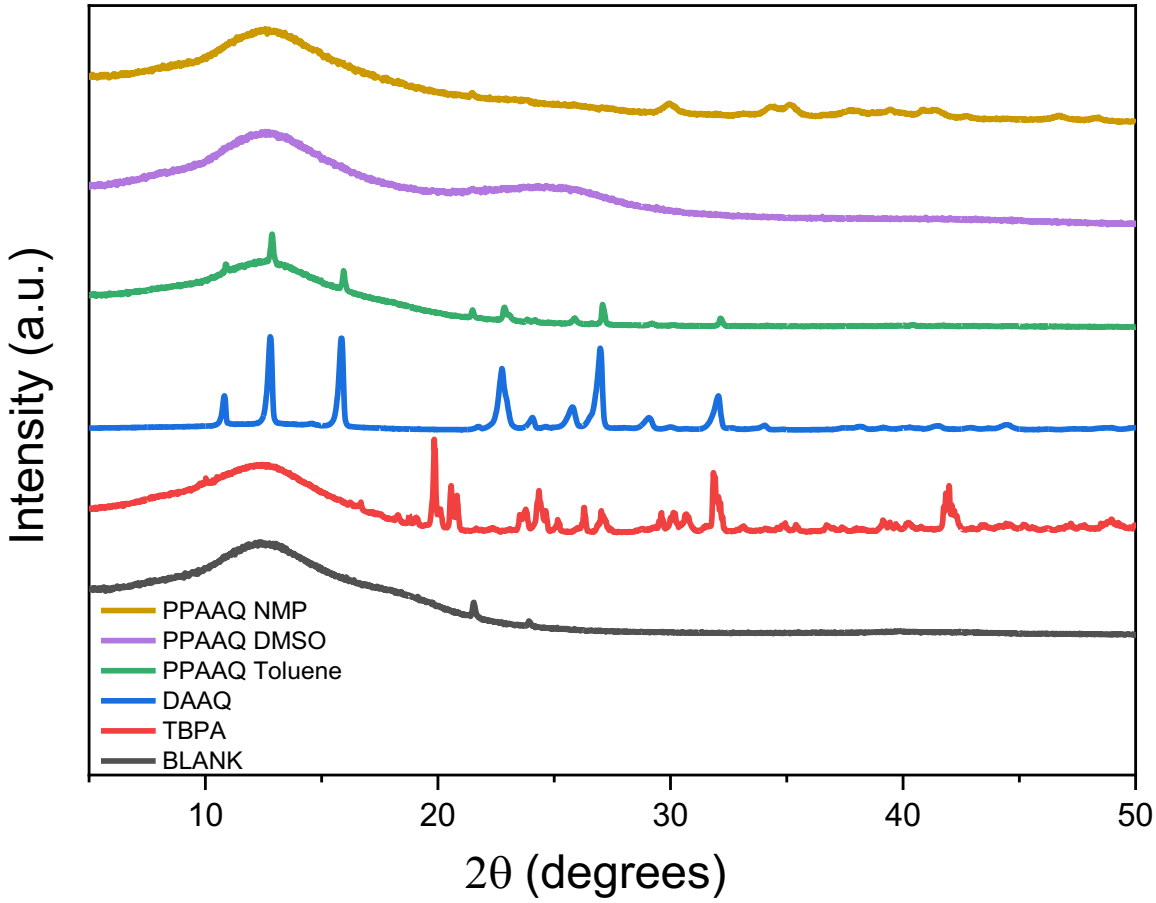

Figure 3-7 XRD spectrum of PPAAQ synthesized in different solvents.

The powder X-ray diffraction demonstrates amorphous structure for PPAAQ DMSO which is typical for porous organic polymers made under nonreversible conditions. The broad peak 25 degrees in 2θ for PPAAQ DMSO indicates π–π stacking, most probably because of the presence of the anthraquinone moieties. PPAAQ NMP and Toluene have semicrystalline structures and the broad peak at 2θ=15 indicates repeat units within polymer chains. Also, PPAAQ Toluene possess

peaks that belongs to starting material DAAQ, while PPAAQ NMP shows peaks at higher angles that fits with reflections from the TBPA starting materials.

3.3.1.3. UV-Vis/NIR investigations

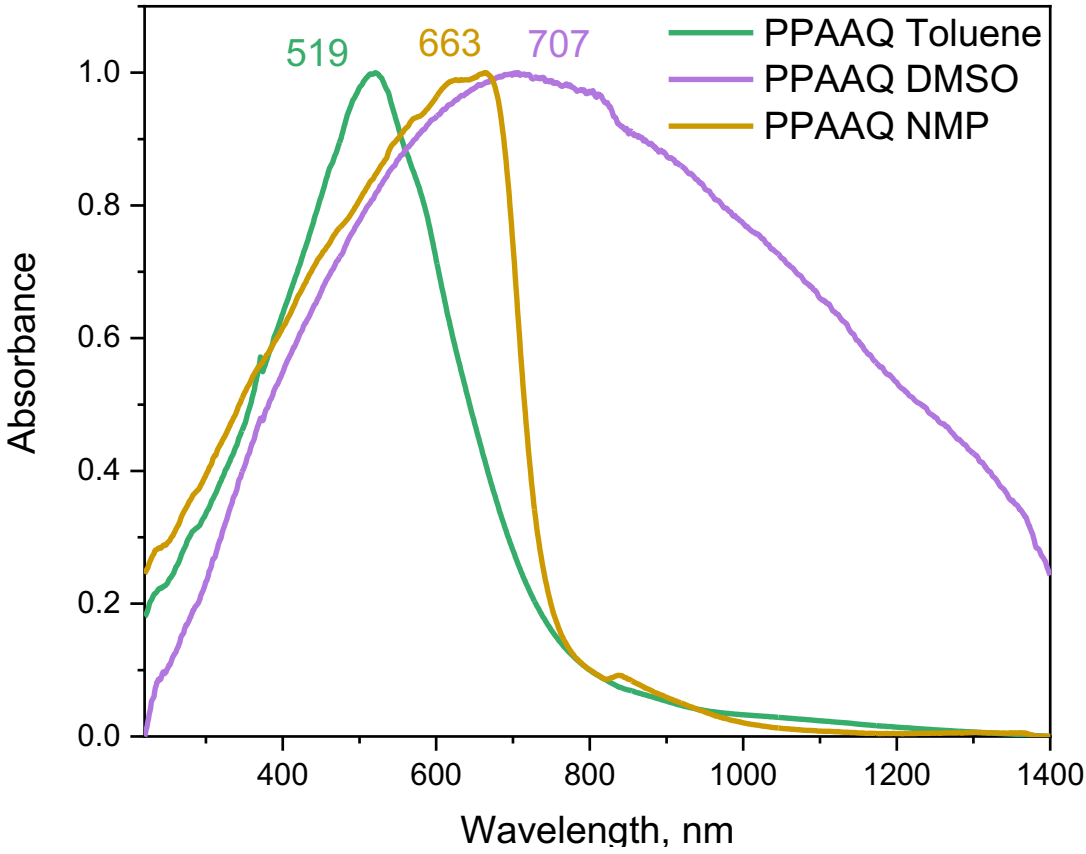

Figure 3-8 Solid state UV-Vis/NIR spectra of PPAAQ synthesized in different solvents

Solid state UV-vis absorbance can be measured using a UV-vis spectrophotometer equipped with a diffuse reflectance accessory (DRA). The sample is ground into a fine powder and pressed into a pellet, which is then placed on the DRA. The DRA reflects the light from the spectrophotometer off the surface of the sample at all angles, allowing for measurement of the diffuse reflectance spectrum. The absorbance spectrum can then be calculated using the Kubelka-Munk equation, which relates the diffuse reflectance to the absorption coefficient of the sample.

Solid-state UV-Vis/NIR spectroscopy reveals that the PPAAQ mainly exhibits one peak. The maximum wavelength is 519 nm for PPAAQ-Toluene, 663 nm for PPAAQ NMP and 707 nm for PPAAQ DMSO. Longer wavelengths that show longer conjugation for PPPAAQ DMSO is present. Also, the PPAAQ DMSO structure shows π–π stacking because of anthraquinone moieties present, with a strong bathochromic shift owing to the extended conjugation.

3.3.1.4. SEM morphological investigations

The surface morphologies of PPAAQ were researched using SEM, as shown in Figure 3-9. It can be seen from Image 3-9 (a) that PPAAQ-Toluene have irregular nanoparticles ranging in size from 2 um to 20 um. PPAAQ DMSO and PPAAQ NMP have mostly amorphous structures. PPAAQ DMSO possess spherical particles in the size range 20 um to 50 um. PPAAQ NMP exhibited plate-like particulates, ranging in sizes from 2 to 15 um. In a few cases thin fibre-like structures can also be seen.

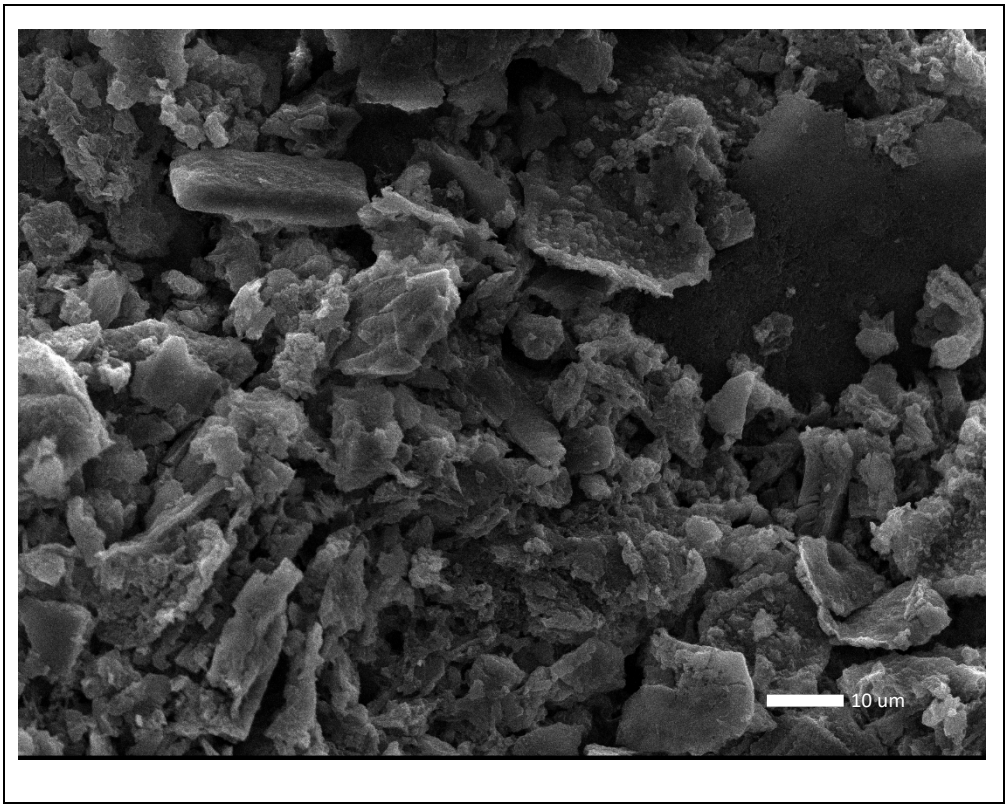

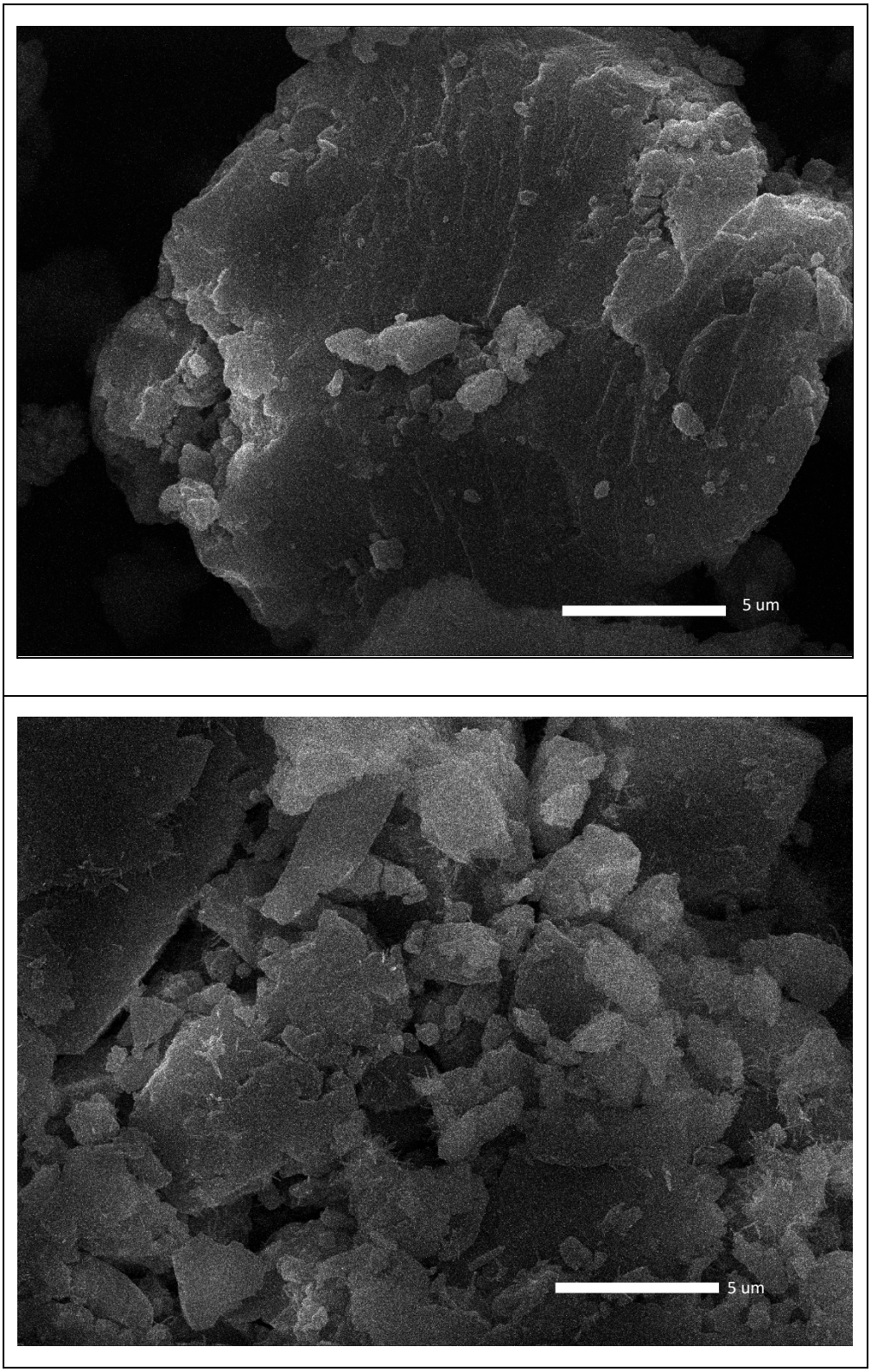

Figure 3-9 SEM images of (a) PPAAQ-Toluene, (b) PPAAQ DMSO and (c) PPAAQ NMP

3.3.1.5. Surface area characterization

Figure 3-10(a) represent the N_2 adsorption/desorption isotherms of PPAAQ prepared in three solvents. According to IUPAC classification, these sorption isotherms correspond to Type III, which mean multilayer formation of adsorbed gas molecules. PPAAQ NMP isotherms show low adsorption volumes until 100 cm^3/g, whereas PPAAQ DMSO and PPAAQ-Toluene reach 300 and 500 cm^3/g, respectively.

In accordance with pore size distribution Figure 3-10(b), it shows the presence of microporous and mesoporous structure.

The highest BET surface area was found for PPAAQ-Toluene at 142 m^2/g Table 3-4. In this case, the optimization of HSPs did not yield the expected results, as all physical property indicators were found to be lower than anticipated. Nevertheless, it was predicted that the utilization of new solvents could potentially enhance the surface area. it was decided to change the core of the starting material for further investigations.

A

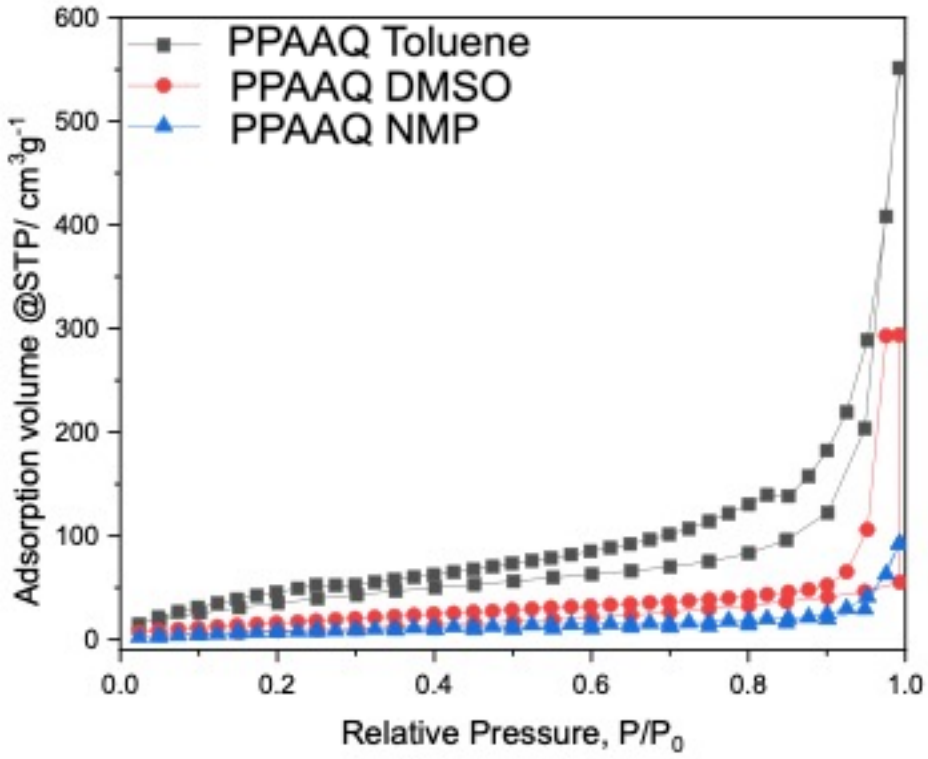

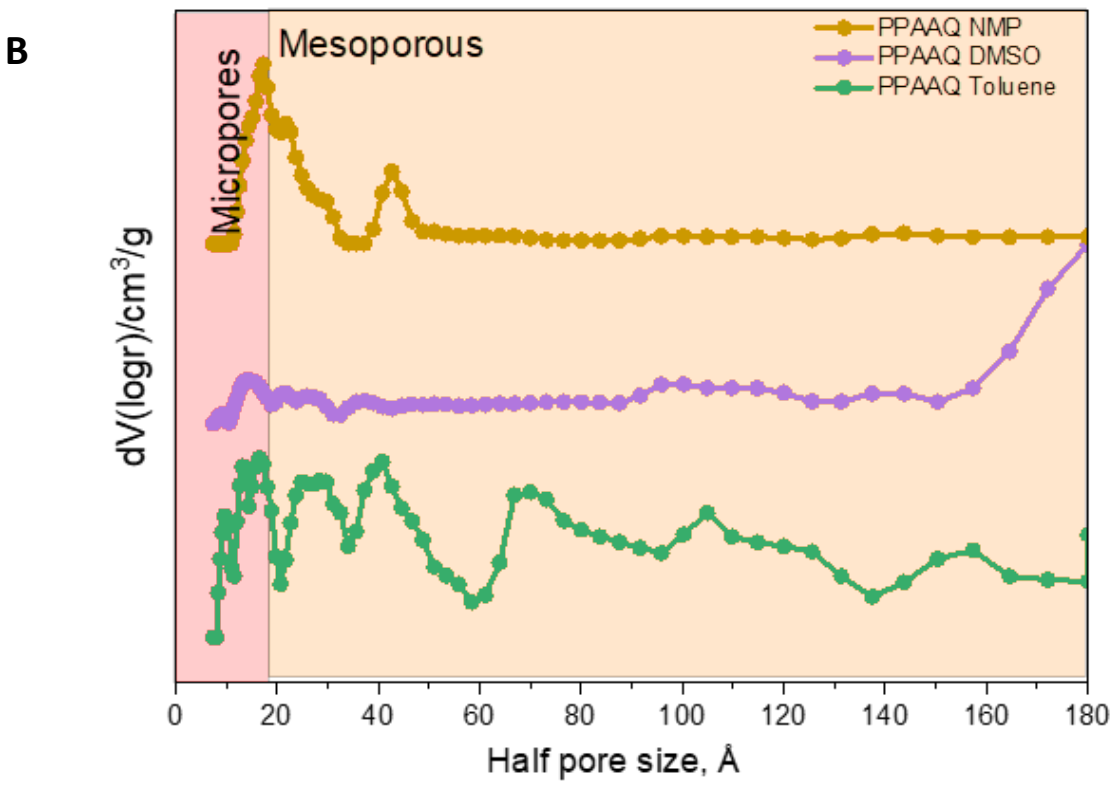

Figure 3-10 (A) Isotherms and (B) pore size distribution of PPAAQ with different solvent

Table 3-4 BET surface area of PPAAQ

Sample	S BET, m^2/g	Total pore volume DFT cm^3/g
PPAAQ-Toluene	142	0.051
PPAAQ DMSO	35	0.002
PPAAQ NMP	6	0.0001

3.3.2. PolyBenzeneAntriQuinone (PBAQ)

PBAQ is a material that is made from the TBB-core and DAAQ linker as shown in Scheme 3-2. It was of interest to change the core to see how it will impact to properties of material. The base polymer was produced by synthesis as described in Section 2.4.2. This new standard polymer was used to explore and analyse HSPs to find appropriate solvents for attempts to further optimize these materials. As in the previous part, the procedure for the calculation of HSPs is showed in Section 3. The three main parameters (δ_D; δ_P; δ_H) and total HSPs (δ_T) of solvents and PBAQ are presented in Table 3-5. Figure 3-11 shows the B-spline fitting of HSPs against the maximum UV-Vis absorbance. The maximum of the B-spline fitting indicates the solubility parameter of the polymer.

According to our investigation, the most applicable solvent is NMP because its $|\Delta\delta T|$ value is less than 1 (and equal to 0.14, see Table 3.4.). Another solvent that fulfills the given condition is dimethylacetamide (DMA), with its $|\Delta\delta T|$ value = 0.39. Thus, both NMP and DMA were chosen for further investigation.

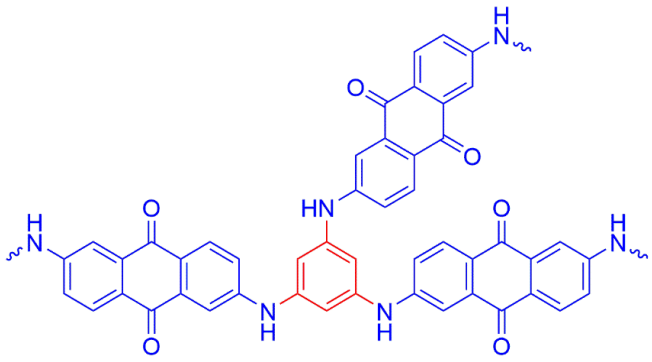

PBAQ

Scheme 3-2 PBAQ with TBB-core and DAAQ linker

Table 3-5 HSPs of solvents and polymer PBAQ

Sl No.	Solvents	δ_D[a]	δ_P[b]	δ_H[c]	δ_T[d]	$\lvert\Delta\delta_T\rvert$
1	Quinoline	20	5.6	5.7	21.53	1.28
2	***NMP***	***18***	***12.3***	***7.2***	***22.95***	***0.14***
3	DMSO	18.4	16.4	10.2	26.67	3.86
4	Propylene carbonate	20	18	4.1	27.22	4.41
5	Dioxane	17.5	1.8	9	19.76	3.05
6	DMF	17.4	13.7	11.3	24.86	2.05
7	1-methylimidazole	20.6	14.9	11	27.7	4.89
8	Acetonitrile	15.3	18	6.1	24.39	1.58
9	Xylene	17.8	1	3.1	18.09	4.72
10	Ethanol	15.8	8.8	19.4	26.52	3.71
11	Toluene	18	1.4	2	18.16	4.65
12	***Dimethylacetamide***	***16.8***	***11.5***	***9.4***	***22.42***	***0.39***
13	Acetone	15.5	10.4	7	19.93	2.88
14	m-cresol	17.96	15.73	10.46	26.06	3.25
15	***PBAQ***	***17.17***	***12.45***	***7.52***	***22.81***	

[a] δ_D = dipolar interaction parameter. [b] δ_P = the permanent dipole interaction parameter. [c] δ_H = the hydrogen-bonding interaction parameter, [d] δ_T = the total Hansen solubility parameter.

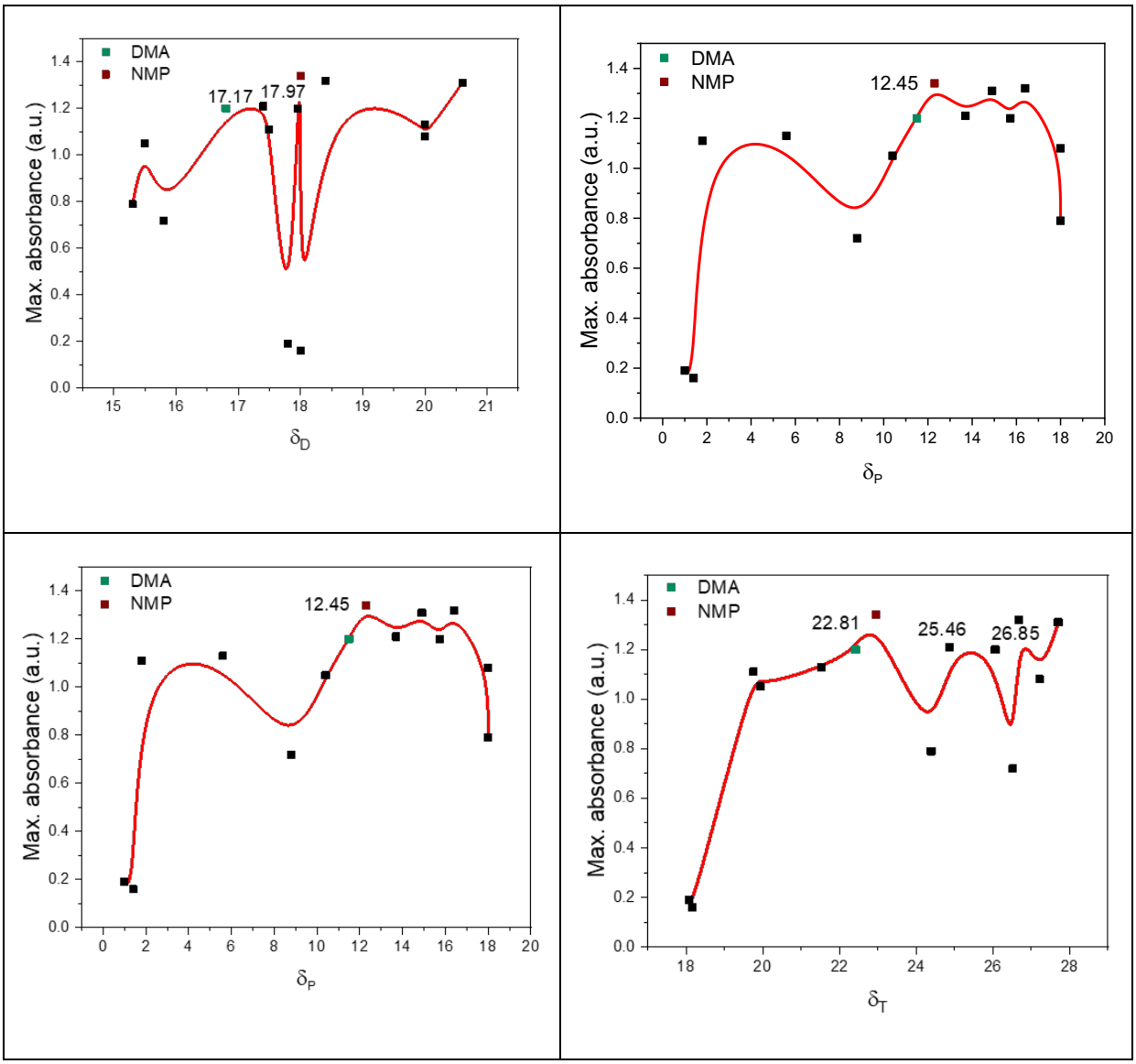

Figure 3-11 B-spline curve of δ_D (a), δ_P (b), δ_H (c) and δ_T(d) of PBAQ Toluene

3.3.2.1. FT-IR Investigations

The successful synthesis of PBAQ was confirmed by FT-IR spectroscopy, see Figure 3-12. First, peaks at 738 and 1096 cm^{-1} are assigned to vibration frequencies originating from C-Br bonds, which are absent from the spectra of the products. Weak peaks in the same region in PBAQ toluene and PBAQ NMP are assigned to C-H in plane and out-of-plane bending vibrations of benzenoid rings. Secondly, N-H stretching band at 3400 and 3300 cm^{-1} are absent from PBAQ DMA and PBAQ NMP. PBAQ Toluene still have N-H signals present. It can be clearly seen that all three polymers have a benzenoid ring at around 1420 cm^{-1}. Table 3-6 presents key peaks and their assignments.

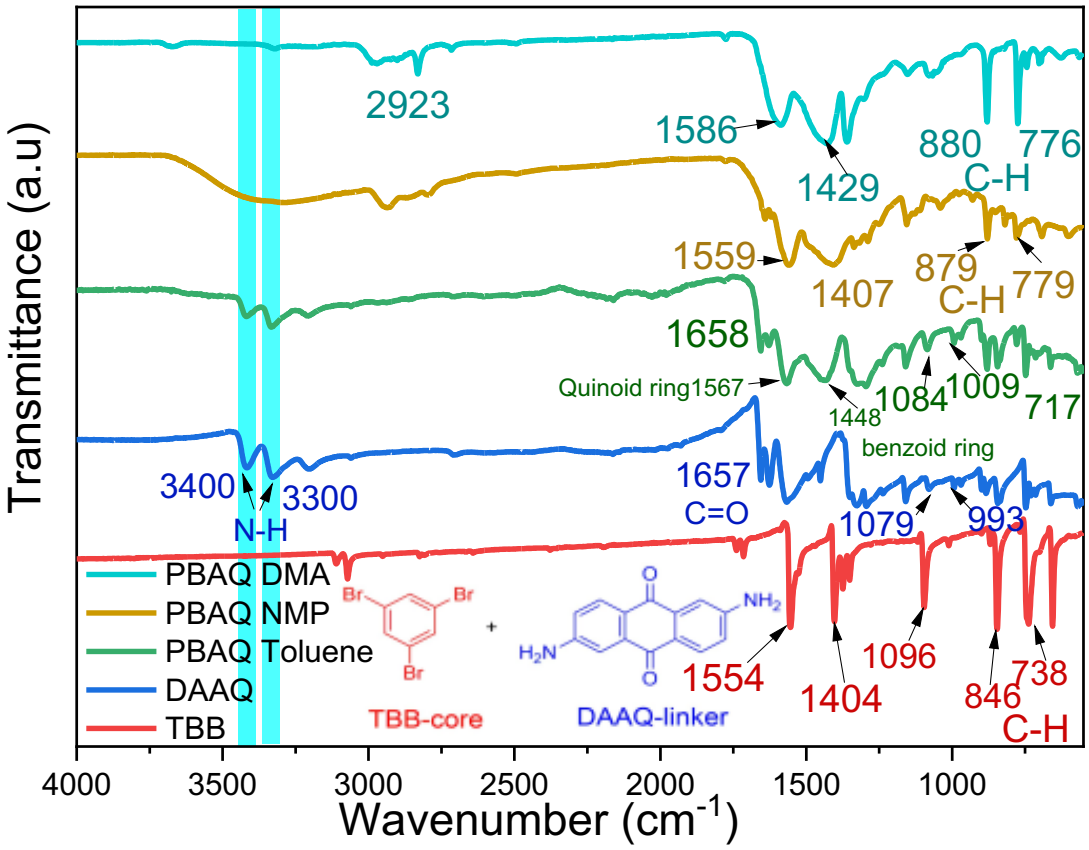

Figure 3-12 FT-IR spectra of PBAQ materials (including starting materials)

Table 3-6 FTIR Peak assignments (from Figure 3-12)

Peak (cm^{-1})	**Assignment**
3400-3300	-NH_2 stretching frequency
1658	C=O stretching bond
1580	Quinoid ring
1497	Benzoid ring
1096, 738	C-Br vibration frequencies

3.3.2.2. XRD investigations

The powder X-ray diffraction data in Figure 3-13 are different for all three polymers. PBAQ Toluene and PBAQ DMA have a broad peak at 15°, which is assigned to a lack of order in the arrangement of the materials' structure, causing the X-rays to scatter in many directions. PBAQ Toluene have weak peaks that can be assigned to the starting material DAAQ. PBAQ NMP have a series of peaks beyond 30 degrees, that probably belongs to TBB used in synthesis process. PBAQ DMA shows a mostly amorphous structure, with the exception of one peak at around 26°, consigned to π–π stacking, and a broad peak at $2\theta=10-17°$, similar to that found for other polymers.

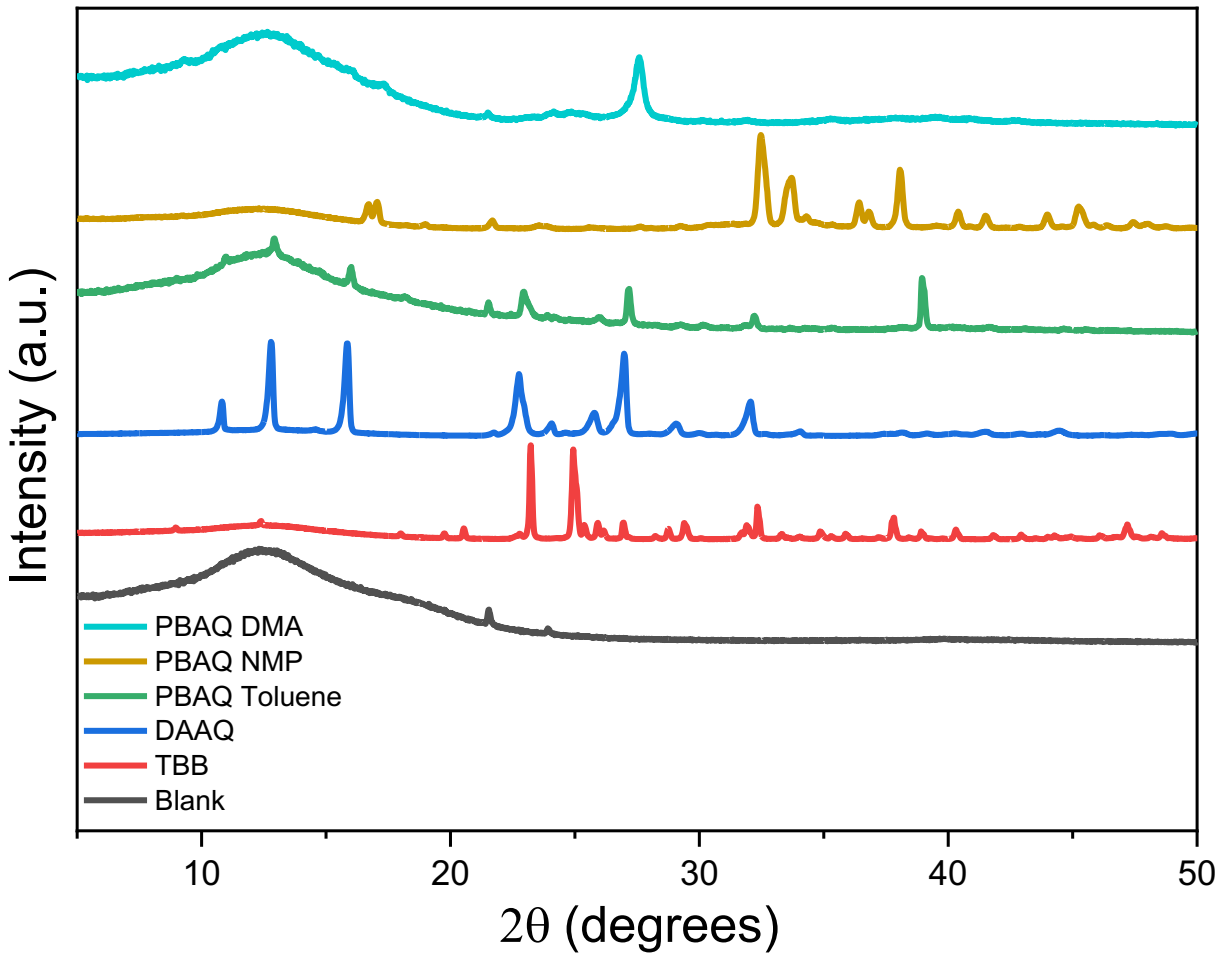

Figure 3-13 XRD spectra of PBAQ

3.3.2.3. UV-Vis/NIR investigations

Solid-state UV-Vis/NIR spectroscopy was used to confirm the existence of conjugation because UV-Vis/NIR shows extended absorption only if conjugated pi-electron systems are present. Solid state UV-Vis/NIR spectra of PBAQ (Figure 3-14) reveal that PBAQ mainly exhibited one peak. The maximum wavelength is 509 nm for PBAQ Toluene, 348 nm for PBAQ NMP and 666 nm for PBAQ DMA. The red-shifted wavelengths for PBAQ Toluene and PBZQ DMA indicate the presence of larger conjugated sections within the synthesised materials. In the case of PBZQ NMP, the short wavelength maximum indicates a lack of conjugation in the prepared material.

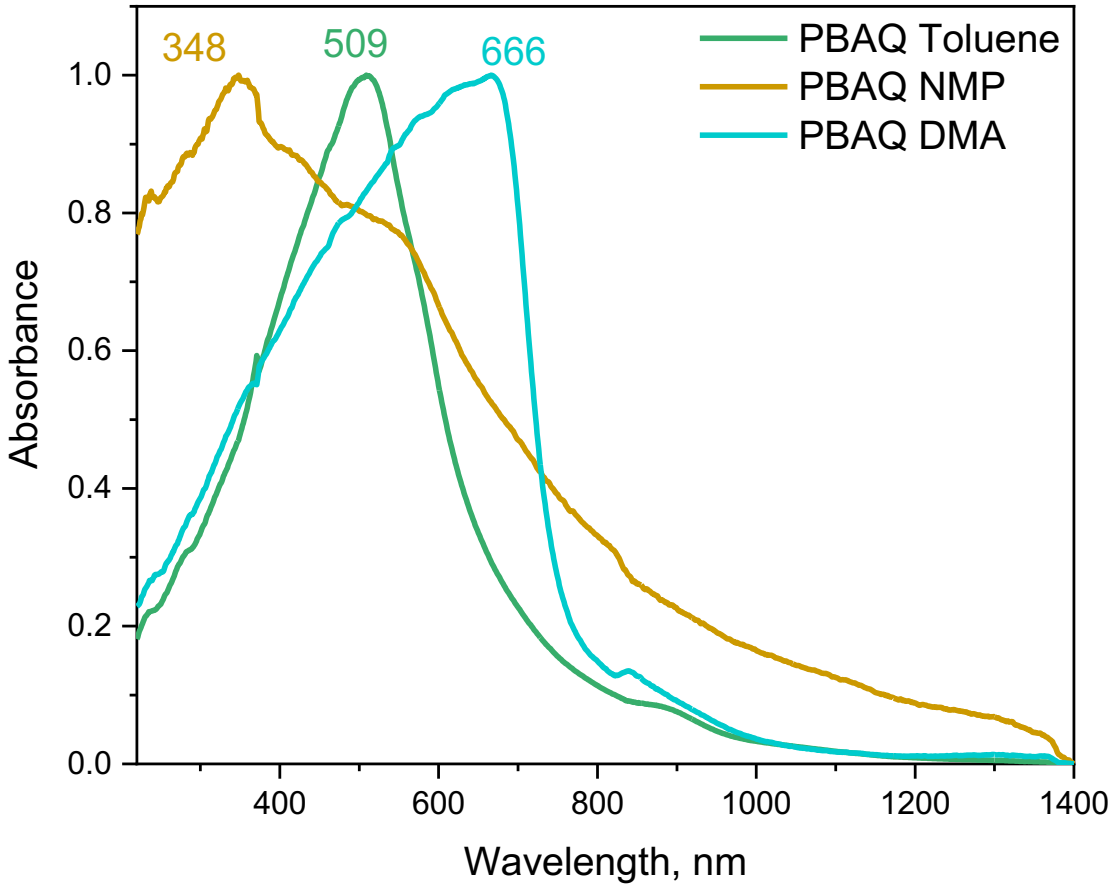

Figure 3-14 Solid state UV-Vis/NIR spectra of PBAQ with different solvent

3.3.2.4. Surface area characterization

Figure 3-15(a) represent the N_2 adsorption/desorption isotherms of PBAQ in three solvents. According to IUPAC classification, these sorption isotherms correspond to Type III. This isotherm is obtained when the amount of gas adsorbed increases without limit as its relative saturation approaches unity. PBAQ NMP isotherms show low adsorption volumes until 25 cm^3/g, whereas PBAQ Tolune and PBAQ DMA reach 100 and 200 cm^3/g, respectively.

In accordance with the pore size distribution Figure 3-15(b), it shows the presence microporous and mesoporous structure. PBAQ toluene and PBAQ NMP have a slight predominance of mesoporous. When DMA was used as solvent, the mesoporous content dramatically increased.

The highest BET surface area was found for PBAQ-Toluene at 32 m^2/g Table 3-7. The lowest BET surface area shows PBAQ NMP 8.5 m^2/g. Optimising HSP did not yield good results, therefore we continued change structure of CMP material.

Table 3-7 BET surface area of PBAQ

Sample	S BET, m^2/g	Total pore volume DFT cm^3/g
PBAQ-Toluene	32	0.009
PBAQ NMP	8.5	0.002
PBAQ DMA	30	0.01

A

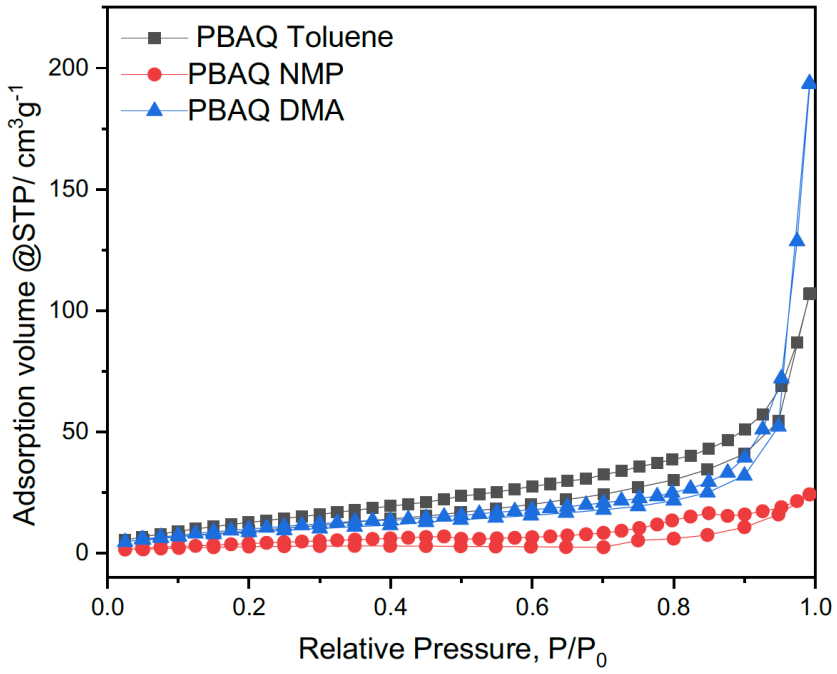

B

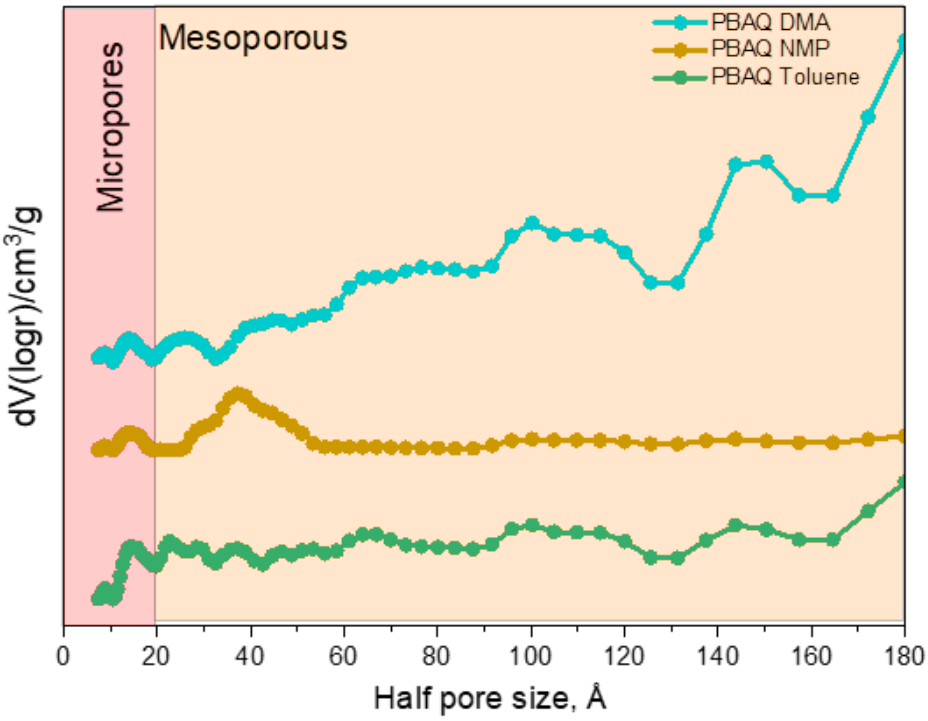

Figure 3-15 (**A**) Isotherms and (**B**) pore size distribution of PBAQ with different solvent

3.3.3. PolyPhenylAminoHydroQuinone (PPAHQ)

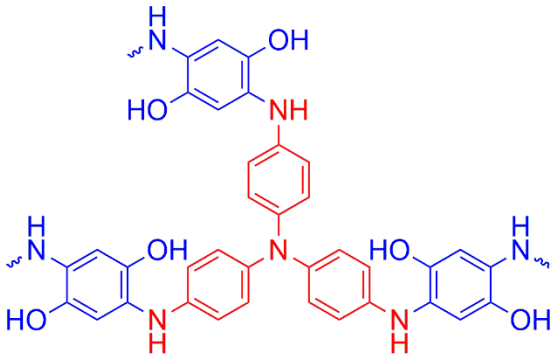

PPAHQ

Scheme 3-3 PPAHQ with TBPA-core and DAHQ linker

In this section we replaced the linker from the first polymer, DAAQ, with DAHQ (see Scheme 3-3 for structures) but kept the TBPA core. This approach provides an opportunity to investigate how the polymer will perform if prepared with a short linker. The synthesis of PPAHQ polymer was

performed in accordance with Part 2.4.3. HSPs were calculated to find the most suitable solvents for the preparation of this new polymer. The process for the calculation of the HSPs is reported in Part 2.3. Results of this study are shown in the Table 3-8 and Figure 3-16.

It is obvious from the Table 3-7 that DMSO have good compatibility with the polymer PPAHQ with a total HSP 26.67, with a difference between $\boldsymbol{\delta_T}$ of polymer and DMSO less than 1 (0.04). Ethanol showed good compatibility, with $|\Delta\delta T|=0.19$, as shown in Figure 3-16(d). The location of both DMSO and ethanol is close to highest peak that belongs to PPAHQ, indicating possible matches as good solvents. However, there are big deviations in the values of the polar components of $\boldsymbol{\delta_T}$, with, for example, $\boldsymbol{\delta_H}$ for these two solvents, which should be kept in mind as well: 10.2 for DMSO and 19.4 for ethanol, respectively.

Table 3-8 HSPs of solvents and polymer PPAHQ

Sl No.	Solvents	δ_D[a]	δ_P[b]	δ_H[c]	δ_T[d]	$\lvert\Delta\delta_T\rvert$
1	Quinoline	20	5.6	5.7	21.53	5.18
2	NMP	18	12.3	7.2	22.95	3.76
3	***DMSO***	***18.4***	***16.4***	***10.2***	***26.67***	***0.04***
4	Propylene carbonate	20	18	4.1	27.22	0.51
5	Dioxane	17.5	1.8	9	19.76	6.95
6	DMF	17.4	13.7	11.3	24.86	1.85
7	1-methylimidazole	20.6	14.9	11	27.7	0.99
8	Acetonitrile	15.3	18	6.1	24.39	2.32
9	Xylene	17.8	1	3.1	18.09	8.62
10	***Ethanol***	***15.8***	***8.8***	***19.4***	***26.52***	***0.19***
11	Toluene	18	1.4	2	18.16	8.55
12	Dimethylacetamide	16.8	11.5	9.4	22.42	4.29
13	Acetone	15.5	10.4	7	19.93	6.78
14	m-cresol	17.96	15.73	10.46	26.06	0.65
15	***PPAHQ***	***17.36***	***16.26***	***10.2***	***26.71***	

[a] δ_D = dipolar interaction parameter. [b] δ_P = the permanent dipole interaction parameter. [c] δ_H = the hydrogen-bonding interaction parameter, [d] δ_T = the total Hansen solubility parameter.

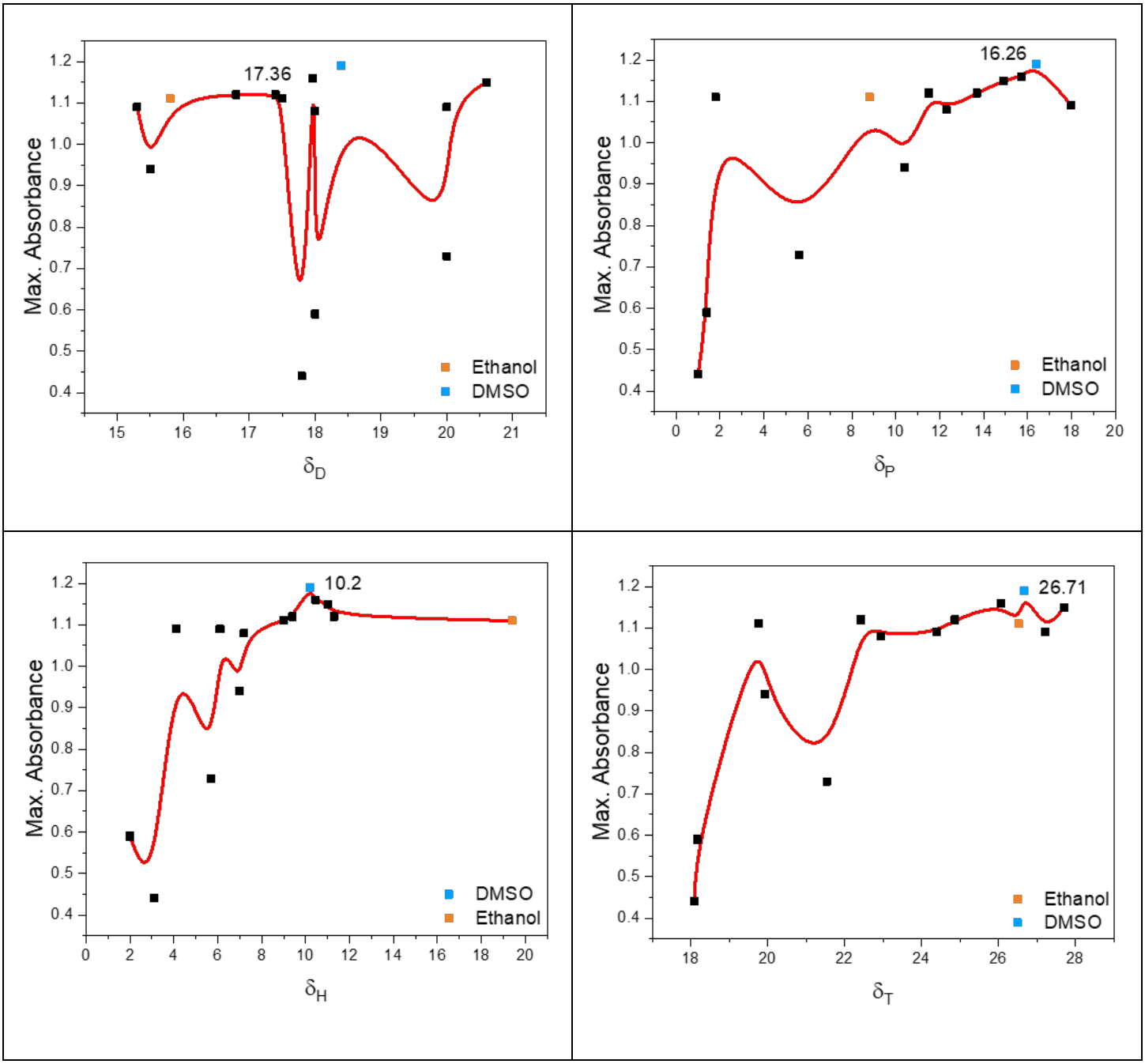

Figure 3-16 B-spline curve fit to determine δ_D (a), δ_P (b), δ_H (c) and δ_T(d) of PPAHQ Toluene

3.3.3.1. FT-IR investigations

The FT-IR spectra were used to identify the various functional groups of the synthesized polymers. Figure 3-17 represents spectra of PPAHQ with three solvents and starting materials.

The FT-IR spectrum of PPAHQ Toluene was characterized by a broad peak between 3500 and 2500 cm^{-1}, attributed to phenolic (OH) and ammonium (NH_3Cl) units (from unreacted amino groups on the small and sterically hindered linker). However, the spectra of PPAHQ DMSO and PPAHQ Ethanol lacked any of the signals for the phenolic (OH) or ammonium (NH_3Cl) groups of the DAHQ, indicating complete reaction. Peaks at 710, 1004 and 1070 cm^{-1}, assigned to vibration frequencies originating from C-Br bonds, are reduced in the spectra of the two latter polymers. Peaks at 1427 cm^{-1} for PPAHQ Ethanol and 1439 cm^{-1} for PPAHQ DMSO are related to the stretching vibrations of benzenoid rings. Table 3-9 represents key peak affiliations of PPAHQ materials.

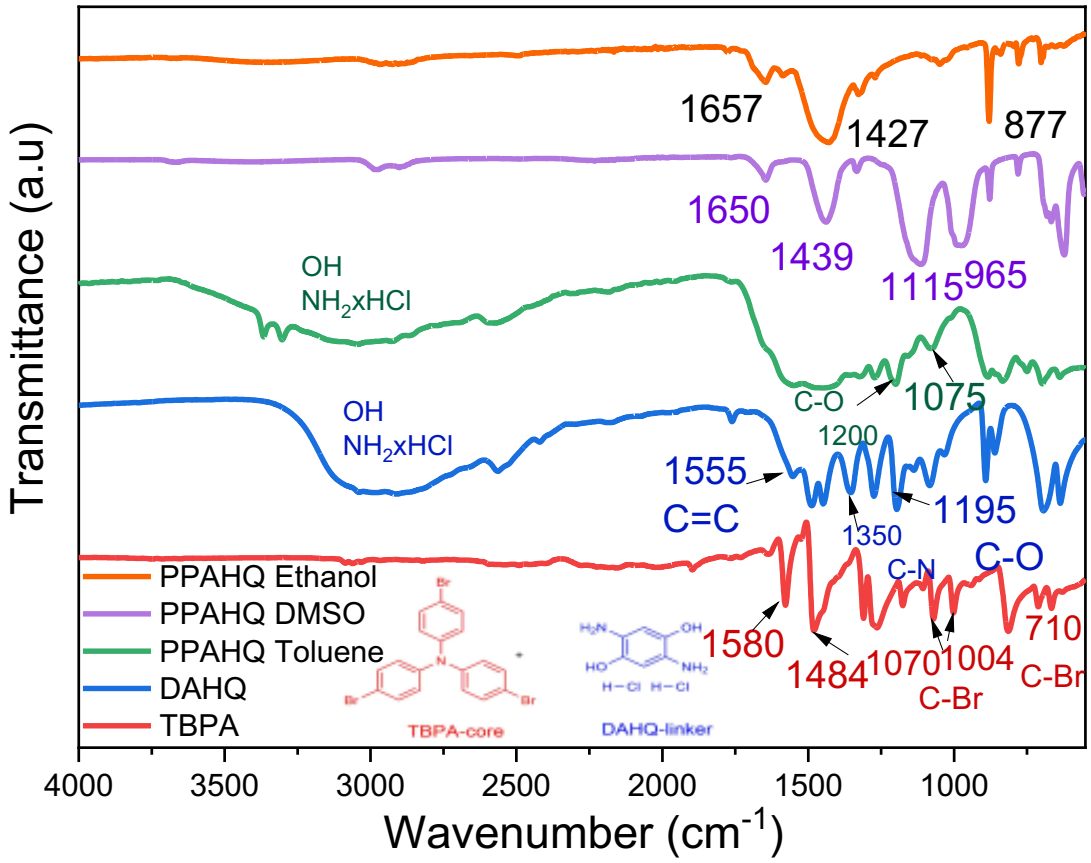

Figure 3-17 FTIR spectrum of PPAHQ

Table 3-9 FTIR Peak assignments

Peak (cm^{-1})	**Assignment**
3500-2500	OH, NH_2xHCl
1658	C=O stretching bond
1580	Quinoid ring
1497	Benzenoid ring
1096, 738	C-Br bonds vibration frequencies

3.3.3.2. XRD investigations

The powder XRD spectra from PPAHQ with three different solvents (toluene, DMSO and ethanol) is shown in Figure 3-18. The broad peak at around 2θ=15°, typical for repeating structure along the backbone (found in PPAHQ toluene and PPAHQ DMSO), and a broad peak centered around 2θ=25°, assigned to π–π stacking. All three polymers have strong intensity sharp peak at around 32° in 2θ. The same peak at 32° is found for the starting material TBPA. Peak at 46° appeared in PPAHQ toluene and ethanol spectra, the most probably residual material from DAHQ.

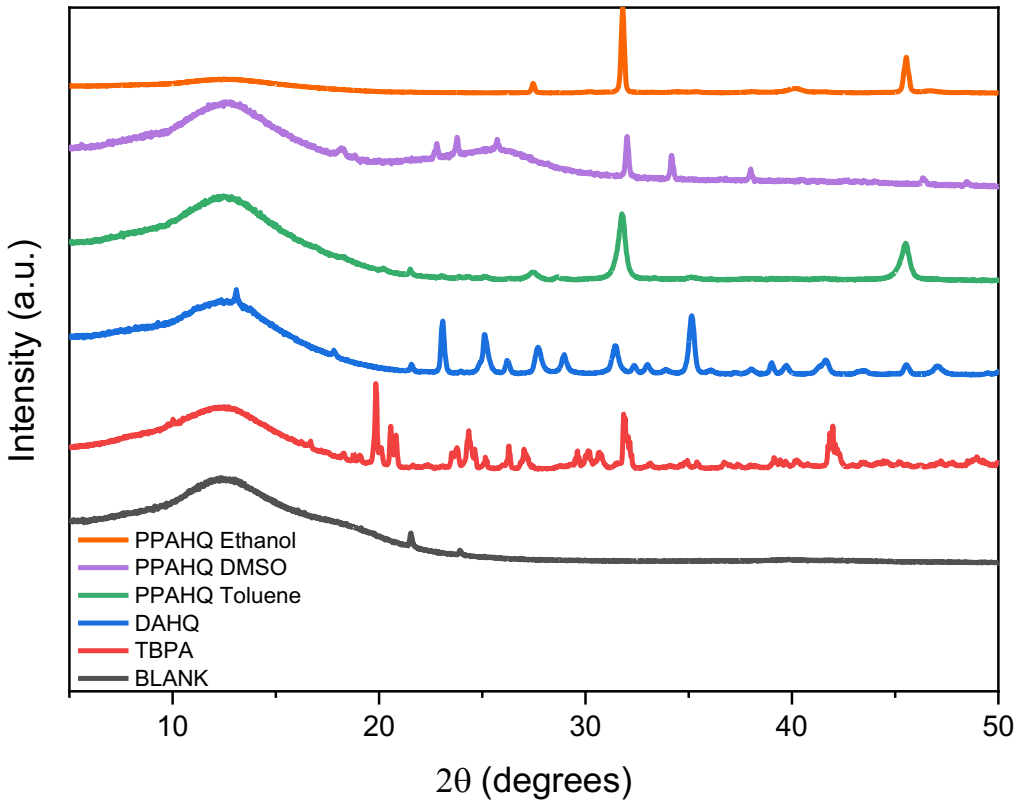

Figure 3-18 XRD spectra of PPAHQ

3.3.3.3. UV-Vis/NIR investigations

The solid-state UV-VIS/NIR spectra of conjugated PPAHQ presented one peak only, as can be seen in Figure 3-19. The maximum wavelength of PPAHQ Toluene is the highest at 669 nm, PPAHQ DMSO has a broad peak at around 513 nm, and finally, PPAHQ Ethanol has a peak at 407 nm. These peaks testify presence of π-π* transition of benzenoid and quinoid rings. These results confirm the creation of conjugated networks using the Buchwald-Hartwig coupling reaction. A number of interesting features need to be considered: 1) the significant shift in the peak maximum, potentially indicating different levels of conjugation in the materials (from the least conjugation in ethanol, to the highest in toluene; and 2) the significant difference in the width of the absorbance peak, and the very narrow peak for the materials prepared in toluene.

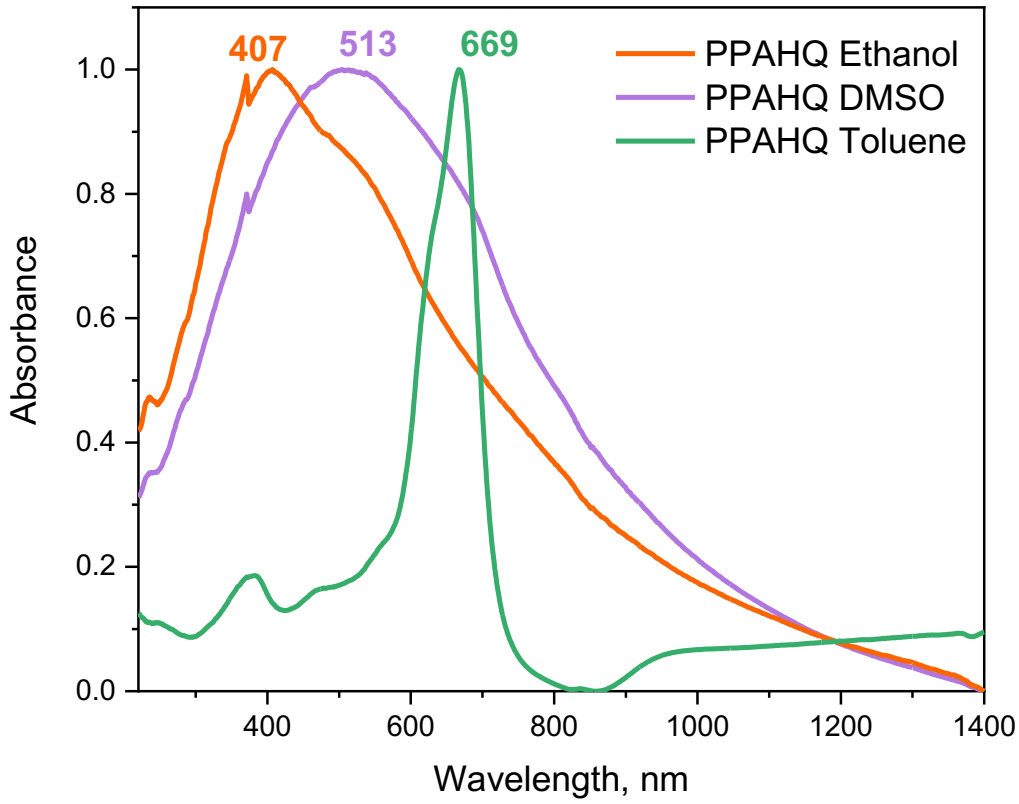

Figure 3-19 Solid state UV-Vis/NIR spectra of PPAHQ with different solvent

3.3.3.4. Surface area characterization

Figure 3-20(a) represent the N_2 adsorption/desorption isotherms of PPAHQ in three solvents. According to IUPAC classification, the PPAHQ Toluene and PPAHQ Ethanol sorption isotherms correspond to Type III isotherms, which are obtained when the amount of gas adsorbed increases without limit as its relative saturation approaches unity. PPAHQ DMSO sorption isotherms belongs to Type II. This type of isotherm indicates an indefinite multi-layer formation after completion of the monolayer and is found in adsorbents with a wide distribution of pore sizes.

All three these polymers contain mesoporous and microporous structures. The PPAHQ DMSO has a higher ratio of micropores then PPAHQ Toluene and Ethanol. The BET surface area for PPAHQ Toluene and PPAHQ Ethanol was 35 m^2/g and 28 m^2/g, respectively. However, in the case where DMSO was used as a solvent, the surface area increased significantly to 179 m^2/g Table 3-10.

The reason for these significant changes in properties (especially the surface area differences) can tentatively be attributed to not only matching of the overall HSP of the polymer and the solvent, but particularly also the different components (as reflected in the significant difference in surface area between DMSO and ethanol, despite having very small HSP differences). These results should be explored further in future studies.

Table 3-10 BET surface area of PPAHQ

Sample	S BET, m^2/g	Total pore volume DFT cm^3/g
PPAHQ Toluene	35	0.01
PPAHQ DMSO	179	0.07
PPAHQ Ethanol	28	0.008

A

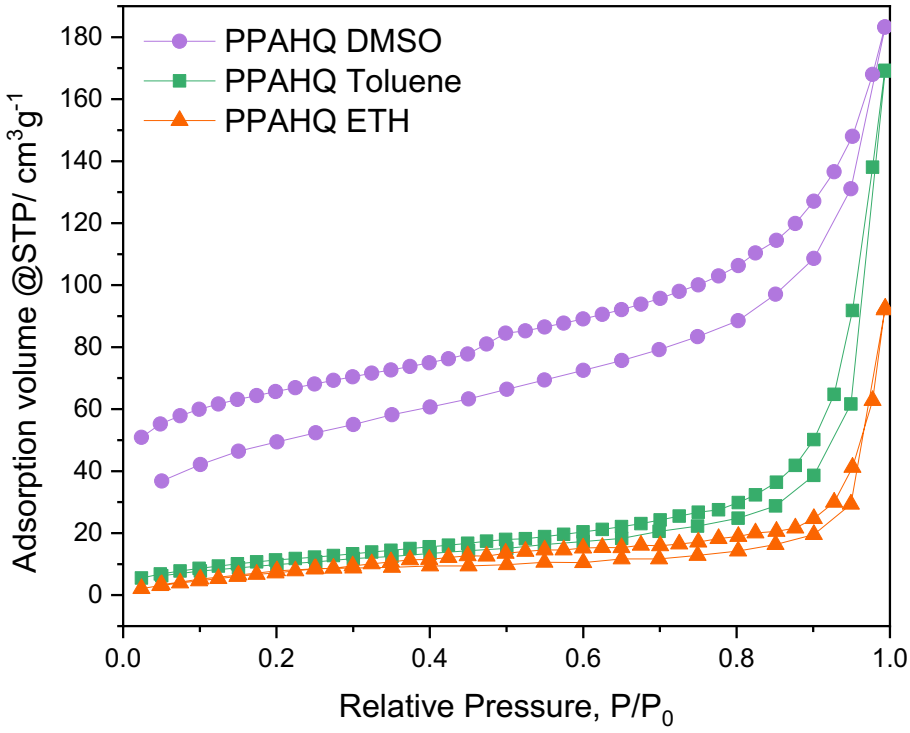
PPAHQ DMSO
PPAHQ Toluene
PPAHQ ETH
Adsorption volume @STP/ cm3g-1
Relative Pressure, P/P0
0
20
40
60
80
100
120
140
160
180
0.0
0.2
0.4
0.6
0.8
1.0

B

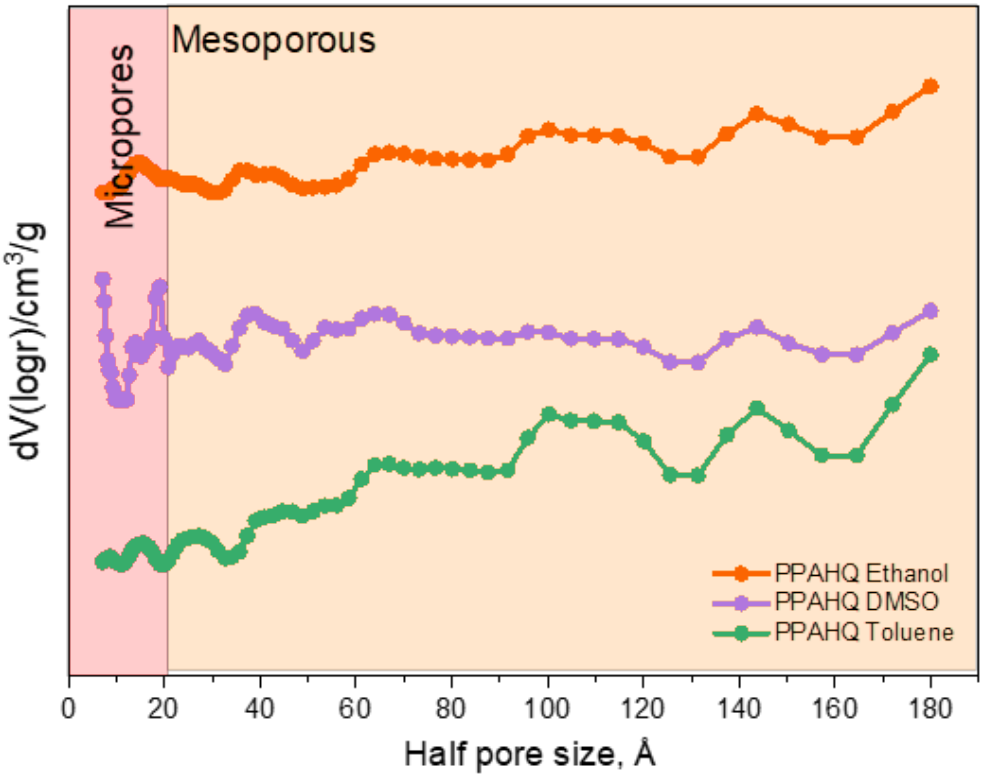
Micropores
Mesoporous
dV(logr)/cm3/g
PPAHQ Ethanol
PPAHQ DMSO
PPAHQ Toluene
0
20
40
60
80
100
120
140
160
180
Half pore size, Å

Figure 3-20 (A) Isotherms and (B) pore size distribution of PPAHQ with different solvent

3.3.4. PolyBenzeneHydroQuinone (PBHQ)

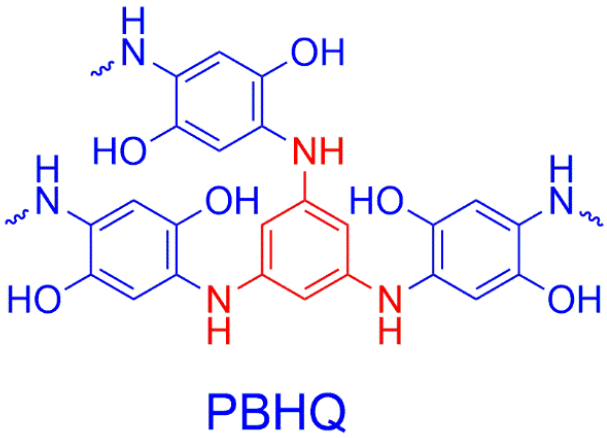

PBHQ

Scheme 3-4 PBHQ with TBB-core and DAHQ linker

PBHQ was produced when using TBB as a core and DAHQ as a linker Scheme 3-4. The main information concerning the synthesis of PBHQ is presented in Part 2.4.4. We use PBHQ Toluene as control for further research into determining HSPs for this polymer. HSPs provide a useful framework to understand, predict and improve the solubility, the compatibility, the stability and interaction between the solvent and the solute. Part 2.3 described the details of analysis of HSPs.

According to Table 3-11, It is clearly seen that the lowest value of $|\Delta\delta_T|$ is 0.06 and belongs to DMSO, which meant that DMSO should be compatible with PBAQ. Figure 3-21 confirmed good alignment of DMSO and the formed polymeric product. We chose ethanol as a second solvent to compare with DMSO (and toluene), with a $|\Delta\delta_T|$ value 0.21. They are both appropriate, but ethanol has lower polarity, i.e., the δ_P value of 8.8 is lower than that of DMSO (16.4), whereas the δ_H value of ethanol is higher (19.4) than that for DMSO (10.2).

Table 3-11 HSPs of solvents and polymer PBHQ

Sl No.	Solvents	δ_D[a]	δ_P[b]	δ_H[c]	δ_T[d]	$\lvert\Delta\delta_T\rvert$
1	Quinoline	20	5.6	5.7	21.53	5.2
2	NMP	18	12.3	7.2	22.95	3.78
3	***DMSO***	***18.4***	***16.4***	***10.2***	***26.67***	***0.06***
4	Propylene carbonate	20	18	4.1	27.22	0.49
5	Dioxane	17.5	1.8	9	19.76	6.97
6	DMF	17.4	13.7	11.3	24.86	1.87
7	1-methylimidazole	20.6	14.9	11	27.7	0.97
8	Acetonitrile	15.3	18	6.1	24.39	2.34
9	Xylene	17.8	1	3.1	18.09	8.64
10	***Ethanol***	***15.8***	***8.8***	***19.4***	***26.52***	***0.21***
11	Toluene	18	1.4	2	18.16	8.57
12	Dimethylacetamide	16.8	11.5	9.4	22.42	4.31
13	Acetone	15.5	10.4	7	19.93	6.8
14	m-cresol	17.96	15.73	10.46	26.06	0.67
15	***PBHQ***	***17.43***	***16.36***	***10.2***	***26.73***	

[a] δ_D = dipolar interaction parameter. [b] δ_P = the permanent dipole interaction parameter. [c] δ_H = the hydrogen-bonding interaction parameter, [d] δ_T = the total Hansen solubility parameter.

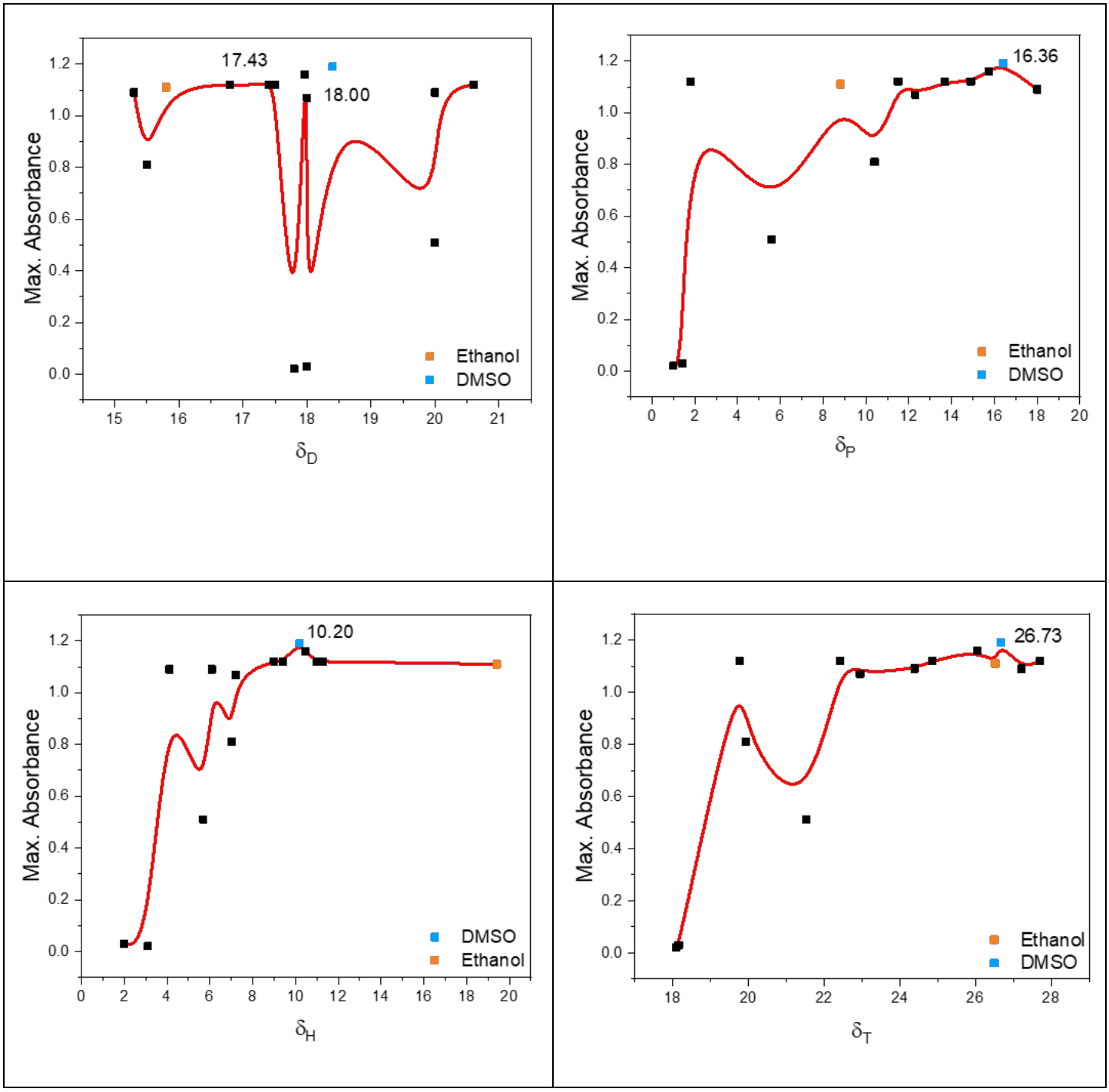

Figure 3-21 B-spline curve of δ_D (a), δ_P (b), δ_H (c) and δ_T(d) of PBHQ Toluene

3.3.4.1. FT-IR investigations

Functional groups and structure of polymers were investigated by FT-IR spectroscopy. Figure 3-22 shows the FT-IR spectra of products and source material of the synthesis. The broad peak at 3000 cm^{-1} attributed to phenolic (OH) and ammonium (NH_3Cl) bands. The TBB peaks at 738 and 1096 cm^{-1}, assigned to the vibration frequencies originating from C-Br bonds, are reduced in the spectra of PBHQ Toluene, PBHQ DMSO and PBHQ Ethanol. Peaks at 1427 cm^{-1} of PBHQ Ethanol and 1435 cm^{-1} of PBHQ DMSO are related to the stretching vibrations of benzenoid rings. In addition, both PBHQ Ethanol and PBHQ DMSO have a peak at 1585 cm^{-1}, which is attributed C-C stretching of the quinoid ring. Table 3-12 shows the position and assignments of these peaks.

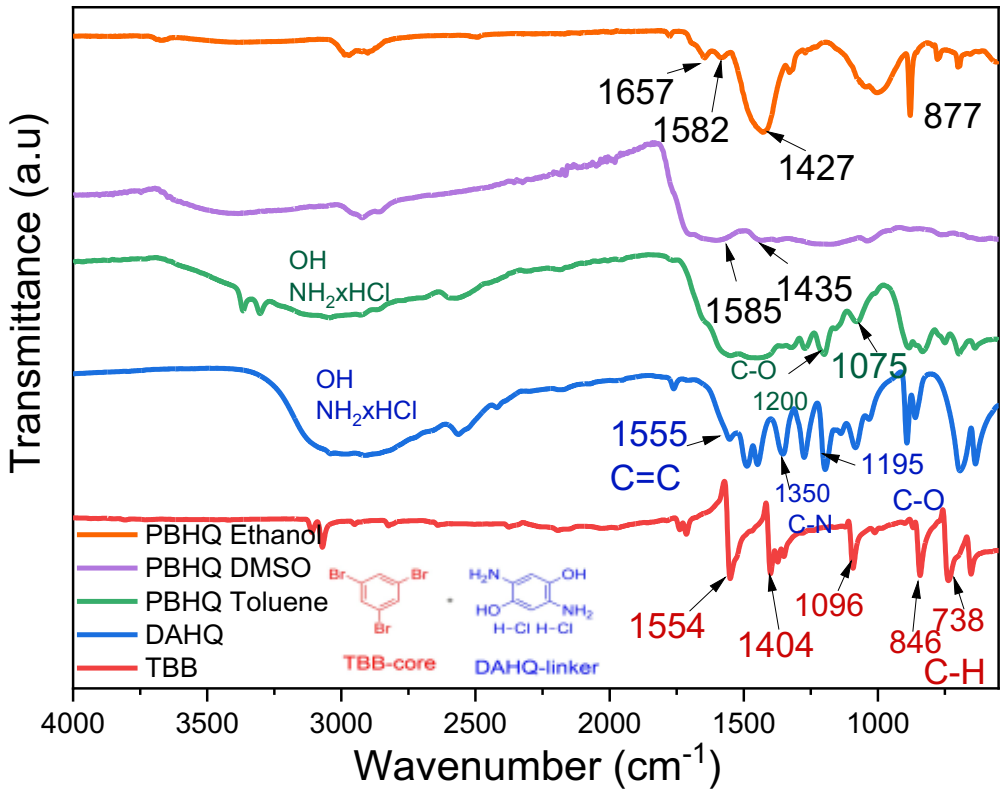

Figure 3-22 FTIR spectrum of PBHQ

Table 3-12 peaks affiliation

Peak	**Assignment**
3500-2500	OH, NH_2xHCl
1658	C=O stretching bond
1580	C-C stretching of the quinoid ring
1497	C-C stretching of the benzenoid ring
1096, 738	C-Br bonds vibration frequencies

3.3.4.2. XRD investigations

Another method of determine the chemical composition and structure of porous organic polymers is powder XRD The results are shown in Figure 3-23. PBHQ Ethanol and PBHQ Toluene both have a similar peak at about 30° and 45°. The starting material DAHQ exhibits the same peaks but with the lower intensity. PBHQ DMSO has a broad peak at 14° assigned to in-polymer chain scattering. PXRD confirm that polymer PBHQ DMSO is an amorphous material, showing a very broad feature that could be attributed to π-π stacking (centered at 25°).

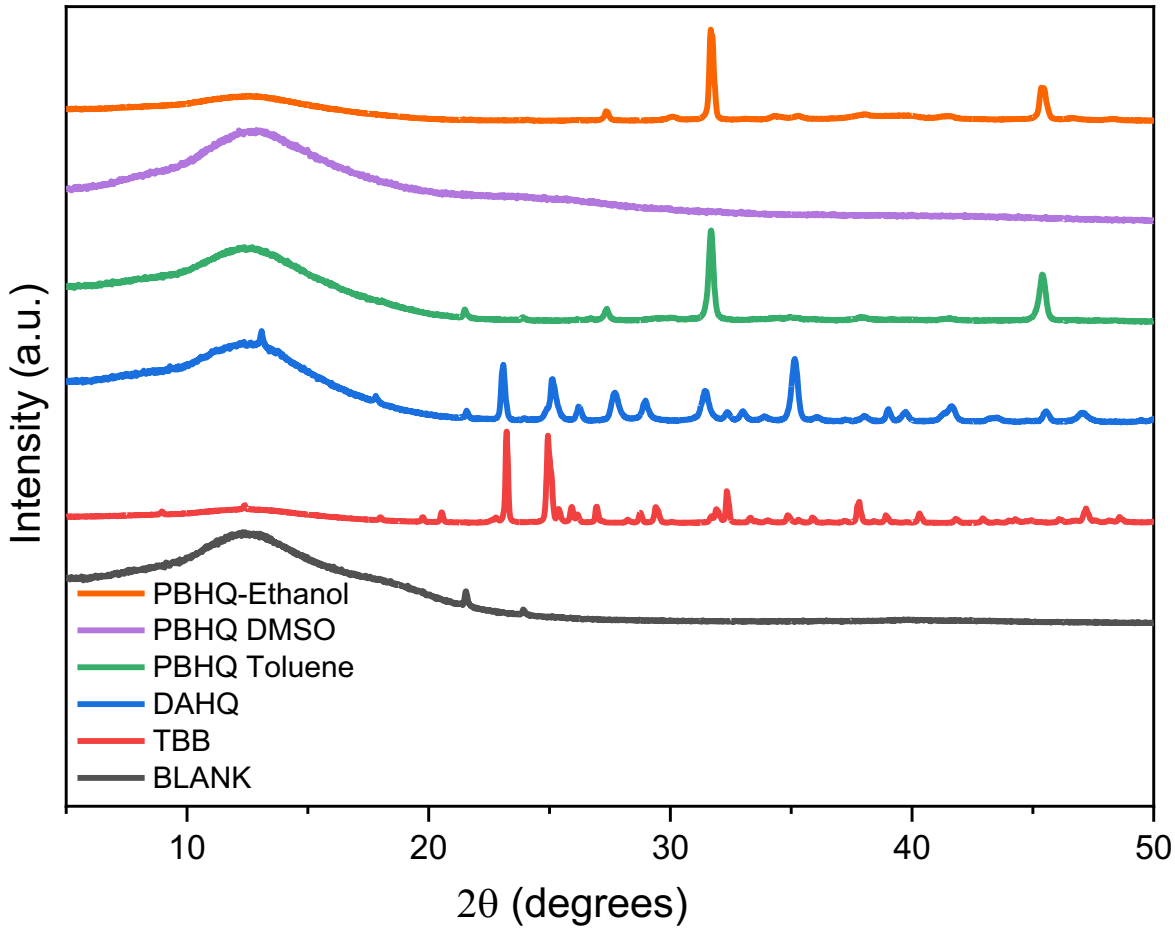

Figure 3-23 XRD spectra of starting and resulting PBHQ materials from different solvents.

3.3.4.3. UV-Vis/NIR Investigations

Solid-state UV-VIS/NIR spectra was used to analyze absorption of conjugated pi-electron systems. Figure 3-24 represents spectra of three polymers: PBHQ DMSO, PBHQ Ethanol and PBHQ Toluene. The maximum wavelength PBHQ Toluene is 667 nm and the peak narrow in comparison with other conjugated polymers (but similar to the previous case of the **PPAHQ** system, also in toluene). PBHQ Ethanol has a wider peak than PBHQ toluene and maximum wavelength equal to 617 nm. PBHQ DMSO has maximum wavelength at around 580 nm and broad peak that confirm presence of conjugated system.

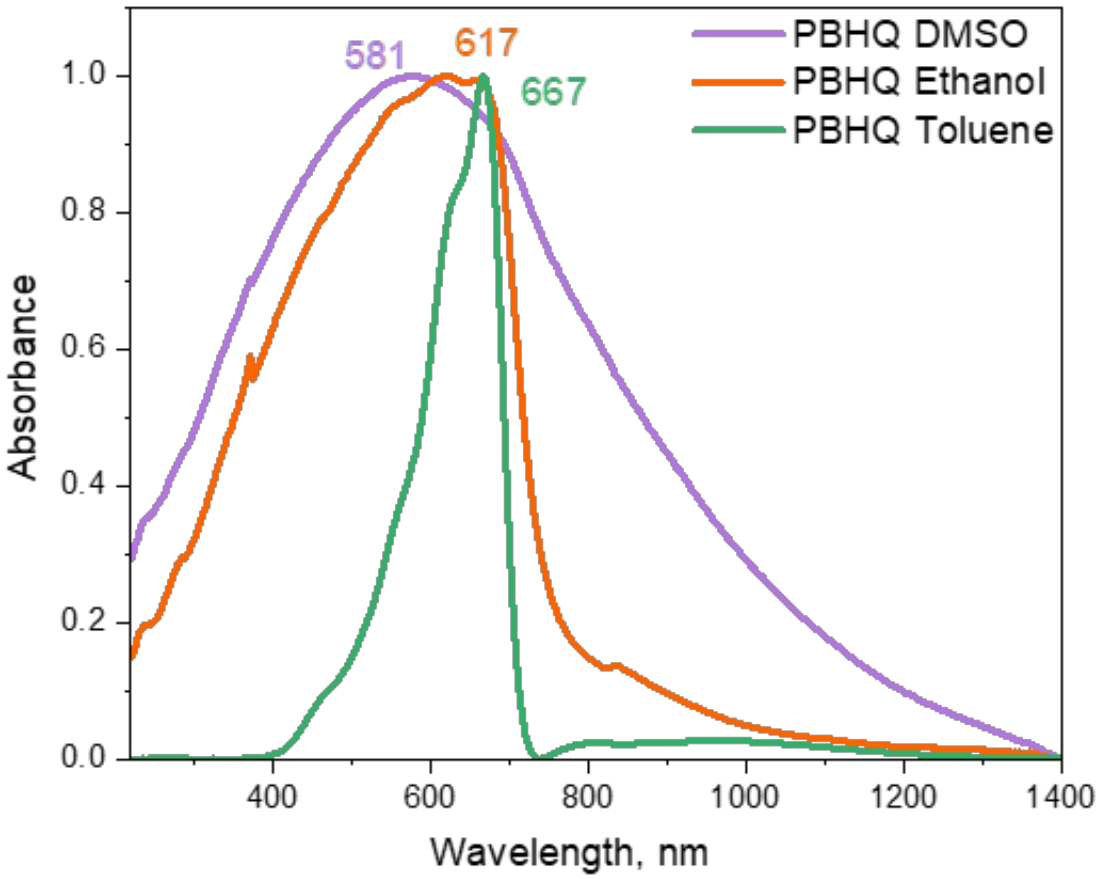

Figure 3-24 Solid state UV-Vis/NIR spectra of PBHQ with different solvent

3.3.4.4. Surface area characterization

The BET surface area significantly increased from 24 m^2/g (PBHQ Toluene) to 201 m^2/g (PBHQ DMSO) owing to HSP optimization. However, surface area did not change in any significant way for PBHQ Ethanol, with a surface area of 27 m^2/g (see Table 3-13).

According to the IUPAC classification both CMP PBHQ Toluene and PBHQ Ethanol show a Type III N_2 sorption isotherm whereas PBHQ DMSO show Type II isotherm Figure 3-25. The isotherms exhibited a continuous linear increase in adsorption, which occurs owing to the PSD mostly showing mesopores. Because of adsorbed gas interacting with the macrostructure and unfilled voids, a dramatic increase is observed after 0.9 relative pressure for PBHQ Toluene and PBHQ Ethanol, but in the case of PBHQ DMSO growth is gradual.

The pore size distribution clearly shows the presence of micropores in the PBHQ DMSO polymer system. In both the other polymers mesopores dominate the distribution.

Table 3-13 BET surface area of PBHQ

Sample	S BET, m^2/g	Total pore volume DFT cm^3/g
PBHQ Toluene	24	0.007
PBHQ DMSO	201	0.07
PBHQ Ethanol	27	0.008

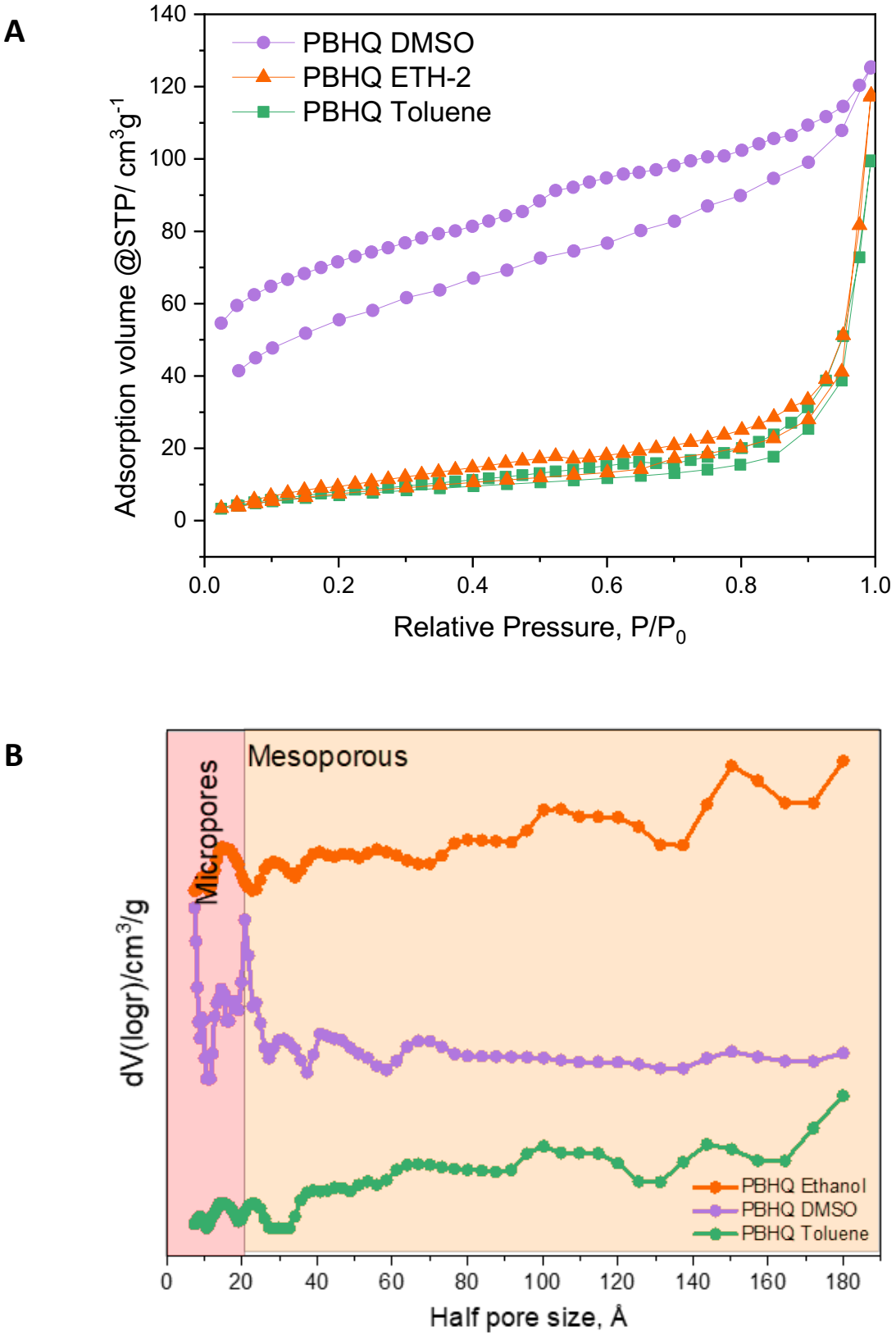

Figure 3-25 (A) Isotherms and (B) pore size distribution of PBHQ with different solvent

3.3.4.5. CO_2 Reduction studies

Cyclic voltametery (CV) is a method to study a material's electrochemical behaviour and gain information about their oxidation and reduction potentials. To investigate the electrochemical and redox properties of the synthesised materials in the presence of CO_2, CV measurements were obtained on a glassy carbon working electrode and was cycled repeatedly between −1.75 V and 0.25 V vs V_{SCE}, then converted to reversible hydrogen electrode (RHE) dependent on the effect of the pH, with the equation given in Section 3. The process of CO_2 electrochemical reduction was carried out with 0.1 M $KHCO_3$ as electrolyte with two different pH values (pH of CO_2 saturated electrolyte: 7.21, pH of argon-saturated electrolyte: 9.23) in a two-compartment H-cell with three-electrodes. The electrodes used are a glassy carbon as the working electrode on which a prepared CMP sample is drop cast (prepared as seen in Figure 8), a calomel electrode as reference electrode, and Pt wire as counter electrode.

The voltammograms present in Figure 3-26 are from the CV measurements under CO_2 and argon atmospheres, respectively. The current density (y-axis) in the CO2-saturated electrolyte investigation (Fig 3-26 A) is lower than the Ar-saturated system (Fig 3-26 B) at higher negative potential (i.e., at −1 V vs RHE). The increased current density for the Ar-saturated sample is attributed to higher hydrogen evolution taking place, and confirms the catalytic activity of our materials.

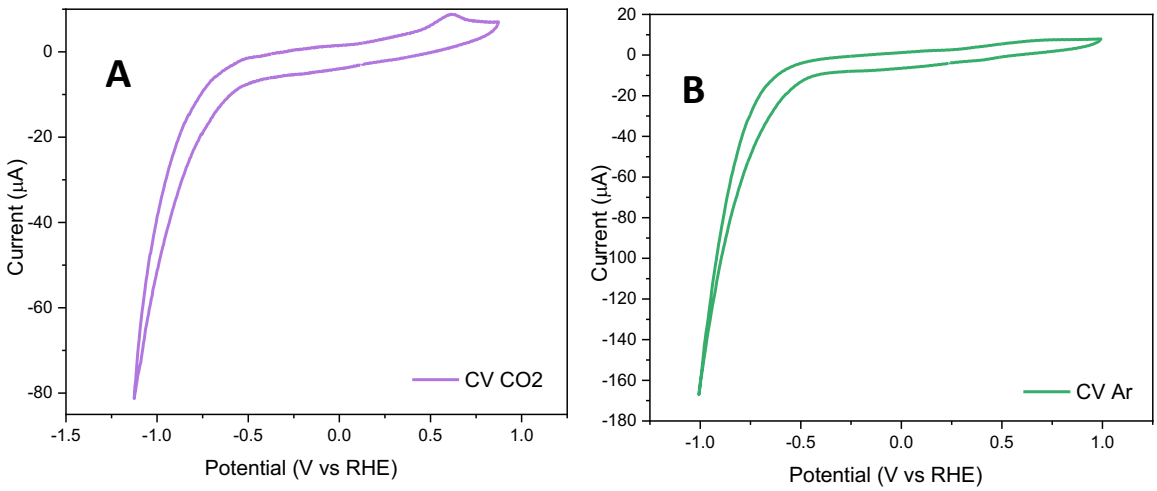

Figure 3-26 Cyclic voltammograms in (A) CO2 and (B) argon atmosphere of the PBAQ DMSO

3.3.4.6. Battery testing

The cycling stability of the batteries based on PBHQ DMSO and PPAHQ was studied by cycling the cells at various current densities (please see the experimental section for details of the cell assembly). For the battery based on the PBHQ DMSO, when the current density was increased from 50 to 100, 250, 500, and 1000 mA g^{-1}, the discharge capacity decreased slightly from approximately 89 to 58, 35, 29 and 20 mA h g^{-1}, respectively. When current density was decreased from 10000 to 50 mA g^{-1}, a discharge capacity of 90 mAh g^{-1} was determined, confirming the potential for long-term usage stability. The same cycling performance was observed for the cell with PPAHQ DMSO. The highest discharge capacity of PPAHQ was found at 89 mAh g^{-1} and the discharge capacity of PPAHQ was 115 mAh g^{-1}. See Figure 3-27 for details. These values compare favourably with related COF materials from the literature.[129]

Cyclic voltammetry (CV) curves (Figure 3-28) showed small redox peaks for PBHQ. The reduction peak for PBHQ DMSO at 2.2 V vs Li/Li^+, which is associated with an oxidation peak at 3.3 V vs Li/Li.

Although showing the promise of these materials, the recorded values and performance of the studied materials in this initial scoping study was lower than expected. Obvious areas of improvement are a) increasing the surface area, b) increasing the conductivity, and c) increasing the PSD to also include macropores to ensure easy diffusion of ions to and from the electrodes.

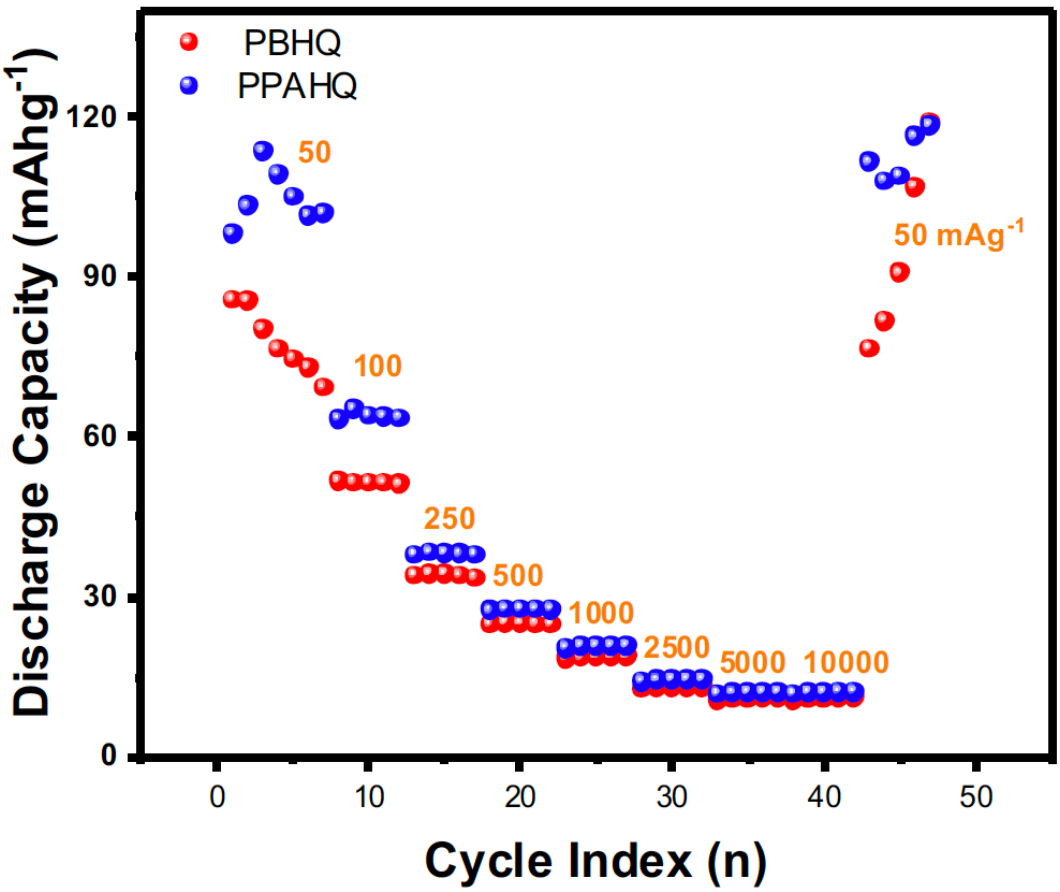

Figure 3-27 Electrochemical performance of discharge capacity of PBHQ and PPAHQ.

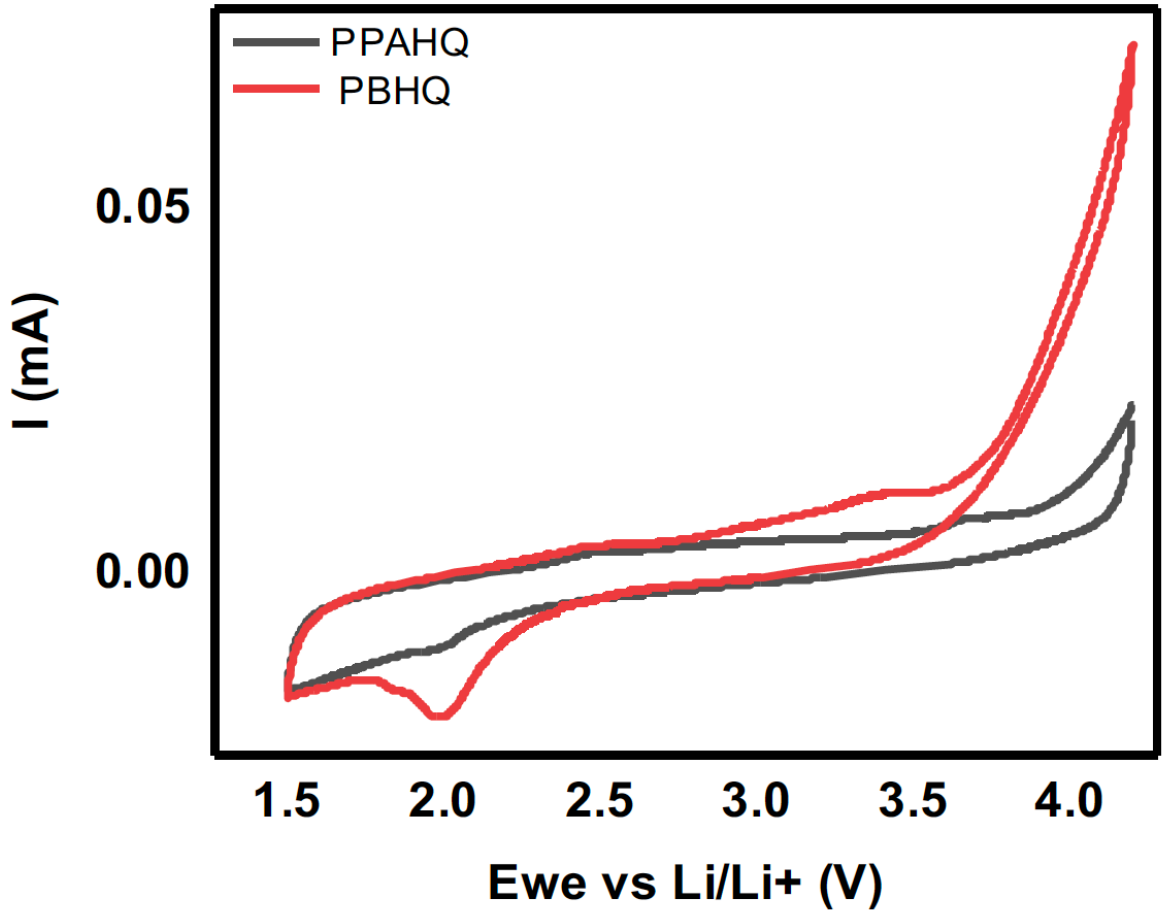

Figure 3-28 Cyclic voltammograms of PBHQ and PPAHQ

3.4. Summary

The unique functional and structural characteristics of CMP gives potential to use these materials in different ways for applications. In this work nitrogen rich CMPs were designed and synthesized via Buchwald-Hartwig (BH) cross-coupling reactions. In the first part, reaction conditions such as reagent ratios and solvents were optimized for higher reactivity and increased ion diffusion. Moreover, we investigated influence of salt on the porosity of polymers.

After optimizing reactions and conditions, HSPs were calculated to find theoretically the most compatible solvents. The most compatible solvents were found for four CMPs PPAAQ, PBAQ, PPAHQ and PBHQ. As a results, high yield and surface areas were achieved for these materials. DMSO was chosen as a compatible solvent for the synthesis of PBHQ.

Finally, electrochemical investigations of PBHQ DMSO were done in the National Center for Nanoscience and Technology in China. Coin cells were prepared as a standard way to test prototype materials for batteries, showing the promise of these materials for further exploration.

4. Conclusions and Future work

4.1. Design

4.1.1. Design and optimising new materials using chemistry

Previous investigations[130] from the Faul group investigated the amine-CMP family by using 1,3,5-tris(4-bromophenyl)amine (TBPA), tetrakis(4-bromidephenyl)-ethylene (TBPE), 1,3,5-tris(4-aminophenyl)benzene (TAPB), and 1,3,5-tris-(4-aminophenyl)triazine (TAPT) as building blocks. The approach to date has been to select and combine cores with multiple bromo groups (3 to 6) and various di-amine linkers. In their study, they expanded the synthetic approach and designed a range of new materials by use combinations of tri- and tetrabromo and tri-amine building blocks (Scheme 4-1), based on TPA and TPE. They synthesized four novel BH CMPs and exploited the universal adaptability of our BXJ method for the control and optimization of the surface area, pore size, and porosity. The results showed that LCMP1 and LPCMP3, synthesized by using TAPB as the building blocks, possess similar BET specific surface area values, which are much higher (more than double) than those of LPCMP2 and LPCMP4 that were synthesized with TAPT as the amino building block. Moreover, if compare two cores with determined linker in both cases where tetra functional group was used, the BET surface area was higher. It would be interesting to investigate material synthesized using TBPE and DAHQ. As it is possible to use simple salts to tune the Hansen solubility parameters (HSPs) of the solvents to match those of the growing polymer chains, the resulting CMPs will possess significantly higher surface areas and well-defined micropores. It is therefore proposed to use, in combination with carefully chosen building blocks, combinations of solvents for better tuning by using computational methods to calculate all three sub components of HSPs (as developed by Xue Fang in her PhD project).[131]

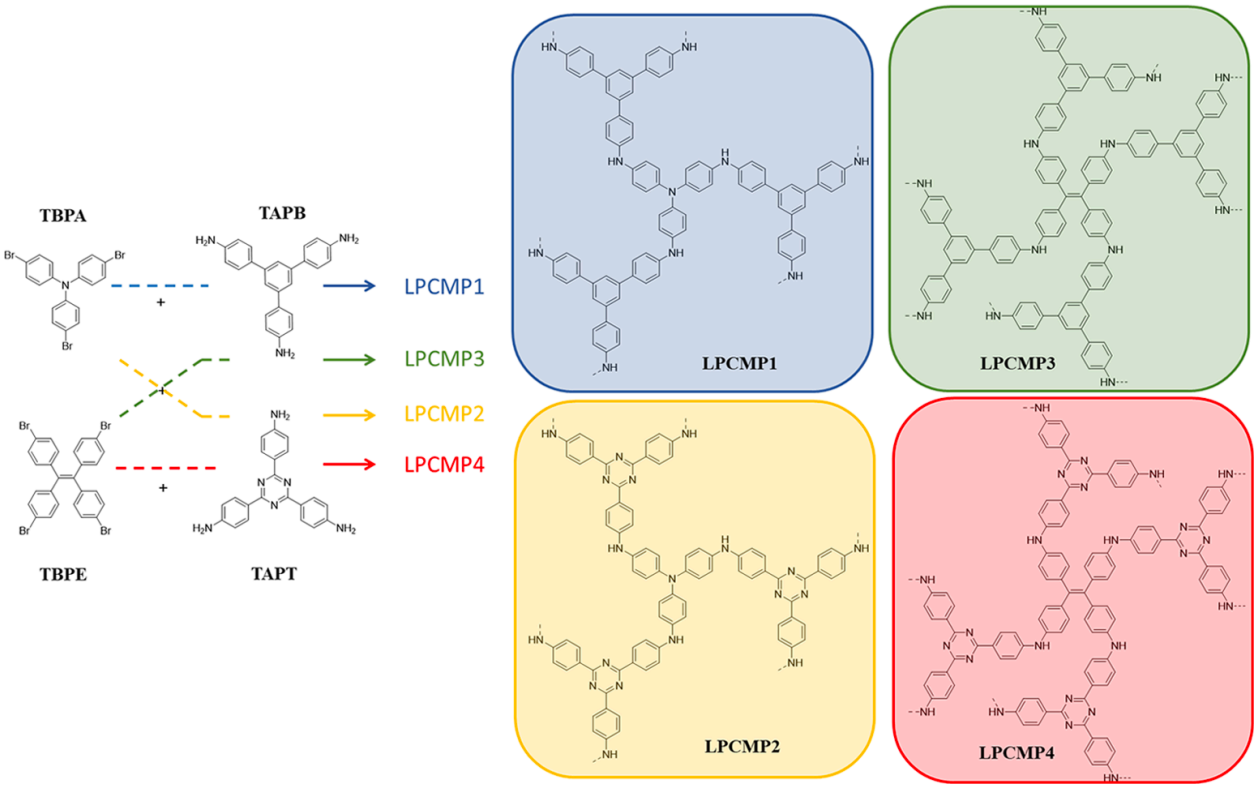

Scheme 4-1 Synthetic route showing structures synthesized with starting materials with higher connectivity.[130]

4.1.2. Computational chemistry methods

One of the modern methods to design material is computational chemistry methods. An exciting new development is the approach used by Dr Abbie Trewin in her so-called Artificial Synthesis of Conjugated Microporous Polymers.[132] Amorphous network materials are becoming progressively important with applications, for example, as supercapacitors, battery anodes, and proton conduction membranes. The design of CMPs materials is hampered by the amorphous nature of the structure and sensitivity to synthetic conditions. Trewin et al showed that through artificial synthesis, fully mimicking the catalytic formation cycle, and full synthetic conditions, it is possible to generate structural models that can fully describe the physical properties of these

amorphous network materials. This opens pathways for the rational design where complex structural influences, such as the solvent and catalyst choice, can be considered.

According to these new computational methods it is suggested to develop a methodology for generating structural models of amorphous conjugated microporous polymers through full imitation of the synthetic process, including variations of the solvent quality (through tuning the HSPs). It is envisaged that information about the structure and formation mechanism will be obtained, enabling design of novel CMP systems.

4.2. Application

4.2.1. New supercapacitor materials with high capacitance

Supercapacitors, fuel cells and batteries are the most common examples of energy storage systems. Supercapacitors, store energy using either ion adsorption (electrochemical double layer capacitors) or fast surface redox reactions (pseudo-capacitors). They can complement or replace batteries in electrical energy storage and harvesting applications when high power delivery or uptake is needed.

Here after redesigning our CMP materials, we can use them for supercapacitors. The porous structure of CMP is characterized by a broad distribution of pore size. Longer activation time or higher temperature leads to larger mean pore size. CMPs are built by covalent connection of rigid, π-conjugated building blocks with three or more functionalities, thus forming 3D macromolecular networks with micropores (i.e., <2 nm) and sometimes exceptionally high permanent surface areas. All these unique properties of CMPs make them good material for supercapacitors.

Thomas et al. synthesized CMP material poly-aminoanthraquinone (PAQ) with specific surface areas up to 600 m2 g-1 via BH cross coupling reaction.[133] PAQs consisting of anthraquinonylamine and triphenylamine showed to be promising materials for electrochemical energy storage owing to their hierarchical porosity and high redox activity.

They used these materials as electrodes for supercapacitors, which delivered specific capacitance values of 570 F g−1, retaining 80–85% capacitance after 6000 cycles with almost 100% columbic efficiencies. This research proves that use CMP with aminoanthraquinone as an electrode for supercapacitors is successful, and that the materials explored here can, with further optimization, find useful application.

4.2.2. CO2 capture and conversion

After completion of research into the development of energy storage devices it will be interesting to explore application of our CMP materials in other directions. One emerging area is the use of CMPs for both capture and conversion (under electrocatalytic conditions), leading to turning a waste product into a potentially valuable feedstock for the preparation of formate and methanol, for example. This application was briefly explored in the thesis (Section 1.2.3.1), but needs more work to fully explore the potential of these new materials.

5. Bibliography

1. Wuebbles, D. J. *et al.* Our Globally Changing Climate - Climate Science Special Report. *Clim. Sci. Spec. Rep. Fourth Natl. Clim. Assess.* **Volume 1**, 35–72 (2017).

2. Buis, A. A Degree of Concern: Why Global Temperatures Matter. *NASA's Global Climate Change Website* (2019).

3. U.S. Global Change Research Program. *Climate science special report: Fourth national climate assessment, volume I*. *U.S. Global Change Research Program* (2018) doi:10.7930/J0J964J6.

4. Friedlingstein, P. *et al.* Global Carbon Budget 2019. *Earth Syst. Sci. Data* **11**, 1783–1838 (2019).

5. Sixth, T. & Budget, C. fuel_supply_County.

6. BEIS. *Net Zero Strategy: Build Back Greener*. *Gov.Uk* (2021).

7. Ockwig, N. W., Co, A. P., Keeffe, M. O., Matzger, A. J. & Yaghi, O. M. Porous , Crystalline , Covalent Organic Frameworks. **310**, 1166–1171 (2005).

8. Das, S., Heasman, P., Ben, T. & Qiu, S. Porous Organic Materials: Strategic Design and Structure-Function Correlation. *Chemical Reviews* (2017) doi:10.1021/acs.chemrev.6b00439.

9. Liu, T. & Liu, G. Porous organic materials offer vast future opportunities. *Nature Communications* (2020) doi:10.1038/s41467-020-15911-8.

10. Thommes, M. *et al.* Physisorption of gases, with special reference to the

evaluation of surface area and pore size distribution (IUPAC Technical Report). *Pure Appl. Chem.* **87**, 1051–1069 (2015).

11. Xu, Y., Jin, S., Xu, H., Nagai, A. & Jiang, D. Conjugated microporous polymers: Design, synthesis and application. *Chem. Soc. Rev.* **42**, 8012–8031 (2013).

12. Tozawa, T. *et al.* Porous organic cages. *Nat. Mater.* **8**, 973–978 (2009).

13. Feng, X., Ding, X. & Jiang, D. Covalent organic frameworks. *Chem. Soc. Rev.* **41**, 6010–6022 (2012).

14. Budd, P. M. *et al.* Polymers of intrinsic microporosity (PIMs): robust, solution-processable, organic nanoporous materials. *Chem. Commun.* **4**, 230–231 (2004).

15. Lu, W. *et al.* Porous polymer networks: Synthesis, porosity, and applications in gas storage/separation. *Chem. Mater.* **22**, 5964–5972 (2010).

16. Jiang, J. X. *et al.* Conjugated microporous poly(aryleneethynylene) networks. *Angew. Chemie - Int. Ed.* **46**, 8574–8578 (2007).

17. Das, M. C., Xiang, S., Zhang, Z. & Chen, B. Functional mixed metal-organic frameworks with metalloligands. *Angew. Chemie - Int. Ed.* **50**, 10510–10520 (2011).

18. Zhao, Y. *et al.* Metal organic frameworks for energy storage and conversion. *Energy Storage Mater.* **2**, 35–62 (2016).

19. Baumann, A. E., Burns, D. A., Liu, B. & Thoi, V. S. Metal-organic framework functionalization and design strategies for advanced electrochemical energy storage devices. *Communications Chemistry* (2019) doi:10.1038/s42004-019-

0184-6.

20. Furukawa, H. & Yaghi, O. M. Storage of hydrogen, methane, and carbon dioxide in highly porous covalent organic frameworks for clean energy applications. *J. Am. Chem. Soc.* **131**, 8875–8883 (2009).

21. Morozan, A. & Jaouen, F. Metal organic frameworks for electrochemical applications. *Energy Environ. Sci.* **5**, 9269–9290 (2012).

22. Wang, L. *et al.* Metal-organic frameworks for energy storage: Batteries and supercapacitors. *Coord. Chem. Rev.* **307**, 361–381 (2016).

23. Ding, M., Flaig, R. W., Jiang, H. L. & Yaghi, O. M. Carbon capture and conversion using metal-organic frameworks and MOF-based materials. *Chemical Society Reviews* (2019) doi:10.1039/c8cs00829a.

24. Guan, B. Y., Yu, X. Y., Wu, H. Bin & Lou, X. W. D. Complex Nanostructures from Materials based on Metal–Organic Frameworks for Electrochemical Energy Storage and Conversion. *Advanced Materials* (2017) doi:10.1002/adma.201703614.

25. Chen, Y. Z., Zhang, R., Jiao, L. & Jiang, H. L. Metal–organic framework-derived porous materials for catalysis. *Coordination Chemistry Reviews* (2018) doi:10.1016/j.ccr.2018.02.008.

26. Xue, D. X., Wang, Q. & Bai, J. Amide-functionalized metal–organic frameworks: Syntheses, structures and improved gas storage and separation properties. *Coordination Chemistry Reviews* (2019) doi:10.1016/j.ccr.2017.10.026.

27. Das, S., Heasman, P., Ben, T. & Qiu, S. Porous Organic Materials: Strategic Design and Structure-Function Correlation. *Chem. Rev.* **117**, 1515–1563 (2017).

28. Xu, S. Q., Zhan, T. G., Wen, Q., Pang, Z. F. & Zhao, X. Diversity of Covalent Organic Frameworks (COFs): A 2D COF Containing Two Kinds of Triangular Micropores of Different Sizes. *ACS Macro Lett.* **5**, 99–102 (2016).

29. Huang, N., Wang, P. & Jiang, D. Covalent organic frameworks: A materials platform for structural and functional designs. *Nature Reviews Materials* (2016) doi:10.1038/natrevmats.2016.68.

30. Xiong, C. *et al.* Towards covalent organic frameworks with predesignable and aligned open docking sites. *Chem. Commun.* (2014) doi:10.1039/c4cc01825g.

31. El-Mahdy, A. F. M. *et al.* A Hollow Microtubular Triazine- and Benzobisoxazole-Based Covalent Organic Framework Presenting Sponge-Like Shells That Functions as a High-Performance Supercapacitor. *Chem. - An Asian J.* **14**, 1429–1435 (2019).

32. Guan, X., Chen, F., Fang, Q. & Qiu, S. Design and applications of three dimensional covalent organic frameworks. *Chemical Society Reviews* (2020) doi:10.1039/c9cs00911f.

33. Geng, K. *et al.* Covalent Organic Frameworks: Design, Synthesis, and Functions. *Chemical Reviews* (2020) doi:10.1021/acs.chemrev.9b00550.

34. Colson, J. W. *et al.* on Single-Layer Graphene. 228–232 (2011).

35. Wan, S., Guo, J., Kim, J., Ihee, H. & Jiang, D. A photoconductive covalent

organic framework: Self-condensed arene cubes composed of eclipsed 2D polypyrene sheets for photocurrent generation. *Angew. Chemie - Int. Ed.* **48**, 5439–5442 (2009).

36. Hani M. El-Kaderi1, Joseph R. Hunt1, José L. Mendoza-Cortés1, Adrien P. Côté1, Robert E. Taylor1, Michael O'Keeffe2, O. M. Y. Designed Synthesis of 3D Covalent. *Science (80-.).* **13**, 268–273 (2007).

37. Ding, S. Y. *et al.* Construction of covalent organic framework for catalysis: Pd/COF-LZU1 in Suzuki-Miyaura coupling reaction. *J. Am. Chem. Soc.* **133**, 19816–19822 (2011).

38. Abuzeid, H. R., EL-Mahdy, A. F. M. & Kuo, S. W. Covalent organic frameworks: Design principles, synthetic strategies, and diverse applications. *Giant* **6**, 100054 (2021).

39. Low, Z. X., Budd, P. M., McKeown, N. B. & Patterson, D. A. Gas Permeation Properties, Physical Aging, and Its Mitigation in High Free Volume Glassy Polymers. *Chemical Reviews* (2018) doi:10.1021/acs.chemrev.7b00629.

40. Carta, M., Msayib, K. J. & McKeown, N. B. Novel polymers of intrinsic microporosity (PIMs) derived from 1,1-spiro-bis(1,2,3,4-tetrahydronaphthalene)-based monomers. *Tetrahedron Lett.* **50**, 5954–5957 (2009).

41. McKeown, N. B. & Budd, P. M. Exploitation of intrinsic microporosity in polymer-based materials. *Macromolecules* **43**, 5163–5176 (2010).

42. McKeown, N. B. *et al.* Towards polymer-based hydrogen storage materials: Engineering ultramicroporous cavities within polymers of intrinsic

microporosity. *Angew. Chemie - Int. Ed.* **45**, 1804–1807 (2006).

43. Doris, S. E., Ward, A. L., Frischmann, P. D., Li, L. & Helms, B. A. Understanding and controlling the chemical evolution and polysulfide-blocking ability of lithium-sulfur battery membranes cast from polymers of intrinsic microporosity. *J. Mater. Chem. A* (2016) doi:10.1039/c6ta06401a.

44. Yang, Q. *et al.* PIM-1 as an artificial solid electrolyte interphase for stable lithium metal anode in high-performance batteries. *J. Energy Chem.* (2020) doi:10.1016/j.jechem.2019.06.012.

45. Baran, M. J. *et al.* Design Rules for Membranes from Polymers of Intrinsic Microporosity for Crossover-free Aqueous Electrochemical Devices. *Joule* (2019) doi:10.1016/j.joule.2019.08.025.

46. Chae, I. S. *et al.* Ultra-High Proton/Vanadium Selectivity for Hydrophobic Polymer Membranes with Intrinsic Nanopores for Redox Flow Battery. *Adv. Energy Mater.* (2016) doi:10.1002/aenm.201600517.

47. Bernardo, P. *et al.* Thin film composite membranes based on a polymer of intrinsic microporosity derived from TrÖger's base: A combined experimental and computational investigation of the role of residual casting solvent. *J. Memb. Sci.* (2019) doi:10.1016/j.memsci.2018.10.001.

48. Lau, C. H. *et al.* Tailoring molecular interactions between microporous polymers in high performance mixed matrix membranes for gas separations. *Nanoscale* (2020) doi:10.1039/d0nr04801a.

49. Song, Q. *et al.* Photo-oxidative enhancement of polymeric molecular sieve membranes. *Nat. Commun.* (2013) doi:10.1038/ncomms2942.

50. Lee, J. S. M. & Cooper, A. I. Advances in Conjugated Microporous Polymers. *Chem. Rev.* **120**, 2171–2214 (2020).

51. Zhang, C. *et al.* Bifunctionalized conjugated microporous polymers for carbon dioxide capture. *Polymer (Guildf).* **61**, 36–41 (2015).

52. Huang, Q. *et al.* Layered Thiazolo[5,4- d] Thiazole-Linked Conjugated Microporous Polymers with Heteroatom Adoption for Efficient Photocatalysis Application. *ACS Appl. Mater. Interfaces* **11**, 15861–15868 (2019).

53. Chen, L., Honsho, Y., Seki, S. & Jiang, D. Light-harvesting conjugated microporous polymers: Rapid and highly efficient flow of light energy with a porous polyphenylene framework as antenna. *J. Am. Chem. Soc.* **132**, 6742–6748 (2010).

54. Chen, L., Yang, Y. & Jiang, D. CMPs as scaffolds for constructing porous catalytic frameworks: A built-in heterogeneous catalyst with high activity and selectivity based on nanoporous metalloporphyrin polymers. *J. Am. Chem. Soc.* **132**, 9138–9143 (2010).

55. Khaligh, A. & Li, Z. Battery, ultracapacitor, fuel cell, and hybrid energy storage systems for electric, hybrid electric, fuel cell, and plug-in hybrid electric vehicles: State of the art. *IEEE Trans. Veh. Technol.* **59**, 2806–2814 (2010).

56. Chang, L., Stacchiola, D. J. & Hu, Y. H. An Ideal Electrode Material, 3D Surface-Microporous Graphene for Supercapacitors with Ultrahigh Areal Capacitance. *ACS Appl. Mater. Interfaces* **9**, 24655–24661 (2017).

57. Liu, X., Xu, Y. & Jiang, D. Conjugated microporous polymers as molecular sensing devices: Microporous architecture enables rapid response and

enhances sensitivity in fluorescence-on and fluorescence-off sensing. *J. Am. Chem. Soc.* **134**, 8738–8741 (2012).

58. Herde, Z. D., Dharmasena, R., Sumanasekera, G., Tumuluru, J. S. & Satyavolu, J. Impact of hydrolysis on surface area and energy storage applications of activated carbons produced from corn fiber and soy hulls. *Carbon Resour. Convers.* **3**, 19–28 (2020).

59. Chen, J. *et al.* Tunable Surface Area, Porosity, and Function in Conjugated Microporous Polymers. *Angew. Chemie - Int. Ed.* **58**, 11715–11719 (2019).

60. Jiang, J. X. *et al.* Conjugated microporous poly(aryleneethynylene) networks. *Angew. Chemie - Int. Ed.* (2007) doi:10.1002/anie.200701595.

61. Liao, Y., Weber, J. & Faul, C. F. J. Conjugated microporous polytriphenylamine networks. *Chem. Commun.* (2014) doi:10.1039/c4cc03026e.

62. Shida, N., Nishimi, H., Asanuma, Y., Tomita, I. & Inagi, S. Synthesis of a conjugated polymer with ring-fused pyridinium units via a postpolymerization intramolecular cyclization reaction. *Polym. J.* **52**, 1401–1406 (2020).

63. Dawson, R., Stöckel, E., Holst, J. R., Adams, D. J. & Cooper, A. I. Microporous organic polymers for carbon dioxide capture. *Energy Environ. Sci.* **4**, 4239–4245 (2011).

64. Dawson, R., Cooper, A. I. & Adams, D. J. Nanoporous organic polymer networks. *Prog. Polym. Sci.* **37**, 530–563 (2012).

65. Li, A. *et al.* Lithium-doped conjugated microporous polymers for reversible hydrogen storage. *Angew. Chemie - Int. Ed.* (2010)

doi:10.1002/anie.200906936.

66. National Grid ESO. Future Energy Scenarios Navigation. 1–124 (2020).

67. Aurora Energy Research. Hydrogen for a Net Zero GB: an integrated energy market perspective. (2020).

68. Gas, T. GB Gas Storage Data January 2021. 1–2 (2021).

69. *UK hydrogen strategy*. *Chemistry and Industry (London)* vol. 85 (2021).

70. Wang, H. *et al.* Conjugated Microporous Polycarbazole Networks as Precursors for Nitrogen-Enriched Microporous Carbons for CO2 Storage and Electrochemical Capacitors. *Chem. Mater.* **29**, 4885–4893 (2017).

71. Yang, L., Ma, Y., Xu, Y. & Chang, G. Cation-π induced lithium-doped conjugated microporous polymer with remarkable hydrogen storage performance. *Chem. Commun.* (2019) doi:10.1039/c9cc04174e.

72. Chen, L., Yang, Y., Guo, Z. & Jiang, D. Highly efficient activation of molecular oxygen with nanoporous metalloporphyrin frameworks in heterogeneous systems. *Adv. Mater.* **23**, 3149–3154 (2011).

73. Zhang, K., Kopetzki, D., Seeberger, P. H., Antonietti, M. & Vilela, F. Surface area control and photocatalytic activity of conjugated microporous poly(benzothiadiazole) networks. *Angew. Chemie - Int. Ed.* **52**, 1432–1436 (2013).

74. Jiang, J. X. *et al.* Metal-organic conjugated microporous polymers. *Angew. Chemie - Int. Ed.* (2011) doi:10.1002/anie.201005864.

75. Furukawa, H. *et al.* Ultrahigh porosity in metal-organic frameworks. *Science*

(80-.). (2010) doi:10.1126/science.1192160.

76. Zhou, Y. B. & Zhan, Z. P. Conjugated Microporous Polymers for Heterogeneous Catalysis. *Chemistry - An Asian Journal* (2018) doi:10.1002/asia.201701107.

77. Kou, Y., Xu, Y., Guo, Z. & Jiang, D. Supercapacitive energy storage and electric power supply using an aza-fused π-Conjugated microporous framework. *Angew. Chemie - Int. Ed.* **50**, 8753–8757 (2011).

78. Novotney, J. L. & Dichtel, W. R. Conjugated porous polymers for TNT vapor detection. *ACS Macro Lett.* **2**, 423–426 (2013).

79. Xiang, L. *et al.* A luminescent hypercrosslinked conjugated microporous polymer for efficient removal and detection of mercury ions. *Macromol. Rapid Commun.* (2015) doi:10.1002/marc.201500159.

80. Schon, T. B., McAllister, B. T., Li, P. F. & Seferos, D. S. The rise of organic electrode materials for energy storage. *Chem. Soc. Rev.* **45**, 6345–6404 (2016).

81. Borza, P. N. *Application of the Energy Storage Systems*. *Emerging Nanotechnologies in Rechargeable Energy Storage Systems* (Elsevier Inc., 2017). doi:10.1016/B978-0-323-42977-1.00009-1.

82. San Martín, J. I., Zamora, I., Martín, J. J. S., Aperribay, V. & Eguía, P. European Association for the Development of Renewable Energies, Environment and Power Quality (EA4EPQ) Energy Storage Technologies for Electric Applications. (2011).

83. Soloveichik, G. L. Battery Technologies for Large-Scale Stationary Energy Storage. *Annu. Rev. Chem. Biomol. Eng.* **2**, 503–527 (2011).

84. Liu, J. *et al.* Advanced Energy Storage Devices: Basic Principles, Analytical Methods, and Rational Materials Design. *Adv. Sci.* **5**, (2018).

85. Dunn, B., Kamath, H. & Tarascon, J. M. Electrical energy storage for the grid: A battery of choices. *Science (80-.).* **334**, 928–935 (2011).

86. Merlet, C. *et al.* On the molecular origin of supercapacitance in nanoporous carbon electrodes. *Nat. Mater.* **11**, 306–310 (2012).

87. Christen, T. & Carlen, M. W. Theory of ragone plots. *J. Power Sources* **91**, 210–216 (2000).

88. Cao, W., Zhang, J. & Li, H. Batteries with high theoretical energy densities. *Energy Storage Mater.* (2020) doi:10.1016/j.ensm.2019.12.024.

89. Durmus, Y. E. *et al.* Side by Side Battery Technologies with Lithium-Ion Based Batteries. *Adv. Energy Mater.* (2020) doi:10.1002/aenm.202000089.

90. Ragone, D. V. Review of battery systems for electrically powered vehicles. in *SAE Technical Papers* (SAE International, 1968). doi:10.4271/680453.

91. Lee, S. C. & Jung, W. Y. Analogical understanding of the Ragone plot and a new categorization of energy devices. *Energy Procedia* **88**, 526–530 (2016).

92. Gogotsi, Y. & Simon, P. True performance metrics in electrochemical energy storage. *Science* vol. 334 917–918 (2011).

93. Rahimi-Eichi, H., Ojha, U., Baronti, F. & Chow, M. Y. Battery management system: An overview of its application in the smart grid and electric vehicles.

IEEE Ind. Electron. Mag. **7**, 4–16 (2013).

94. Yu, H., Duan, J., Du, W., Xue, S. & Sun, J. China's energy storage industry: Develop status, existing problems and countermeasures. *Renew. Sustain. Energy Rev.* **71**, 767–784 (2017).

95. Liu, C., Li, F., Lai-Peng, M. & Cheng, H. M. Advanced materials for energy storage. *Adv. Mater.* **22**, (2010).

96. Myung, S. T. *et al.* Role of alumina coating on Li-Ni-Co-Mn-O particles as positive electrode material for lithium-ion batteries. *Chem. Mater.* **17**, 3695–3704 (2005).

97. Gover, R. K. B., Tolchard, J. R., Tukamoto, H., Murai, T. & Irvine, J. T. S. Investigation of Ramsdellite Titanates as Possible New Negative Electrode Materials for Li Batteries. *J. Electrochem. Soc.* **146**, 4348–4353 (1999).

98. Tian, B. *et al.* Insight into lithium diffusion in conversion-type iron oxide negative electrode. *J. Phys. Chem. C* **119**, 919–925 (2015).

99. Guerfi, A. *et al.* Improved electrolytes for Li-ion batteries: Mixtures of ionic liquid and organic electrolyte with enhanced safety and electrochemical performance. *J. Power Sources* **195**, 845–852 (2010).

100. Zahn, R., Lagadec, M. F., Hess, M. & Wood, V. Improving Ionic Conductivity and Lithium-Ion Transference Number in Lithium-Ion Battery Separators. *ACS Appl. Mater. Interfaces* **8**, 32637–32642 (2016).

101. Deng, D. Li-ion batteries: Basics, progress, and challenges. *Energy Science and Engineering* (2015) doi:10.1002/ese3.95.

102. Etacheri, V., Marom, R., Elazari, R., Salitra, G. & Aurbach, D. Challenges in the development of advanced Li-ion batteries: A review. *Energy and Environmental Science* (2011) doi:10.1039/c1ee01598b.

103. Stampatori, D., Raimondi, P. P. & Noussan, M. Li-ion batteries: A review of a key technology for transport decarbonization. *Energies* (2020) doi:10.3390/en13102638.

104. Goodenough, J. B. & Park, K. S. The Li-ion rechargeable battery: A perspective. *J. Am. Chem. Soc.* **135**, 1167–1176 (2013).

105. Heidari, E. K., Kamyabi-gol, A., Sohi, M. H. & Ataie, A. Electrode Materials for Lithium Ion Batteries : A Review. **51**, 1–12 (2018).

106. Francis, C. F. J., Kyratzis, I. L. & Best, A. S. Lithium-Ion Battery Separators for Ionic-Liquid Electrolytes: A Review. *Advanced Materials* (2020) doi:10.1002/adma.201904205.

107. Stoller, M. D., Park, S., Yanwu, Z., An, J. & Ruoff, R. S. Graphene-Based ultracapacitors. *Nano Lett.* **8**, 3498–3502 (2008).

108. Jiang, Y. & Liu, J. Definitions of Pseudocapacitive Materials: A Brief Review. *Energy Environ. Mater.* **2**, 30–37 (2019).

109. Ervin, M. H., Mailly, B. & Palacios, T. Electrochemical Double Layer Capacitance of Metallic and Semiconducting SWCNTs and Single Layer Graphene. *ECS Trans.* **41**, 153–160 (2019).

110. Mensah-Darkwa, K., Zequine, C., Kahol, P. K. & Gupta, R. K. Supercapacitor energy storage device using biowastes: A sustainable approach to green

energy. *Sustainability (Switzerland)* (2019) doi:10.3390/su11020414.

111. Bhoyate, S. *et al.* Eco-Friendly and High Performance Supercapacitors for Elevated Temperature Applications Using Recycled Tea Leaves. *Glob. Challenges* (2017) doi:10.1002/gch2.201700063.

112. Gao, Y. Graphene and polymer composites for supercapacitor applications: A review. *Nanoscale Research Letters* (2017) doi:10.1186/s11671-017-2150-5.

113. Jayalakshmi, M. & Balasubramanian, K. Simple capacitors to supercapacitors - An overview. *Int. J. Electrochem. Sci.* **3**, 1196–1217 (2008).

114. Choi, H. & Yoon, H. Nanostructured electrode materials for electrochemical capacitor applications. *Nanomaterials* **5**, 906–936 (2015).

115. Ellenbogen, J. C. Supercapacitors : A Brief Overview. (2006).

116. Mohapatra, S., Acharya, A. & Roy, G. S. The role of nanomaterial for the design of supercapacitors. *Lat. Am. J. Phys. Educ.* **6**, 380–384 (2012).

117. Chen, T. & Dai, L. Carbon nanomaterials for high-performance supercapacitors. *Mater. Today* **16**, 272–280 (2013).

118. Beidaghi, M. & Wang, C. Micro-supercapacitors based on interdigital electrodes of reduced graphene oxide and carbon nanotube composites with ultrahigh power handling performance. *Adv. Funct. Mater.* **22**, 4501–4510 (2012).

119. Drummond, R., Huang, C., Grant, P. S. & Duncan, S. R. Overcoming diffusion limitations in supercapacitors using layered electrodes. *J. Power Sources* **433**, 126579 (2019).

120. Chen, J., Qiu, T., Yan, W. & Faul, C. F. J. Exploiting Hansen solubility parameters to tune porosity and function in conjugated microporous polymers. *J. Mater. Chem. A* (2020) doi:10.1039/d0ta05563h.

121. Jenkins, S. *Hansen solubility parameters (HSP)*. *Chemical Engineering* vol. 118 (2011).

122. Cohen, P. P. Phiihp p. **113**, (1950).

123. Amin, K., Ashraf, N., Mao, L., Faul, C. F. J. & Wei, Z. Conjugated microporous polymers for energy storage: Recent progress and challenges. *Nano Energy* (2021) doi:10.1016/j.nanoen.2021.105958.

124. Molina, A. *et al.* New Anthraquinone-Based Conjugated Microporous Polymer Cathode with Ultrahigh Specific Surface Area for High-Performance Lithium-Ion Batteries. *Adv. Funct. Mater.* **30**, (2020).

125. Yeh, S. Y. & Wang, C. M. Anthraquinone-modified electrodes, preparations and characterizations. *J. Electroanal. Chem.* (2006) doi:10.1016/j.jelechem.2006.04.027.

126. Naoi, K., Suematsu, S. & Manago, A. Electrochemistry of Poly(1,5-diaminoanthraquinone) and Its Application in Electrochemical Capacitor Materials. *J. Electrochem. Soc.* (2000) doi:10.1149/1.1393212.

127. Li, X. G., Li, H., Huang, M. R. & Moloney, M. G. Synthesis and multifunctionality of self-stabilized poly(aminoanthraquinone) nanofibrils. *J. Phys. Chem. C* **115**, 9486–9497 (2011).

128. Cell, S. & Layers, A. Using Solubility Parameters to Model More Solar Cell

Active Layers. (2019).

129. Amin, K. *et al.* Surface controlled pseudo-capacitive reactions enabling ultra-fast charging and long-life organic lithium ion batteries. *Sustain. Energy Fuels* (2020) doi:10.1039/d0se00610f.

130. Pan, L. *et al.* Luminescent and Swellable Conjugated Microporous Polymers for Detecting Nitroaromatic Explosives and Removing Harmful Organic Vapors. *ACS Appl. Mater. Interfaces* (2019) doi:10.1021/acsami.9b16767.

131. Fang, X. PhD project, University of Bristol, 2021 – 2024..pdf.

132. Thomas, J. M. H. *et al.* Artificial synthesis of conjugated microporous polymers via Sonogashira-Hagihara coupling. *J. Phys. Chem. B* (2020) doi:10.1021/acs.jpcb.0c04850.

133. Liao, Y., Wang, H., Zhu, M. & Thomas, A. Efficient Supercapacitor Energy Storage Using Conjugated Microporous Polymer Networks Synthesized from Buchwald–Hartwig Coupling. *Adv. Mater.* **30**, (2018).